GALVANIC COUPLING OF AA5XXX-H116 AND CDA 706 UTILIZING LABORATORY, OUTDOOR, AND ACCELERATED TESTING

A Thesis Presented to

The Faculty of the School of Engineering and Applied Science

University of Virginia

In Partial Fulfillment

of the requirements for the Degree

Masters of Science (Materials Science and Engineering)

by

Lindsey Blohm

March 2018

APPROVAL SHEET

The thesis is submitted in partial fulfillment of the
requirements of the degree of
Master of Science (Materials Science and Engineering)

Lindsey McCoy Blohm
(Author)

This thesis has been read and approved by the examining Committee:

Dr. Robert G. Kelly
(Thesis Advisor)

Dr. James T. Burns
(Committee Chair)

Dr. James F. Fitzgerald
(Committee Member)

Accepted for the School of Engineering and Applied Science:

Dr. Craig H. Benson
Dean, School of Engineering and Applied Science
May 2018

Abstract

Aluminum-magnesium AA5XXX alloys are widely used in marine applications due to beneficial properties such as expense, strength, and weldability. However, when these alloys have greater than 3 wt% Mg, they are susceptible to sensitization at standard temperatures over time. With sensitization, more anodic β-phase (Al_3Mg_2) precipitates at the grain boundaries, resulting in a direct pathway for intergranular corrosion (IGC) propagation. With mechanical stress, intergranular stress corrosion cracking (IGSCC) can also occur. In addition to AA5XXX alloys, many marine vessels utilize CDA 706, a 90/10 cupronickel alloy, piping for water and heat transfer. CDA 706 directly couple to the AA5XXX superstructure. In addition, as copper corrosion products form, they can be carried through these pipes and deposit on exterior of the vessel's superstructure. These deposited copper corrosion products can be reduced to elemental copper, forming a galvanic couple that accelerates IGC propagation of the sensitized AA5XXX alloys.

Previous work has shown that both the cathode:anode ratio and increasing DoS accelerates IGC, as well as the anode size influences IGC. To understand the effects for these alloy system, AA5456-H116 was coupled to CDA 706 under full immersion conditions at varying cathode:anode ratios, with alterations in degree of sensitization (DoS) and anode area. Outdoor exposure testing was also utilized with AA5XXX alloys (AA5456-H116 and AA5083-H116) sensitized to varying levels and coupled to CDA 706 of different sizes to investigate IGC propagation of samples exposed to service marine environments. Exposure samples were mounted on the *R/V Endeavor* and *R/V Kilo Moana*, two University-National Oceanographic Laboratory System (UNOLS) vessels ported out of Rhode Island and Hawaii respectively. These exposure samples were exposed to diurnal weather conditions and salt spray as the vessels were at sea. In addition, galvanically coupled samples were also exposed in accelerated testing with ASTM G85-A2 wet bottom (WB) and G85 WB modified version of G85-A2. Cross-sectional analysis was used to quantitatively assess the spatial and temporal distribution of the damage. Modelling was also used to correlate damage to water layer thickness. These results are correlated to outdoor exposure retrievals to compare IGC damage and connect service exposures to laboratory testing.

Based on initial results, DoS is shown to increase IGC propagation in both full immersion and outdoor exposure samples. As more β-phase is present at grain boundaries, IGC accelerates propagation. Mixed potential theory was used to explain the role of cathodic kinetics as cathode:anode ratio increases IGC following full immersion testing. Outdoor exposure returns show the effect of not only DoS, but cathode:anode ratio, geolocation, and relative humidity (RH) conditions under which samples were exposed. Following accelerated testing in G85-A2, damage follows throwing power trends modeled by Finite Element Modeling with COMSOL. A water layer thickness of 3000 um was found to be most comparable to damage seen experimentally.

Acknowledgments

I would like to first sincerely thank my advisor, Professor Rob Kelly, for his invaluable guidance and support. I will forever be grateful to have had him as a confidant through trying times of my graduate career and having him as a support system. I cannot thank him enough for being an incredible mentor and provided me with some amazing and unforgettable opportunities for which I will be forever grateful and will carry with me throughout my career.

I would also like to acknowledge my fellow CESE members for their aid in laboratory, be it aiding me with procedures or troubleshooting. A particular thank you to my RGK group members who have tolerated all my pestering questions and always been there for me when I needed a hand in the lab, or help answering a research problem. They have been an amazing asset to learn from, as well as great fun to share offices and explore Charlottesville and other cities! Thank you to my amazing undergraduate help (John, Harris, Cameron, Jay) who helped me with data collection and experimentation. Special thanks to all the great friends I have made in Charlottesville with whom it has been so much fun exploring restaurants, breweries, and attending sporting events! Go Hoos!

Thanks to all my former colleagues at the Army Research Laboratory, particularly Dr. Joe Labukas from whose mentorship and support I found inspiration to pursue a career in this field and come to The University of Virginia.

Finally, all my love and thanks to my amazing family. You are always there for me and have always inspired me to reach for my dreams. I couldn't ask for a better support system. Love you Ma, Dad, Leigh and Kev!

Table of Contents

List of Figures

List of Tables

1 Introduction

1.1 Galvanic Corrosion

Galvanic coupling occurs when two metals are electrically or physically in contact with an electrolytic solution. The galvanic series in a seawater electrolyte, shown in Figure 1.1[1], displays a range of active (more negative) to noble (more positive) metals. The more negative (active) metal will act as the anode in a coupling situation, leaving the more positive (noble) metal to be the cathode. By creating a galvanic couple, the anode will corrode more rapidly than if it is left uncoupled. This coupling can even occur within an alloy. For example, copper or intermetallic precipitates within aluminum alloys have been found to accelerate bulk alloy uniform corrosion[10].

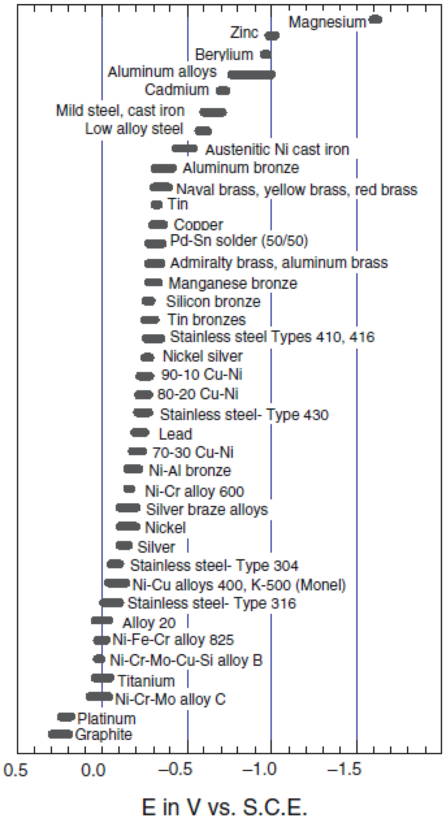

Figure 1.1[1]: Galvanic series of various metals and alloys in seawater

From mixed potential theory, it is known that the cathodic and anodic rate must be equal. Therefore, by increasing cathodic size, resulting in an increase in cathodic kinetics, anodic corrosion accelerates. Figure 1.2[2] shows overlayed polarization curves for two materials, with material 1 being more noble. When coupled at the same area ratio, the potentials and current of each material will equal, as denoted by E_{couple} and I_{couple}. When coupled, the applied E_{couple} potential increases above the open circuit potential (OCP) of material 2, accelerating dissolution as the pitting potential is approached. From coupling, the corrosion rate of Metal 2 accelerates dissolution due to moving to a higher potential. The I_{CORR} values also increase following coupling, increasing dissolution.

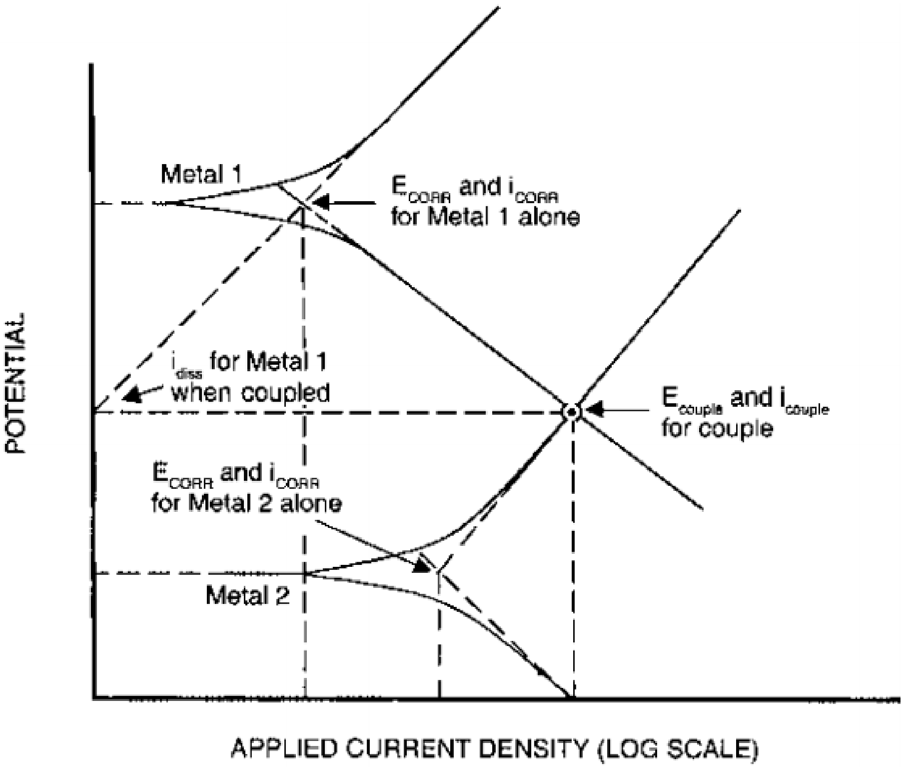

Figure 1.2[2]: Polarization curves of two metals being analyzed for galvanic coupling behavior

Cathode size also effects corrosion rates when coupling samples. As shown in Figure 1.3, when coupling iron (cathode) and zinc (anode), with increasing cathode size, the I_{CORR} increases and E_{CORR} becomes more positive. With the increase in cathode size, and cathodic current density, the anodic current density will increase equally. This increase in current, rapidly accelerates intergranular corrosion (IGC) propagation of the small anode area.

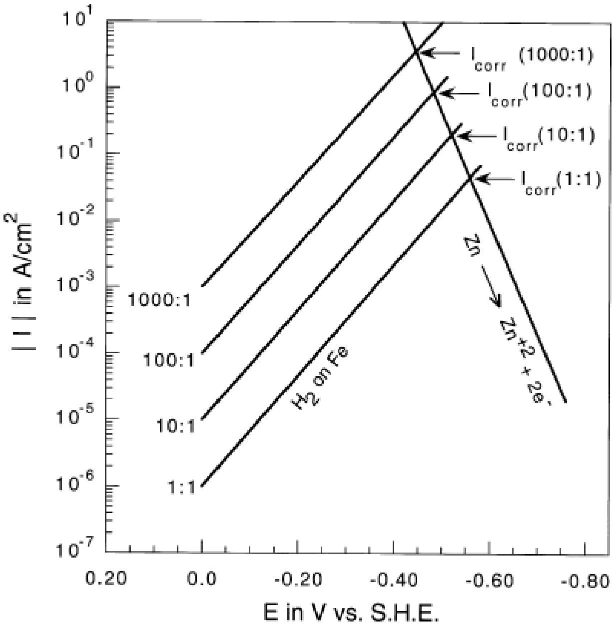

Figure 1.3[1]*: Polarization curves of two metals being analyzed for galvanic coupling behavior of iron and zinc*

1.2 Atmospheric Corrosion vs Bulk/Full Immersion

Although many systems are exposed to atmospheric conditions, much of past work has been performed in full immersion, or bulk testing solutions. Recent work has compared these two different testing systems. Khullar et al. investigated IGC propagation under thin film with oxidizers to accelerate the corrosion rate[11]. It is shown that cathodic kinetics control IGC rate, while in full immersion and thin films, the same potential controls IGC propagation[11]. Mizuno et al. studied IGC propagation for AA5083-H131 and AISI 4340 steel under full immersion and thin film conditions[3]. Through scanning kelvin probe (SKP) measurements, it was found that high potentials at the coupling boundary accelerate IGC, as shown in Figure 1.4, and throwing power is comparable with that in full immersion testing[3]. This work shows that for coupling, full immersion and thin film are comparable.

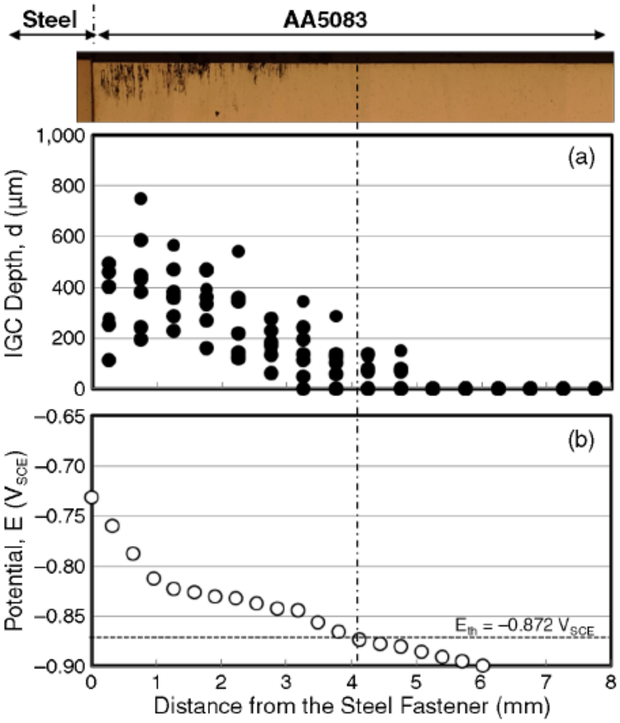

Figure 1.4[3]: IGC depth measured following exposure testing, compared to SKP potential measurements for AA5083-H131 (DoS 50 mg/cm^2) coupled with AISI 4340 steel

1.3 Service Connection

Naval ship structures, containing a galvanic couple, advance a potential corrosion threat. AA5XXX aluminum alloys have many beneficial properties including strength, corrosion resistance, weldability. Due to these properties, aluminum alloys are increasingly used by the United States Department of Defense for vehicles and ships[12]. These AA5XXX alloys sensitize, resulting in a more active β phase (Al_3Mg_2) precipitation at the grain boundaries. The rate of degree of sensitization (DoS) fluctuates with time, temperature, alloy, as well as mechanical treatment[13,14]. Sensitization can occur at temperatures as low as 50°C, which is actively seen in field exposures[14]. This sensitization accelerates IGC, which can lead to intergranular stress corrosion cracking (IGSCC).

Galvanic coupling can accelerate this IGC, when a more noble material is added to the system. These couples are formed when high strength fasteners or deposition of corrosion products on AA5XXX superstructures. The littoral combat ship (LCS) has had complications following coupling of unsensitized AA5083-H116 to stainless steel water jets resulting in corrosion problems[15]. Within one year of manufacturing, the USS Independence, the first LCS produced, suffered galvanic corrosion[16]. In addition, there are other galvanic couples on these naval vessels. Much of the piping on naval ships is fashioned of copper alloys, including a cupronickel alloy CDA 706 (C70600), that directs seawater overboard[17]. There is a direct coupling of CDA 706 and AA5XXX at their junction point on the ships superstructure. In addition, copper corrosion products, carried through these CDA 706 pipes, can deposit on the AA5XXX superstructures as shown in Figure 1.5[4], potentially accelerating the IGC of the sensitized aluminum alloys.

Figure 1.5[4]: Littoral combat ship with copper corrosion deposition

1.4 5XXX Aluminum-Magnesium Alloys

AA5XXX alloys are strengthened via magnesium addition and cold working, as they are not heat treatable[18]. The grain structure of these strain hardened aluminum-magnesium alloys is displayed in Figure 1.6[5], a barkers etched AA5083-H131 alloy. The microstructure of AA5XXX have elongated grains on the longitudinal by short transverse (LS) and short transverse (ST) planes, and wide grains on the long transverse (LT) plane. IGC growth rate, studied in detail by Lim, was found to be comparable in both the L and T, but not in the S direction, due to elongated grain structures[5].

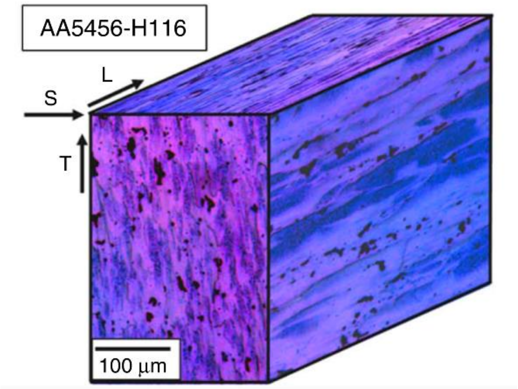

Figure 1.6[7]: Barkers etch of AA5456-H116 showing grain structure along the SL, ST, and LT faces

AA5XXX aluminum-magnesium alloys, although they have many beneficial properties, present challenges due to their susceptibility to IGC as a function of sensitization[5]. Sensitization occurs with the precipitation of the highly active β phase (Al_3Mg_2) at the grain boundaries, resulting in an active path for corrosion. This grain boundary precipitation has been studied in depth, and is imaged on sensitized AA5083 using SEM in Figure 1.7[6]. The more anodic β phase corrodes preferentially due to the electrochemical difference between the precipitates and more noble α bulk phase.

Sensitization also results in an increase in stress corrosion cracking susceptibility. Severe IGSCC has been found to be severe above a critical DoS level of 9-12 mg/cm^2 for AA5083-H131[19]. Though still debated, many works favor hydrogen embrittlement (HE) mechanism to control IGSCC susceptibility due to β phase dissolution[20]. For constant tempers, it has been found that increased Mg content reduces IGSCC susceptibility[21] .

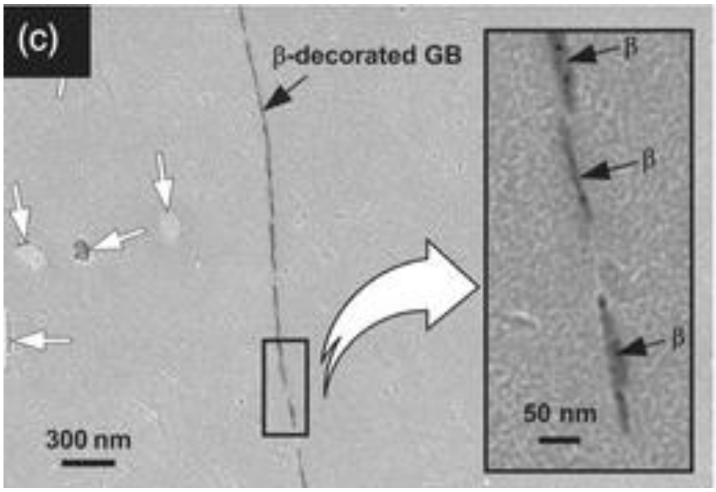

Figure 1.7[6]: SEM micrograph of sensitized, polished, and etched AA5083 showing β phase precipitation at the grain boundary

1.5 CDA 706 Cupronickel

Cupronickel alloys are widely used in naval applications[17,22–26]. CDA 706 (otherwise known as C70600) is a CuNi 90/10 cupronickel alloy has widely used for piping materials for water and heat exchange systems[17]. This cupronickel alloy is used due to beneficial properties, including corrosion resistance (localized, uniform, and erosion) as well as bacteriostatic and microfouling resistant properties[17]. Although these alloys are corrosion resistant, they develop a corrosion product film when exposed to seawater. North et al. found that the major corrosion products formed from CDA 706 are Cu_2O, [$Cu_2(OH)_3Cl$], CuO, and $CuCl_23Cu(OH)_2$ forming a protective product film ranging from 2800-4400Å[17,27]. With seawater passing through these pipes, a shear stress strips away the protective corrosion product film from these alloys[26]. These corrosion products, carried by seawater over these naval vessels, deposit on the AA5XXX superstructure as imaged in Figure 1.5.

1.6 Research Questions and Hypothesis

As summarized, AA5XXX and CDA 706 couple on the superstructure of naval vessels. Coupling has not yet resulted in major damage on the LCS, but over time, as AA5XXX sensitizes, it is expected to increase susceptibility and accelerate IGC. The studies performed in this work investigate direct coupling of AA5XXX and CDA 706 rather than CDA 706 corrosion products. CDA 706 corrosion products will reduce on the surface of the AA5XXX, converting copper ions into metallic copper. For this reason, CDA 706 is directly used rather than copper oxide corrosion products. From past work performed at the University of Virginia by Khullar, it has been found that anode size affects IGC propagation[11]. Mizuno et al. found that cathode:anode ratio, with sensitized AA5083, effects IGC propagation as well[3,28].

This past work leads to an investigation of cathode:anode ratio, while changing the size of the cathode and the anode. It is hypothesized that the anode area influences IGC and increased cathodic kinetics from increasing the cathode size also influence IGC propagation. It is also hypothesized that increasing the DoS, will increase IGC due to increased active area due to added β phase at the grain boundaries.

1.7 Objective Statement

The main goal of this thesis is to understand the effect of galvanic coupling on IGC propagation using AA5XXX and CDA 706. The role of coupling will be studied using varying anode sizes, cathode:anode ratios, DoS, and AA5083-H116 and AA5456-H116 aluminum-magnesium alloys.

1.8 Thesis Organization

Figure 1.8 depicts a schematic for the layout of this thesis. The galvanic coupling of sensitized AA5XXX and CDA 706 using full immersion coupling, outdoor exposure, and accelerated testing with a modeling investigation of damage.

Chapter 2 presents a galvanic coupling investigation of sensitized AA5456-H116 with CDA 706 using a zero-resistance ammeter (ZRA) test. The effect of cathode:anode ratio, anode size, and DoS were investigated. All of these previously stated factors were found to have an effect on IGC propagation.

Chapter 3 presents an outdoor exposure investigation of galvanically coupled AA5XXX and CDA 706. Exposures were placed on research vessels (*R/V*) *Endeavor* and *Kilo Moana* ported in Rhode Island and Hawaii respectively. The corrosivity of each environment, and resultant corrosion damage on exposure samples were correlated. Following the effect found of CDA size and DoS in Chapter 2, these effects were investigated and found to have effect IGC propagation.

Chapter 4 explores the IGC propagation of galvanically coupled AA5456-H116 DoS 54mg/cm^2 and CDA 706 in G85 wet bottom (WB) and G85 WB Modified tests. Samples tested were identical to those used in outdoor exposure testing. Modeling, performed by

Chao (Gilbert) Liu, was also performed to investigate throwing power of CDA 706 in a G85 accelerated testing environment.

Chapter 5 summarizes the conclusions and ties in results from each chapter, and their correlation with each other. The technological impacts of this work as well as recommendations for future work are discussed.

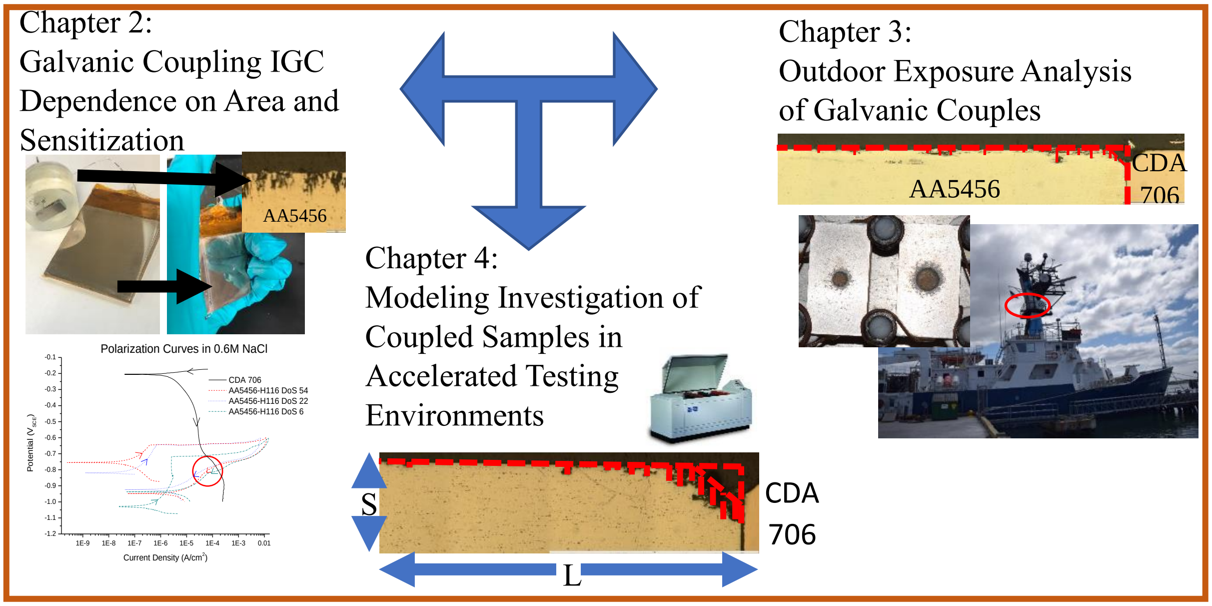

Figure 1.8: Schematic for Thesis Organization

1.9 References

1. McCafferty, E. *Introduction to Corrosion Science*. (2009).
2. Kelly, R., Scully, J., Shoesmith, D. & Buchheit, R. *Electrochemical Techniques in Corrosion Science and Engineering*. **20021014,** (2002).
3. Mizuno, D. & Kelly, R. G. Galvanically Induced Intergranular Corrosion of AA5083-H131 Under Atmospheric Exposure Conditions - Part I –Experimental Characterization. 1–6 (2013).
4. Golumbfskie, W. private communication.
5. Lim, M. L. C., Kelly, R. G. & Scully, J. R. Overview of intergranular corrosion mechanisms, phenomenological observations, and modeling of AA5083. *Corrosion* **72,** 198–220 (2016).
6. Birbilis, N. *et al.* A Survey of Sensitisation in 5xxx series Aluminium Alloys. *Corrosion* **72,** 144–159 (2016).

7. McMahon, M., Steiner, P., Lass, A. & Burns, J. The Effect of Loading Orientation on the Stress Corrosion Cracking of Al-Mg Alloys. *Corrosion* **73,** 347–361 (2017).
8. https://www.vesseltracker.com/en/Ships/Kilo-Moana-9229037.html.
9. Mary Parker (personal communication). (2018).
10. Greene, H. J. Evaluation of Corrosion Protectin Methods for Aluminum Metal Matrix Composites. (1992).
11. Khullar, P., Badilla, J. V & Kelly, R. G. Intergranular Corroson in Al-Mg 5XXX Alloys Under Atmospheric Exposures. in *NACE* 1–10
12. Montgomery, J. S. & Chin, E. . The AMPTIAC Quarterly. **8,** 15–20 (2004).
13. Searles, J. L., Gouma, P. I. & Buchheit, R. G. Stress corrosion cracking of sensitized AA5083 (Al-4.5Mg-1.0Mn). *Metall. Mater. Trans. A Phys. Metall. Mater. Sci.* **32,** 2859–2867 (2001).
14. Oguocha, I. N. A., Adigun, O. J. & Yannacopoulos, S. Effect of sensitization heat treatment on properties of Al-Mg alloy AA5083-H116. *J. Mater. Sci.* **43,** 4208–4214 (2008).
15. Lerman, D. & Capaccio, T. Navy Finds 'Aggressive' Corrosion on Austal's Combat Ship. *Bloomberg* (2011). Available at: https://www.bloomberg.com/news/articles/2011-06-17/navy-finds-aggressive-corrosion-on-austal-s-combat-ship-1-.
16. CORROSION FAILURE: LCS 2 USS Independence Naval Ship Engine Corrosion. *NACE International* Available at: https://www.nace.org/CORROSION-FAILURE-LCS-2-USS-Independence-Naval-Ship-Engine-Corrosion.aspx.
17. Schleich, W. *Typical failures of CuNi 90/10 seawater tubing systems and how to avoid them*.
18. Davis, J. R. Corrosion of Aluminum and Aluminum Alloys. *Mater. Park. OH ASM Int.* 75–83 (1999).
19. Crane, C. B. & Gangloff, R. P. Stress Corrosion Cracking of Low Temperature Sensitized AA5083. *Corrosion* **72,** 1–14 (2011).
20. Jones, R. H., Baer, D. R., Danielson, M. J. & Vetrano, J. S. Role of Mg in the Stress Corrosion Cracking of an Al-Mg Alloy. *Metall. Mater. Trans. A* **32,** 1699–1711 (2001).
21. McMahon, M. E., Steiner, P. J., Lass, A. B. & Burns, J. T. The Effect of Temper and Composition on the Stress Corrosion Cracking of Al-Mg Alloys. *Corrosion* **73,** 347–361 (2017).
22. Aylor, D. M., Hays, R. A. & Marshall, L. S. *Galvanic Corrosion Evaluation of High Performance Naval Seawater Valve Materials in Quiescent, Natural Seawater*. (2000).
23. Hack, H. P. & Wheatfall, W. W. Evaluation of Galvanic and Stray Current Corrosion in 70/30 Copper-Nickel/Alloy 625 Piping Systems. *CARDIVNSWC-TR-61--94/15* (1995).
24. Hack, H. P. & Wheatfall, W. W. *Comparison of Cathodic Protection Currents on 70/30 Copper-Nickel and Alloy 625 Piping Systems*. *CARDIVNSWC-TR-61--94/14* (1995).
25. Srinivasa Rao, A. *Characterization of the Surface Film Growth During the Electrochemical Process: Part III (70 % Copper- 30 % Nickel System). CARDIVNSWC - TR - 61 - 98 - 24* (1998).
26. Tuthill, A. H. Guidelines For the Use of Copper Alloys In Seawater. *Mater. Perform.* **26,** 12–22 (1987).
27. North, R. F. & Pryor, M. J. The Influence of Corrosion Product Structure on the Corrosion Rate of Cu-Ni Alloys. *Corros. Sci.* **10,** 297–311 (1970).
28. Mizuno, D. & Kelly, R. G. Galvanically Induced Intergranular Corrosion of AA5083-

H131 Under Atmospheric Conditions Part 2 Modelling the damage. *Corrosion* **69,** 681–692 (2013).

29. Khullar, P. & Kelly, R. G. *Investigation of Corrosion Testing Methods and Selected Corrosion Protection Strategies on Modern High-Performance Alloys that Affect Land Vehicle Structural Integrity (2012-2016)*. (2016).
30. Mizuno, D. & Kelly, R. G. Galvanically Induced Intergranular Corrosion of AA5083-H131 Under Atmospheric Conditions Part 2 Modelling the damage. *Corrosion* **69,** 681–692 (2013).
31. Holtz, R. L., Pao, P. S., Bayles, R. A., Longazel, T. M. & Goswami, R. Corrosion-fatigue behavior of aluminum alloy 5083-H131 sensitized at 448 K (175 C). *Metall. Mater. Trans. A Phys. Metall. Mater. Sci.* **43,** 2839–2849 (2012).
32. Lim, M. L. C. *et al.* Model to predict intergranular corrosion propagation in three dimensions in AA5083-H131. *Mater. Des.* **96,** 131–142 (2016).
33. Lim, M. L., Scully, J. R. & Kelly, R. G. Intergranular Corrosion Penetration in AA5083 as a Function of Electrochemical and Metallurgical Conditions service. **69,** 35–47 (2013).
34. Schleich, W. Typical failures of CuNi 90/10 seawater tubing systems and how to avoid them. *Eng. Struct.* **49,** (2004).
35. ASTM G67-04, 'Standard Test Method for Determining the Susceptibility to Intergranular Corrosion of 5XXX Series Aluminum Alloys by Mass Loss After Exposure to Nitric Acid (NAMLT Test)'. (2004).
36. M. Tiryakioglu, J. T. S. Physical Metallurgy and the Effect of Alloying Additions in Aluminum Alloys. in *Handbook of Aluminum* (ed. G.E. Totten, D. S. M.) (Marcel Dekker, Inc, 2003).
37. Tattersall, C. Manual for Depth Analysis Code.
38. Tattersall, C. & Kelly, R. G. Automated Quantification of Corrosion Damage from Cross-sectional Micrographs. *to be Submitt. to Corros.*
39. Burns, C. *Understanding the Intergranular Corrosion Kinetics in AA5456-H116 as a Function of Electrochemical and Metallurgical Variables*. (2017).
40. Abbott, W. H. A Decade of Corrosion Monitoring in the World ' s Military Operating Environments -A Summary of Results. *Columbus, OH DoD CorrDefense* (2008).
41. Katona, R. Personal Communication. (2017).
42. Macha, Erica N.;Dante, J. F. Effect of Cyclic RH & Preliminary Sensor Analysis. Personal Communication. (2018).
43. Neiser, E. B. Atmospheric Corrosion of Silver and its Relation to Accelerated Corrosion Testing. (University of Virginia, 2010).
44. ASTM B825-13: Standard Test Method for Coulometric Reduction of Surface Films on Metallic Test. *Annu. B. ASTM Stand.* (2002). doi:10.1520/B0825-13.2
45. NIH. Image J.
46. Horton, D. J., Sanders, C. E., Anderson, R. M., Davis, R. S. & Lemieux, E. J. Accelerated Field Exposure using Seawater Spray: A Comparison to Traditional Atmospheric Test Methods. *NACE Corros. Conf.* **Paper No.,** 1–11 (2017).
47. Lim, M. L. C. Intergranular Corrosion Propagation in Sensitized Al-Mg Alloys. (University of Virginia, 2016).

2 Galvanic Coupling Study of Sensitized AA5456-H116 with CDA 706 and the Effects of Cathode to Anode Coupling Area Ratios

2.1 Abstract

The galvanic corrosion behavior of sensitized AA5456-H116 coupled to CDA706 under full immersion conditions was experimentally investigated. The effects of anode area, degree of sensitization (DoS), and cathode:anode ratio on intergranular corrosion (IGC) propagation rate, as well as potential and coupling current densities, were quantified. It was found that increasing anode area, DoS, and cathode:anode area ratio increases IGC rate. Area of anode is proven to be of importance for IGC due to insufficient cathodic kinetics for anodic dissolution at small areas. Increased cathode:anode ration increases these cathodic kinetics for IGC based on mixed potential theory.

2.2 Overview

The following chapter presents an experimental study of area of cathode and anode, as well as sensitization on intergranular corrosion (IGC) propagation in AA5456-H116. Khullar et al[29]. has found that the size of anode, in this case AA5456-H116 has an effect on IGC. Mizuno et al[28,30]. has also found that with increased cathode:anode ratio, IGC increases. For this work, increased cathode size, resulting in increased cathodic kinetics was hypothesized to increase IGC. It was also hypothesized, that with increased anode area, IGC further propagates. These hypotheses were tested using zero resistance ammeter (ZRA) tests under full immersion with AA5456-H116 at 1 cm^2 and 3 cm^2 areas and varying degrees of sensitization galvanically coupled to varying areas of CDA 706. The results show that both anode and cathode size, as well as degree of sensitization (DoS) have an effect on IGC. Potential and coupling potential correlate with these results. Mixed potential theory was used to explain how anodic and cathodic kinetics influence this IGC.

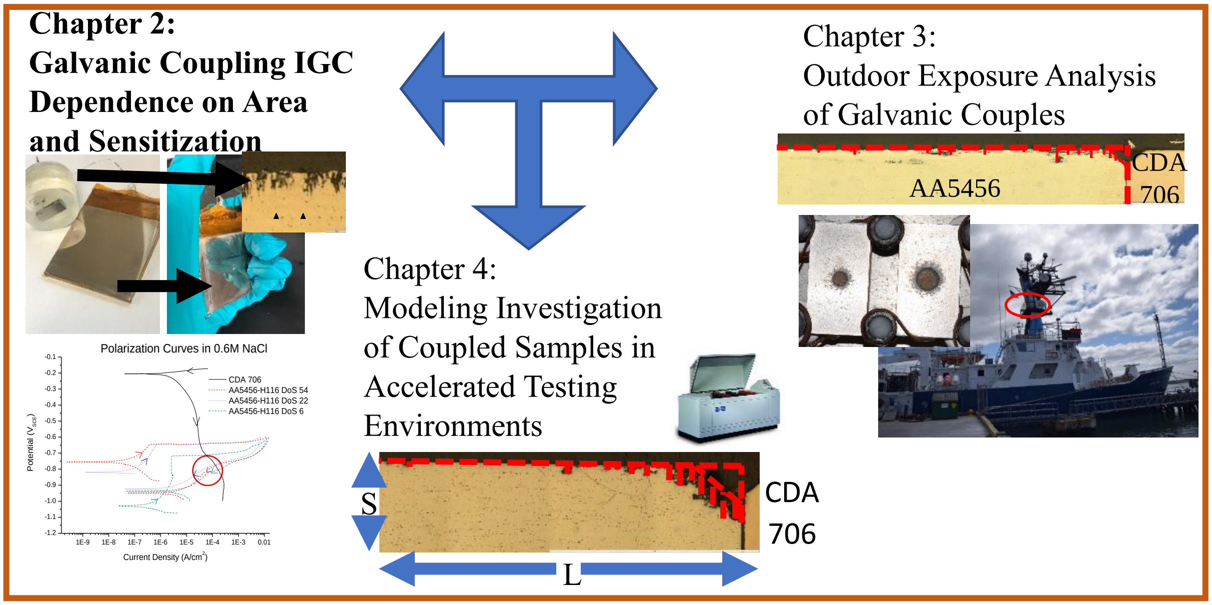

Schematic for Thesis Organization

2.3 Introduction

5XXX series aluminum-magnesium alloys are widely utilized in marine applications due to a combination of beneficial properties including strength, corrosion resistance, ductility, and weldability[14,31]. Microstructures of 5XXX series show elongated grains on the longitudinal by short transvere (LS) and short transverse (ST) planes, and wide grains on the long transverse (LT) plane. This grain morphology is evident in the Barker's etch micrograph of AA5456-H116 shown in Figure 2.1[7]. Intergranular corrosion (IGC) growth rate, studied in detail by Lim, was found to be comparable in both the L and T directions based on the elongated grain structures and the similarity in the low degree of grain boundary path tortuosity[32].

These AA5XXX alloys, when containing greater than 3wt% Mg, are susceptible to sensitization leading to susceptibility to IGC after extended times at standard service temperatures[14]. At temperatures as low as 50°C, for extended periods of time, sensitization is observed[14]. With added stress, intergranular stress corrosion cracking (IGSCC) can occur. When AA5XXX sensitizes, the β phase (Al_3Mg_2) precipitates out at the grain boundaries[32]. The β phase is more active than the bulk phase, creating a direct pathway for IGC. Previous studies have shown that for AA5083 in artificial seawater, the degree of sensitization (DoS), applied potential, and rolling direction of the alloy are the main influences on IGC rate[3,33].

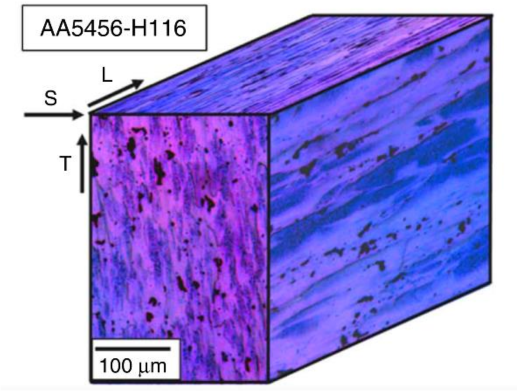

Figure 2.1[7]*: 5456-H116 alloy microstructure revealed with Barker's etch*

In addition to sensitization, these alloys are often galvanically coupled in their varying marine applications. Many naval vessels utilize CDA 706 pipes within their superstructure that couple to the AA5XXX superstructure. These CDA 706 pipes are being utilized in marine structures for water and heat exchange[22,34]. CDA 706 is widely used due to its resistance to uniform and localized corrosion, as well as its bacteriostatic and anti-microfouling properties[34]. Although the corrosion rate of CDA 706 in seawater is low, some dissolution does occur. These pipes can then carry CDA 706 corrosion products in the seawater and deposit them on the superstructure of the 5XXX alloy ship, generating a direct galvanic couple. This direct galvanic coupling of copper and aluminum alloys could accelerate corrosion propagation, particularly if the 5XXX alloy is sensitized.

Past work has studied the extent of IGC damage on AA5083-H131 due to the coupling with AISI 4340 steel under both full immersion and atmospheric conditions[3,30]. Mizuno has shown, that at the same potential, IGC is comparable under full immersion and atmospheric conditions[30]. This finding allows future experimentation to be performed utilizing full immersion parameters. It was also noted that DoS and coupling area ratios of anode:cathode affect IGC growth[30].

Mizuno et al. found that not only does the cathode:anode area ratio have an effect on IGC rate, but also the size of the anodes being utilized affects the damage observed[3]. Khullar found that under accelerated testing, with increased sample size, IGC became more prominent[29]. For this reason, it is of interest to investigate the prominence of IGC dependence on the surface area of the anode. This study focuses on galvanic coupling of AA5456-H116 and CDA 706, and the effect that area ratios of anode to cathode have on IGC.

2.4 Materials

Samples were machined to size from a AA5456-H116 ¼" thick plate were provided by the Naval Surface Warfare Center-Carderock Division (NSWCCD). AA5456-H116 samples were heat treated at 100°C to 6, 14, 23, and 54 mg/cm^2 degrees of sensitization for 0, 1, 3, and 14 days respectively. These sensitization durations have been validated using ASTM G67[35] nitric acid mass loss test (NAMLT). As shown in Table 2.1, the main alloying element of AA5456-H116 is magnesium. H116 is representative of the temper, designating that the alloy is special strain hardened, and corrosion resistant[36]. Metal Samples provided CDA 706, otherwise known as C70600, which is a cupronickel alloy as indicated in Table 2.2.

Table 1: Alloy composition of 5456-H116 ¼" provided by NSWCCD (by materials certification)

5456-H116								
Element	Al	Mg	Fe	Si	Cr	Zn	Ti	Cu
Wt %	Rem.	5.2640	0.1830	0.1570	0.0930	0.0560	0.0263	0.0240

Table 2: Alloy composition of CDA 706 provided by Metal Samples (by materials certification)

CDA 706					
Element	Cu	Ni	Fe	Mn	Impurities
Wt %	87.778	9.948	1.453	0.793	Rem.

2.5 Experimental Procedures

Polarization experiments were performed on samples machined from a ¼" thick plate of AA5456-H116 and CDA 706. AA5456-H116 DoS 6, 23, and 54 mg/cm^2 were individually mounted with the ST face exposed. AA54546-H116 and CDA 706 samples were prepared by polishing to 1200 grit with silicon carbide papers, followed by 3 and 1µm diamond suspension, before finishing with 0.05µm colloidal silica. Both CDA 706 and AA5456-H116 were tested in quiescent 0.6M NaCl. The open circuit potential (OCP) was measured for 2 hours. CDA 706 samples were polarized +0.05 V above OCP, to -1.0C (vs SCE) at 0.5 mV/s. AA5456-H116 samples were polarized from -0.05 V below OCP, to -0.06 V (vs SCE), and reversed to -1 V at 0.5 mV/s.

Galvanic coupling experiments were performed with a Biologic VMP-300 with AA5456-H116 and CDA 706 utilizing a range of cathode:anode area ratios. AA5456-H116 samples that were sensitized to DoS 14, 23, and 54 mg/cm^2 were for these coupling experiments. The A5456-H116 samples were cut to an area of 1 cm^2 and 3 cm^2. From Figure 2.1, it is seen that grain boundary interfaces are under 100 µm on the ST face, resulting in ample grain boundary exposures on both the 1 and 3 cm^2 AA5456-H116 samples. The CDA 706 samples were machined to areas of 1, 3, 50, and 300 cm^2. The samples, both AA5456-H116 with the SL face exposed, and CDA706 were polished to 1200 grit with silicon carbide papers prior to testing. The 1 cm^2 anode was coupled to cathodes of sizes: 0, 1, and 50 cm^2. The 3 cm^2 anode was coupled to cathodes of sizes: 0, 3, and 300 cm^2. AA5456-H116 was used as the working electrode, CDA706 was the counter electrode, and saturated calomel electrode (SCE) was used as the reference electrode. Samples were coupled galvanostatically for 100 hours using a zero-resistance ammeter (ZRA) test with an electrolyte of 0.6M NaCl at a pH of 8.3.

After 100 hrs, the exposed SL faces of AA5456-H116 samples were imaged using an optical microscope at 5x magnification. They were then cross-sectioned, mounted, and polished to 1200 grit with silicon carbide papers, followed by 3 µm, 1 µm diamond polish and 0.05 µm colloidal silica finish, allowing the ST surface to be imaged. Using an optical microscope at 5x magnification, micrographs were collected over three depths of polish for quantification and averaging. To calculate the maximum and mean IGC, a MATLAB code[37] provided by Tattersall et al.[38] was utilized to investigate IGC in the T direction. The average and standard deviation of both the maximum and mean IGC depth was calculated from the three depths of polish on each sample. In addition, of these AA5456-H116 galvanically coupled samples, at all three sequential depths of polish, had the total number of fissures counted and averaged using optical micrographs. The coupling potential and current density were recorded for galvanic samples, with the last 2000 s averaged for reporting. The current density was normalized using the area anode exposed.

2.6 Results

Polarization curves of CDA 706 and AA5456-H116 in 0.6M NaCl are shown in Figure 2.2. CDA 706 exhibits a higher open circuit potential than AA5456-H116. There is approximately a 340-800 mV difference in driving force between copper and aluminum alloys based on the galvanic series. The overlaid polarization curves suggest an anode to cathode with area ratio of 1:1 would have a galvanic couple potential ranging from -0.772 V to -0.813 V (vs SCE), dependent on DoS. It is also evident that CDA 706 is more noble, therefore the cathode in the coupling relationship to AA5456-H116 in galvanic coupling experiments. After sitting coupled at OCP for 100 hrs, the CDA 706 remained shiny and untarnished as evident in Figure 2.3.

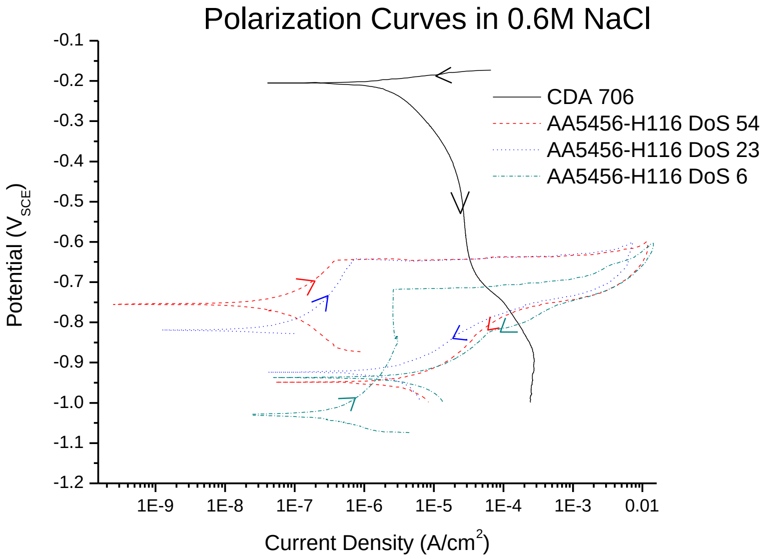

Figure 2.2: Polarization curves of CDA 706 and sensitized AA5456-H116 in 0.6M NaCl

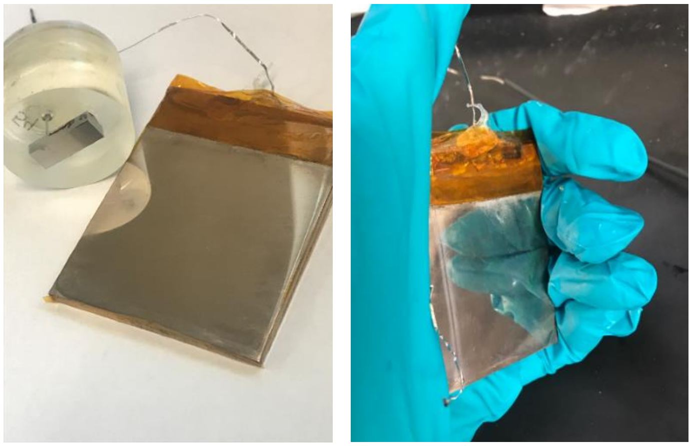

Figure 2.3: CDA 706 sample before and after 100hr galvanic coupling

Figure 2.4a shows surface micrographs of the exposed AA5456-H116 ST surfaces after 100hr full immersion galvanically coupled to CDA 706 samples over a range of area ratios. Based on visual surface damage, it is evident that as the DoS, as well as the cathode:anode ratio increases, surface damage also increases. After cross-sectioning samples to investigate IGC propagation in the L direction, as shown in Figure 2.4b, this trend is validated. IGC propagates further in the L direction with an increase in sensitization, and cathode to anode ratio.

The maximum IGC measurements for the 1 cm^2 and 3 cm^2 AA5456-H116 cross-sections are shown in Figure 2.5. Maximum IGC generally increases as a function of DoS, although the DoS 14 mg/cm^2 sample at the 1 cm^2 anode to 1 cm^2 cathode ratio showed greater than expected attack. A magnified cross section of the 1 cm^2:1 cm^2 DoS 14mg/cm^2 sample is superimposed on Figure 2.5. As the coupling ratio of cathode to anode increases, so does the maximum IGC. When the size of the anode, AA5456-H116, is changed from 1 cm^2 to 3 cm^2, the maximum IGC measurements increase. This area influence is most prominently seen at lower sensitizations, particularly DoS 14 mg/cm^2.

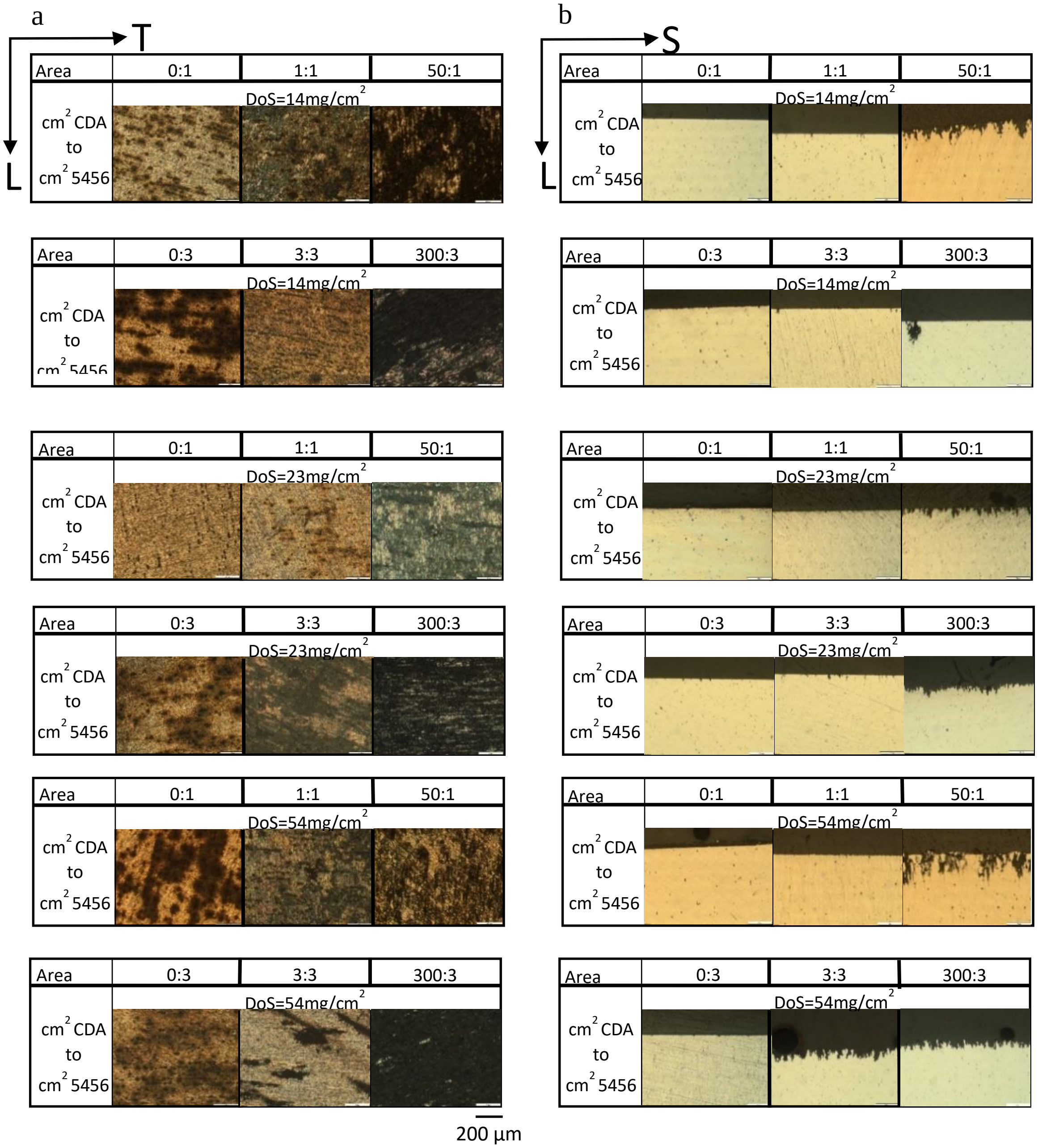

Figure 2.4: Photomicrographs of the exposed ST surface and SL cross sections of AA5456-H116 of three sensitization levels after 100 hours of galvanic coupling to CDA 706 under full immersion in 0.6M NaCl at pH 8.3 at varying cathode:anode ratios.

The mean IGC was also measured to confirm the maximum IGC trends and diminish the effects of outliers. Mean IGC measurements for 1 cm^2 and 3 cm^2 AA5456-H116 are shown in Figure 2.6 and have the same general trends as maximum IGC measurements. As the DoS increases, IGC mean tends to propagate further. The one outlier from the maximum IGC measurements at DoS 14 mg/cm^2 for the 1 cm^2 anode to cathode ratio is still evident. As the size of cathode increases, the mean IGC also increases. It is evident, as well in the maximum IGC measurements, that as the size of the anode increase, IGC grows. This anode size difference is most evident with no cathode present.

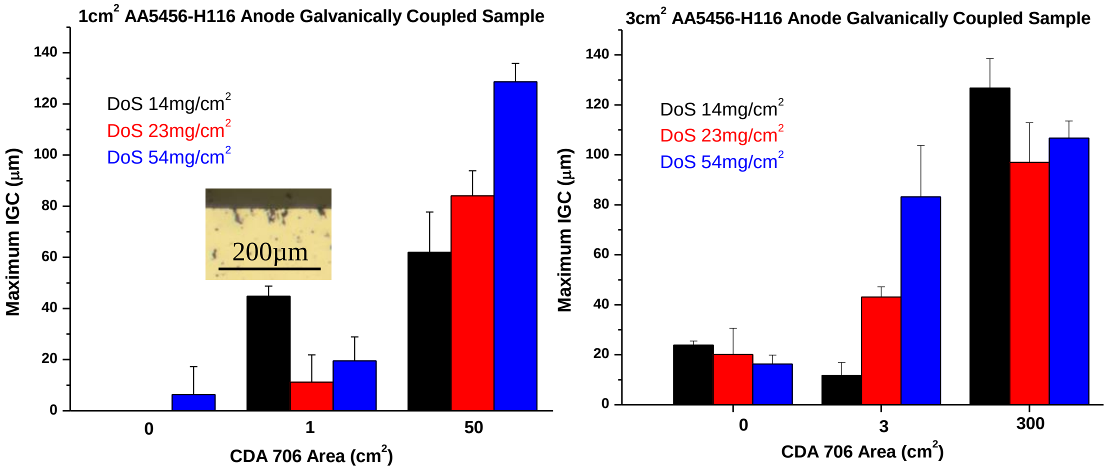

Figure 2.5: Maximum IGC and standard deviation after three depths of view of AA5456-H116 down the L plane. Maximum IGC depth for varying DoS and coupling ratios of aluminum to copper.

Coupling potential measurements, as shown in Figure 2.7, show that in general, the highest DoS has the lowest coupling potentials. Disregarding one outlier at 1 cm^2 to 1 cm^2 anode to cathode ratio, the lowest DoS measured (14 mg/cm^2) has the most positive coupling potential. As the area ratio of cathode to anode increases, the coupling potential becomes more positive. The anode area has no effect at low area ratios, as is apparent in the coupling results with no cathode and the 1 cm^2:1 cm^2 and 3 cm^2:3 cm^2 galvanic couples, with the exception of a 300 cm^2 cathode. When 1 cm^2 AA5456-H116 was coupled to 50 cm^2 CDA 706, it had greater potential than 3 cm^2 of AA5456-H116 coupled to 300 cm^2 of CDA 706.

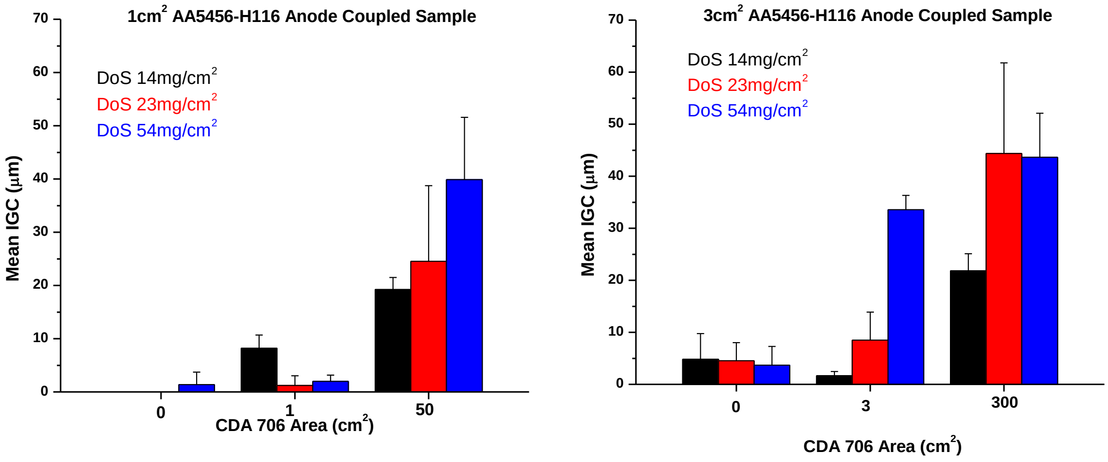

Figure 2.6: Mean IGC and standard deviation after three depths of view of 5456-H116 down the L plane. Mean IGC depth for varying DoS and coupling ratios of aluminum to copper.

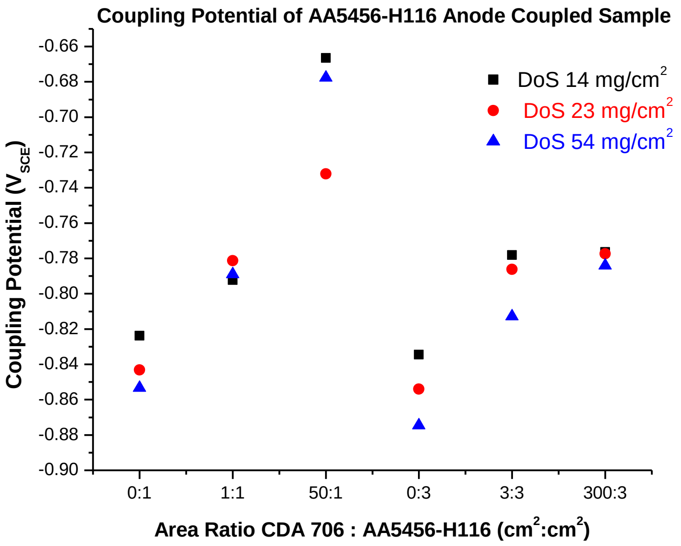

Figure 2.7: Coupling potential of varying AA5456-H116 sensitizations and CDA 706 at varying area ratios for 1 cm^2 and 3 cm^2 anodes

Coupling current densities, as shown in Figure 2.8, display the coupling current as a function of DoS and coupling area ratios of AA5456-H116 to CDA 706. DoS does not show any trend with coupling potential. Varying area ratios of cathode to anode have limited effects. When changing the size of the anode, from 1 cm^2 to 3 cm^2, the coupling current density is not affected. With no CDA 706 coupled, the coupling current density remains at 0 mA/cm^2 regardless of anode size. When the ratio of cathode increases to 1 cm^2:1 cm^2 and 3 cm^2:3 cm^2, they are comparable coupling current densities. The coupling current density of the 3 cm^2:300 cm^2 AA5456-H116:CDA 706 ratio compared to the 1 cm^2:50 cm^2 ratio is approximately doubled in value.

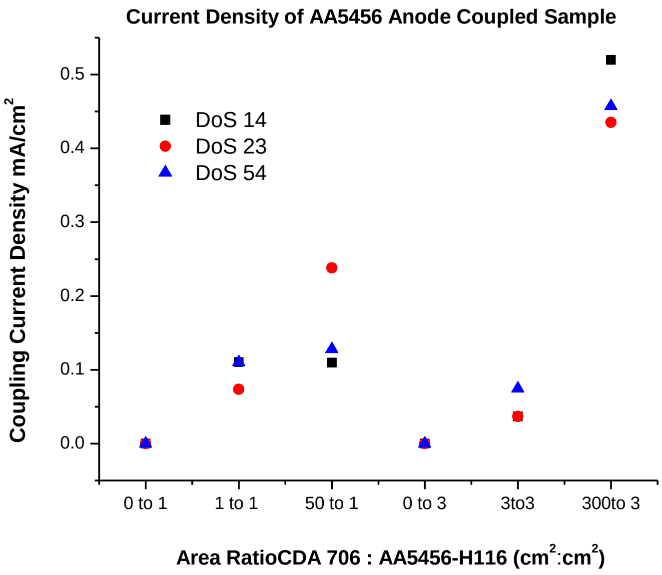

Figure 2.8: Coupling current densities of varying AA5456-H116 sensitizations and CDA 706 at varying area coupling ratios for two different anode sizes.

Coupling potential vs both coupling current density and the current as seen in Figure 2.9a&b corroborate the trend seen in Figure 2.7 for varying DoS, and areas of AA5456-H116, and area of CDA 706. Specific area ratios of CDA 706: AA5456-H116 cluster potential and current densities together. Figure 2.9b also correlates with Figure 2.8 showing that with increasing cathode:anode ratio, the potential increases. The coupling current density and current increase with cathode:anode ratio, with the exception of the 300cm^2 CDA 706. For this case, with 300cm^2:3cm^2 CDA 706 to AA5456-H116, the potential increases, but the current is less than that of a 50cm^2:1cm^2 ratio.

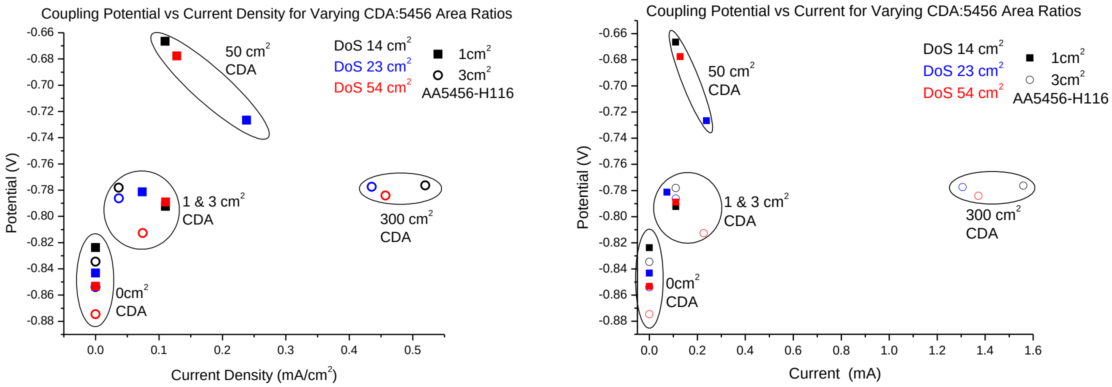

Figure 2.9: a. Coupling potential vs current density b. coupling potential vs current; for varying area ratios of CDA 706 to sensitized AA5456-H116

Figure 2.10 shows the polarization curves from Figure 2.2 overlaid with the potential and current measurements from Figure 2.9b. These current measurements are overlaid in hollow squares (1 cm^2) and hollow circles (3 cm^2). The coupling potentials are shown to closely correlate to expected values based on the overlay of CDA 706 and AA5456-H116 polarization curve potentials in the -0.8 V region. The currents measured from coupling also closely correlate with those expected from the polarization plots. It can be seen that the best correlation of coupling potential and coupling current are with the reverse polarization curves as expected due to AA5456 reversing back past its passive region towards a lower reversible potential.

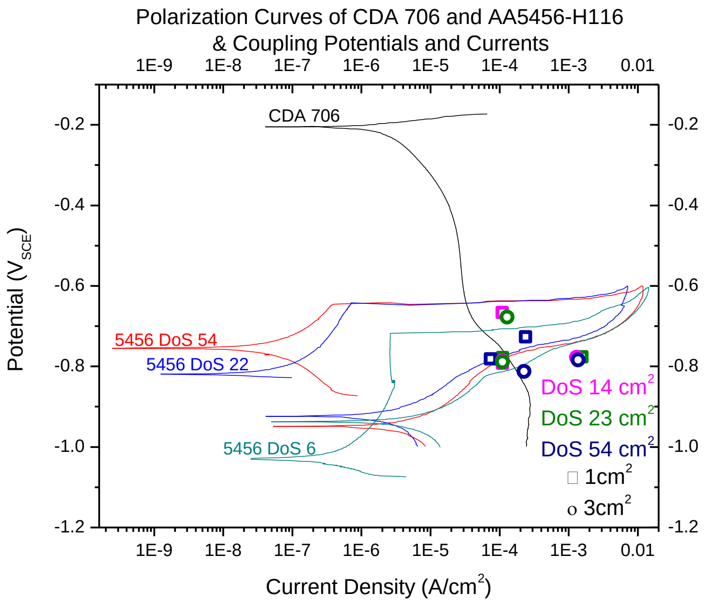

Figure 2.10: Polarization curves of CDA 706 and AA5456-H116 of DoS 54, 23, & 6 mg/cm^2 in 0.6M NaCl overlaid with coupling potential and current measurements from galvanic coupling tests with AA5456-H116 of DoS 54, 23, and 14 mg/cm^2 and CDA 706 where squares represent 1cm^2 AA5456, while circles represent 3cm^2 AA5456 samples

The quantity of fissures from the AA5456-H116 samples, shown in Figure 2.11, grow with increasing area ratio of cathode to anode. Anode size also has an effect. With 0 cm^2 and 1 cm^2 cathode, the number of fissures is greater with a larger anode. However, with the 50 cm^2 and 300 cm^2 cathode, this anode size is less relevant. With only two exceptions, 1 cm^2:1 cm^2 and 1 cm^2:50 cm^2 sample sets, the number of fissures increases with an increase in DoS.

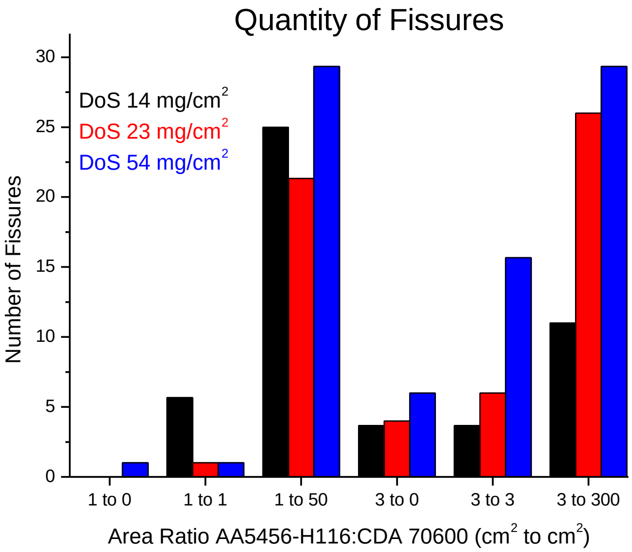

Figure 2.11: Average number of fissures averaged across 3 depths of polish on each AA5456-H116 sample

2.7 Discussion

AA5XXX series alloys, as they sensitize, become susceptible to IGC damage. When coupled to less active metals such as CDA 706, the damage is exacerbated. As both sensitization and coupling individually propagate IGC, together they combine to accelerate IGC. As seen in Figure 2.2, CDA 706 is more noble than AA5456-H116. Because copper sits at a higher potential, copper as well as its alloys, will not corrode when galvanically coupled with aluminum alloys in full immersion conditions. This is evident in Figure 2.3 where CDA 706 is untarnished following galvanic coupling. CDA 706 remained untarnished regardless of the area ratio of coupling with AA5456-H116.

Mizuno saw IGC effects in his monitoring of IGC as a function of cathode:anode ratio with sensitized AA5083-H131 and AISI 4340 steel comparable to those seen in this work [30]. Figure 2.4, showing surface and subsurface; has similar trends to those found by Mizuno[30]. IGC propagates further in the L direction as sensitization increases due to more β phase being present resulting in a more anodic sample. IGC also propagates further with an increase in cathode to anode ratio, as there is more cathode to facilitate anodic reduction. As DoS and area ratios increase, IGC fissures and grain fallout increase and can be confused for surface wastage. Past work shows that for AA5456-H116 DoS ≤54mg/cm^2, surface wastage dominates at current densities >0.8 mA/cm^2[39]. The maximum current densities that were seen in the coupling densities of AA5456-H116 and CDA 706 sat at least 0.275 mA/cm^2 below the 0.8 mA mark.

As Khullar saw in accelerated corrosion testing with AA5083[29], it was seen in full immersion that sample sizes of AA5456-H116 have an effect on observable IGC. With 1 cm^2 anodes and no cathode galvanically coupled, as shown in Figure 2.5, there is little to no IGC detected compared to observable IGC with a 3 cm^2 anode. It is believed that the small anode size has limited to no IGC observed due to cathodic kinetics not being sufficient to support anodic dissolution by the available cathodic current. IGC propagation can be aided by increasing cathodic sites due to increasing sample size or adding an oxidizer to the system. This variance in IGC depth becomes less prominent as the cathode size increases, however the number of fissures grows as seen in Figure 2.11.

Calculations of the mean IGC, shown in Figure 2.6 have the same trends as the maximum IGC measurements. As DoS increases, the IGC mean propagates further into the sample. The one outlier, DoS 14 mg/cm^2 and 1 cm^2:1 cm^2 anode to cathode ratio, from maximum IGC measurements is still evident but less prominent. Just as with the maximum IGC measurements and most apparent at low cathode:anode ratios, as the size of the anode increases, IGC increases corresponding to fissure quantity.

AA5456-H116 samples with higher DoS tend to have lower coupling potentials, as shown in Figure 2.7. Mizuno saw the same effect, attributing the change to anodic kinetics being more active as the sensitization increases[30]. As the coupling area ratio increased, the potential became more positive, as expected based on mixed potential theory shown in Figure 2.12. It is expected as the cathode size increases, as shown in Figure 2.12 from 50 cm^2 to 300 cm^2, the cathode line will increase, depicted from solid to dashed lines. The current density, regardless of anode size, increases with increasing cathode:anode ratio. The current density increases with area ratios, as expected form Figure 2.12. However, coupling potential decreases from 50 cm^2:1 cm^2 and 300 cm^2:3 cm^2. With increased area from fissures and maximum IGC and grain fallout, shown in Figures 2.11 and 2.5, the area of anode increases, shifting the anodic line down. The number of fissures, seen in Figure 2.11, is comparable, however there was more total IGC as shown in Figure 2.5. Although fissures are comparable, there is more grain fall out resulting in more area anode for coupling. This lowers the coupling potential as evident in Figure 2.7.

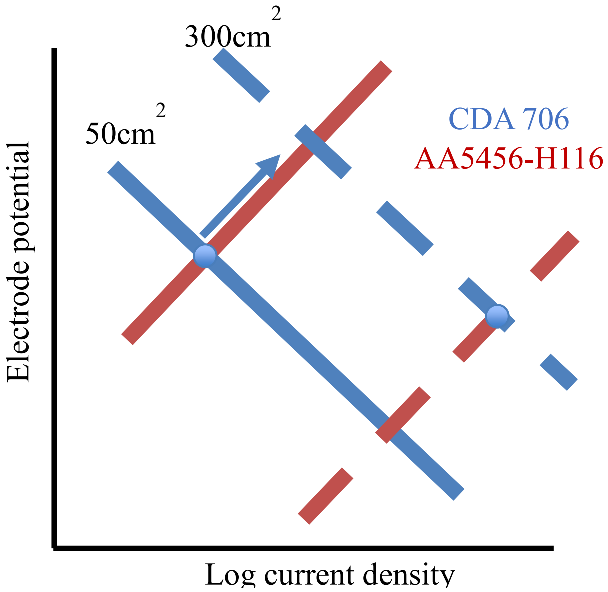

Figure 2.12: Evans diagram showing trend of cathode size for electrode potential vs log current density

2.8 Conclusions

AA5456-H116 and CDA706 galvanic coupling corrosion behavior was investigated under full immersion conditions. The influence of DoS, cathode:anode ratio, and anode size on IGC damage were investigated, as well as coupling effects on coupling potentials and coupling currents.

(1) IGC propagates very minimally at the low sensitization of DoS 14 mg/cm^2, but the maximum and mean IGC increases with increasing sensitization. More β phase is present with increasing sensitization, resulting in the samples being more anodic, and accelerated IGC.

(2) As the size of the anode, AA5456-H116, increases, IGC further propagates. As the anode size increases from 1 cm^2 to 3 cm^2, IGC increases. There are many grain boundaries exposed on the ST face for both the 1 and 3 cm^2 samples that would allow for IGC propagation. Therefore, this phenomenon is due to insufficient cathodic kinetics for anodic dissolution. This is most evident at the lowest cathode:anode ratios.

(3) As the size of the cathode increases, regardless of the size of the anode, IGC accelerates. This is due to more cathode area to accelerate anodic corrosion.

(4) Galvanic coupling potential fluctuates with DoS. Higher sensitizations yield a lower coupling potential. With increasing cathode size, the potential rises. The anode area has no effect on the coupling potential. However, at the highest cathode areas investigated, potential dropped. The coupling potential decreases due to surface area of the anode increasing with increased grain fallout and IGC propagation.

(5) The coupling current density is not affected by DoS or the size of the anode. However, as the cathode increases, so does the current density.

2.9 Acknowledgments

Financial support from the Office of the Undersecretary of Defense Technical Corrosion Collaboration via the USAFA Contract FA7000-14-2-0010 is gratefully acknowledged.

2.10 References

1. McCafferty, E. *Introduction to Corrosion Science*. (2009).
2. Kelly, R., Scully, J., Shoesmith, D. & Buchheit, R. *Electrochemical Techniques in Corrosion Science and Engineering*. **20021014,** (2002).
3. Mizuno, D. & Kelly, R. G. Galvanically Induced Intergranular Corrosion of AA5083-H131 Under Atmospheric Exposure Conditions - Part I –Experimental Characterization. 1–6 (2013).
4. Golumbfskie, W. private communication.
5. Lim, M. L. C., Kelly, R. G. & Scully, J. R. Overview of intergranular corrosion mechanisms, phenomenological observations, and modeling of AA5083. *Corrosion* **72,** 198–220 (2016).
6. Birbilis, N. *et al.* A Survey of Sensitisation in 5xxx series Aluminium Alloys. *Corrosion* **72,** 144–159 (2016).
7. McMahon, M., Steiner, P., Lass, A. & Burns, J. The Effect of Loading Orientation on the Stress Corrosion Cracking of Al-Mg Alloys. *Corrosion* **73,** 347–361 (2017).
8. https://www.vesseltracker.com/en/Ships/Kilo-Moana-9229037.html.
9. Mary Parker (personal communication). (2018).
10. Greene, H. J. Evaluation of Corrosion Protectin Methods for Aluminum Metal Matrix Composites. (1992).
11. Khullar, P., Badilla, J. V & Kelly, R. G. Intergranular Corroson in Al-Mg 5XXX Alloys Under Atmospheric Exposures. in *NACE* 1–10
12. Montgomery, J. S. & Chin, E. . The AMPTIAC Quarterly. **8,** 15–20 (2004).
13. Searles, J. L., Gouma, P. I. & Buchheit, R. G. Stress corrosion cracking of sensitized AA5083 (Al-4.5Mg-1.0Mn). *Metall. Mater. Trans. A Phys. Metall. Mater. Sci.* **32,** 2859–2867 (2001).
14. Oguocha, I. N. A., Adigun, O. J. & Yannacopoulos, S. Effect of sensitization heat treatment on properties of Al-Mg alloy AA5083-H116. *J. Mater. Sci.* **43,** 4208–4214 (2008).
15. Lerman, D. & Capaccio, T. Navy Finds 'Aggressive' Corrosion on Austal's Combat Ship. *Bloomberg* (2011). Available at: https://www.bloomberg.com/news/articles/2011-06-17/navy-finds-aggressive-corrosion-on-austal-s-combat-ship-1-.

16. CORROSION FAILURE: LCS 2 USS Independence Naval Ship Engine Corrosion. *NACE International* Available at: https://www.nace.org/CORROSION-FAILURE-LCS-2-USS-Independence-Naval-Ship-Engine-Corrosion.aspx.
17. Schleich, W. *Typical failures of CuNi 90/10 seawater tubing systems and how to avoid them*.
18. Davis, J. R. Corrosion of Aluminum and Aluminum Alloys. *Mater. Park. OH ASM Int.* 75–83 (1999).
19. Crane, C. B. & Gangloff, R. P. Stress Corrosion Cracking of Low Temperature Sensitized AA5083. *Corrosion* **72,** 1–14 (2011).
20. Jones, R. H., Baer, D. R., Danielson, M. J. & Vetrano, J. S. Role of Mg in the Stress Corrosion Cracking of an Al-Mg Alloy. *Metall. Mater. Trans. A* **32,** 1699–1711 (2001).
21. McMahon, M. E., Steiner, P. J., Lass, A. B. & Burns, J. T. The Effect of Temper and Composition on the Stress Corrosion Cracking of Al-Mg Alloys. *Corrosion* **73,** 347–361 (2017).
22. Aylor, D. M., Hays, R. A. & Marshall, L. S. *Galvanic Corrosion Evaluation of High Performance Naval Seawater Valve Materials in Quiescent, Natural Seawater*. (2000).
23. Hack, H. P. & Wheatfall, W. W. Evaluation of Galvanic and Stray Current Corrosion in 70/30 Copper-Nickel/Alloy 625 Piping Systems. *CARDIVNSWC-TR-61--94/15* (1995).
24. Hack, H. P. & Wheatfall, W. W. *Comparison of Cathodic Protection Currents on 70/30 Copper-Nickel and Alloy 625 Piping Systems*. *CARDIVNSWC-TR-61--94/14* (1995).
25. Srinivasa Rao, A. *Characterization of the Surface Film Growth During the Electrochemical Process: Part III (70 % Copper- 30 % Nickel System). CARDIVNSWC - TR - 61 - 98 - 24* (1998).
26. Tuthill, A. H. Guidelines For the Use of Copper Alloys In Seawater. *Mater. Perform.* **26,** 12–22 (1987).
27. North, R. F. & Pryor, M. J. The Influence of Corrosion Product Structure on the Corrosion Rate of Cu-Ni Alloys. *Corros. Sci.* **10,** 297–311 (1970).
28. Mizuno, D. & Kelly, R. G. Galvanically Induced Intergranular Corrosion of AA5083-H131 Under Atmospheric Conditions Part 2 Modelling the damage. *Corrosion* **69,** 681–692 (2013).
29. Khullar, P. & Kelly, R. G. *Investigation of Corrosion Testing Methods and Selected Corrosion Protection Strategies on Modern High-Performance Alloys that Affect Land Vehicle Structural Integrity (2012-2016)*. (2016).
30. Mizuno, D. & Kelly, R. G. Galvanically Induced Intergranular Corrosion of AA5083-H131 Under Atmospheric Conditions Part 2 Modelling the damage. *Corrosion* **69,** 681–692 (2013).
31. Holtz, R. L., Pao, P. S., Bayles, R. A., Longazel, T. M. & Goswami, R. Corrosion-fatigue behavior of aluminum alloy 5083-H131 sensitized at 448 K (175 C). *Metall. Mater. Trans.*

A Phys. Metall. Mater. Sci. **43,** 2839–2849 (2012).

32. Lim, M. L. C. *et al.* Model to predict intergranular corrosion propagation in three dimensions in AA5083-H131. *Mater. Des.* **96,** 131–142 (2016).

33. Lim, M. L., Scully, J. R. & Kelly, R. G. Intergranular Corrosion Penetration in AA5083 as a Function of Electrochemical and Metallurgical Conditions service. **69,** 35–47 (2013).

34. Schleich, W. Typical failures of CuNi 90/10 seawater tubing systems and how to avoid them. *Eng. Struct.* **49,** (2004).

35. ASTM G67-04, 'Standard Test Method for Determining the Susceptibility to Intergranular Corrosion of 5XXX Series Aluminum Alloys by Mass Loss After Exposure to Nitric Acid (NAMLT Test)'. (2004).

36. M. Tiryakioglu, J. T. S. Physical Metallurgy and the Effect of Alloying Additions in Aluminum Alloys. in *Handbook of Aluminum* (ed. G.E. Totten, D. S. M.) (Marcel Dekker, Inc, 2003).

37. Tattersall, C. Manual for Depth Analysis Code.

38. Tattersall, C. & Kelly, R. G. Automated Quantification of Corrosion Damage from Cross-sectional Micrographs. *to be Submitt. to Corros.*

39. Burns, C. *Understanding the Intergranular Corrosion Kinetics in AA5456-H116 as a Function of Electrochemical and Metallurgical Variables*. (2017).

40. Abbott, W. H. A Decade of Corrosion Monitoring in the World ' s Military Operating Environments -A Summary of Results. *Columbus, OH DoD CorrDefense* (2008).

41. Katona, R. Personal Communication. (2017).

42. Macha, Erica N.;Dante, J. F. Effect of Cyclic RH & Preliminary Sensor Analysis. Personal Communication. (2018).

43. Neiser, E. B. Atmospheric Corrosion of Silver and its Relation to Accelerated Corrosion Testing. (University of Virginia, 2010).

44. ASTM B825-13: Standard Test Method for Coulometric Reduction of Surface Films on Metallic Test. *Annu. B. ASTM Stand.* (2002). doi:10.1520/B0825-13.2

45. NIH. Image J.

46. Horton, D. J., Sanders, C. E., Anderson, R. M., Davis, R. S. & Lemieux, E. J. Accelerated Field Exposure using Seawater Spray: A Comparison to Traditional Atmospheric Test Methods. *NACE Corros. Conf.* **Paper No.,** 1–11 (2017).

47. Lim, M. L. C. Intergranular Corrosion Propagation in Sensitized Al-Mg Alloys. (University of Virginia, 2016).

3 Outdoor Exposure of Galvanically Coupled Sensitized AA5456-H116 and CDA 706

3.1 Abstract

Samples of galvanically coupled AA5XXX-H116 and CDA 706 were mounted on the *R/V Endeavor*, ported out of Narragansett, Rhode Island and on the *R/V Kilo Moana* ported out of Honolulu, Hawaii for 6 and 12-month exposures. AA5083-H116 and AA5456-H116 samples at varying degrees of sensitization (DoS) had CDA 706 cupronickel inserts of ¼” and 3/8” diameter press fitted to form the samples. It was found that geolocation of samples and relative humidity (RH) affect intergranular corrosion (IGC) propagation and interaction distance/throwing power. Increased DoS as well as increased CDA 706 insert diameter also increase IGC. The alloy variation of AA5083-H116 and AA5456-H116 has little influence on IGC trends.

3.2 Overview

This chapter focuses on results of outdoor exposure testing of samples on two University-National Oceanographic Laboratory System (UNOLS) research vessels (R/V), the *R/V Endeavor* and *R/V Kilo Moana*. Naval ships utilize AA5XXX series aluminum alloys as well as CDA 706 cupronickel pipes. In some cases, these two alloys are in intimate contact and exposed to the same marine atmosphere, thus meeting the requirements for galvanic interaction. It is of importance to study and characterize the intergranular corrosion (IGC) effects of these galvanic couples in real-world conditions. By investigating the IGC of these couples in a service environment, the effects of AA5XXX sensitization and CDA coupling effects can be studied. These exposure results will aid in predicting IGC propagation of AA5XXX on naval vessels as a function of varying parameters including sensitization, CDA:5XXX ratio, RH (relative humidity), and geolocation.

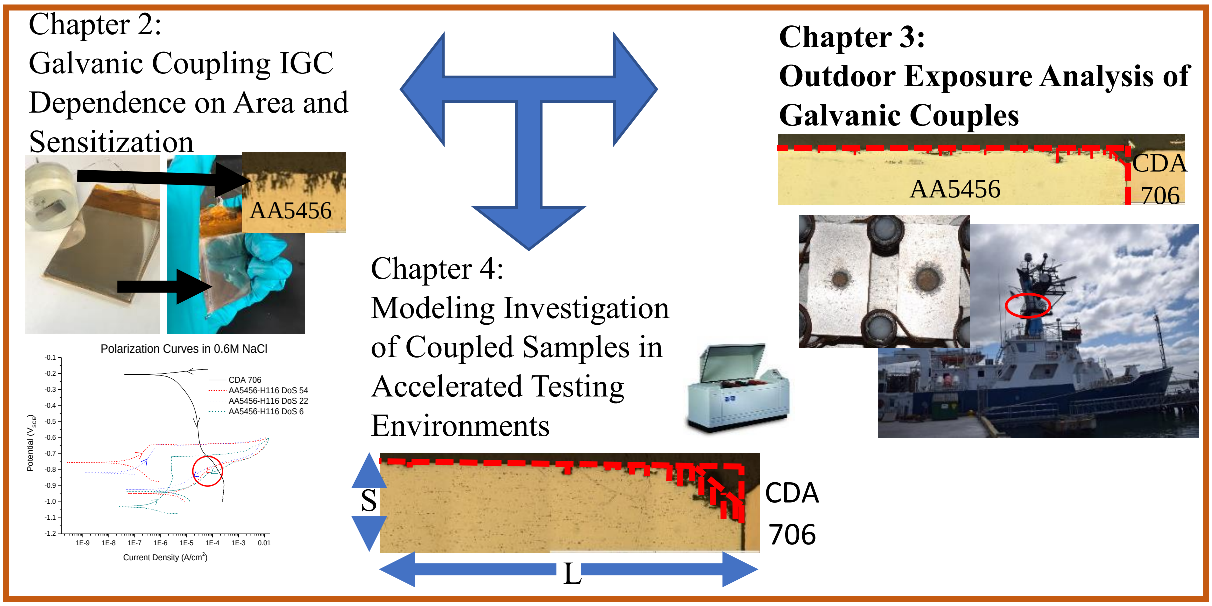

Schematic for Thesis Organization

3.3 Introduction

AA5XXX alloys are utilized increasingly in naval ship superstructures. These aluminum-magnesium alloys are selected because of their strength, corrosion resistance, ductility, and weldability[14,18,31]. These AA5XXX alloys, with time and temperature, sensitize. This degree of sensitization (DoS) can increase at temperatures as low as 50°C in service conditions[14]. When these samples sensitize, the β phase (Al_3Mg_2) precipitates at the grain boundaries[32]. The β phase is more anodic than the α bulk phase. This anodic β phase along the grain boundaries creates a pathway for IGC propagation. If mechanical stress is also present, intergranular stress corrosion cracking (IGSCC) can occur. The microstructure of AA5XXX, exemplified by the electrolytic Barkers etch micrograph of AA5083-H131 in Figure 3.1[5], showing elongated grains on the longitudinal by short transverse (LS) and short transverse (ST) planes, and wide grains on the long transverse (LT) plane. IGC growth rate, studied in detail by Lim, was found to be comparable in both the L and T, but not in the S direction, due to this elongated grain structures[5].

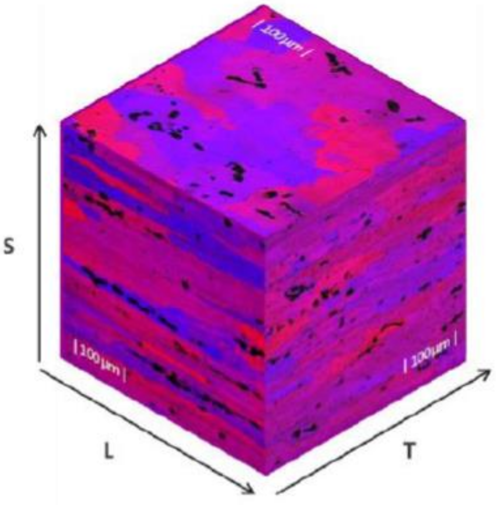

Figure 3.1[5]*: Microstructure of AA5083-H113 after Barkers etching to show grain structure*

In naval service, these AA5XXX samples are not only sensitized, but galvanically coupled to more noble materials. Naval vessels utilize CDA 706 pipes for transporting seawater, and in some cases these pipes exit the ship superstructure through the AA5XXX superstructure of these ships. CDA 706 is used for water and heat exchange systems due to its uniform corrosion resistance as well as bacteriostatic and anti-microfouling properties[17,22]. CDA 706 does suffer dissolution, regardless of this low corrosion rate, and as a result, CDA 706 corrosion products are carried by seawater and deposited on the superstructures of the AA5XXX vessels. This direct galvanic couple would be expected to accelerate IGC propagation on sensitized AA5XXX.

Historically, laboratory testing has been used to investigate IGC propagation due to galvanic coupling of varying alloys, however little work has been performed in exposures even though these materials are exposed to atmospheric conditions. Full immersion testing, as well as thin film testing has been performed to study various galvanic couples with AA5XXX[3,29,30]. The aim of this work is to investigate conditions the effect of conditions these alloys experience when exposed in service. Geolocation, coupled metals, DoS, and silver exposure[40], which is used as a corrosion monitor, are used to investigate corrosion damage.

3.4 Materials

5456-H116 ¼” thick panels were provided by the Naval Surface Warfare Center-Carderock Division (NSWCCD), the composition of which can be seen in Table 3.1. 5083-H116 ¼” thick plates were provided by Metal Samples, the composition of which is displayed in Table 3.2. Both 5XXX alloys are special strain hardened and corrosion resistant, as signified by their H116 temper[36]. CDA 706, a copper nickel 90/10 alloy shown in Table 3.3 was provided by Metal Samples in ¼” and 3/8” diameters. Silver (Ag) samples, specifically UNS P07010 99.99%, were provided by Metal Samples.

Table 3.1: Alloy composition of AA5456-H116 ¼” provided by NSWCCD (by materials certification)

AA5456-H116								
Element	Al	Mg	Fe	Si	Cr	Zn	Ti	Cu
Wt %	Rem.	5.2640	0.1830	0.1570	0.0930	0.0560	0.0263	0.0240

Table 3.2: Alloy composition of AA5083-H116 ¼” provided by Metal Samples (by materials certification)

AA5083-H116												
Element	Al	Mg	Mn	Fe	Si	Zn	Ti	Cu	Cr	Be	Pb	Ni
Wt %	Rem.	4-4.5	0.4-0.7	0.5	0.4	0.25	0.15	0.1	0.05-0.25	0.05	0.05	0.05

Table 3.3: Alloy composition of CDA 706 provided by Metal Samples (by materials certification)

CDA 706					
Element	Cu	Ni	Fe	Mn	Impurities
Wt %	87.778	9.948	1.453	0.793	Rem.

3.5 Experimental Procedures

3.5.1 Test Matrix

Two locations were selected for outdoor exposure testing. University-National Oceanographic Laboratory System (UNOLS) locations in Hawaii and Rhode Island were gracious enough to accommodate in testing and retrievals. Panels were assembled in the laboratory, following the matrix in Figure 3.2, and mounted on the *R/V Endeavor* and *R/V Kilo Moana*. Four panels were placed on each vessel, with one panel to be removed every six months resulting in a maximum of two years exposure. Panels were mounted to begin the exposures on 6/9/16 for the *R/V Endeavor* and mounted on 11/7/16 on the *R/V Kilo Moana*. With each retrieval, supplemental meteorological weather data were collected and returned from the research vessels. As of February 2018, both 6 and 12-month removals have been completed and analyzed.

The matrix for the exposure panels as well as an assembled panel can be seen in Figure 3.2 a & b. Each panel contained six samples of size 1”x 1.5” x 1/4” of AA5083-H116 and AA5456-H116. The AA5083-H116 samples, in pairs, were sensitized to 10, 23, and 54 mg/cm^2 by heat-treating them at 100°C for 0, 7, and 45 days. The AA5456-H116 samples, in pairs, were sensitized to 14, 23, and 54 mg/cm^2 by heat-treating them at 100°C for 0, 3 and 14 days. These sensitization times were validated using ASTM G67[35] nitric acid mass loss test (NAMLT). All of the aluminum samples were polished to 1200 grit using silicon carbide paper. One of each sensitization of AA5083-H116 and AA5456-H116 had a ¼” CDA 706 rod press-fitted into a hole drilled in its center. The other samples of each sensitization had a 3/8” CDA 706 rod press fitted in the center. The back of these coupled samples was taped using Kapton® tape. In addition, each panel contained two unsensitized samples of size 1” x 2” x ¼”. One of these was AA5083-H116 and one was AA5456-H116, both were polished to 1200 grit using silicon carbide paper. One Ag sample was also used on each sample, and polished to 1200 grit as well. This work presents the first year of exposure returns. The panels on the *R/V Endeavor,* ported in Narragansett, Rhode Island were mounted on the lower mast platform. The panels on the *R/V Kilo Moana*, ported in Honolulu, Hawaii, were mounted above the pilot house. The location of sample exposures on each research vessel can be seen in Figure 3.3.

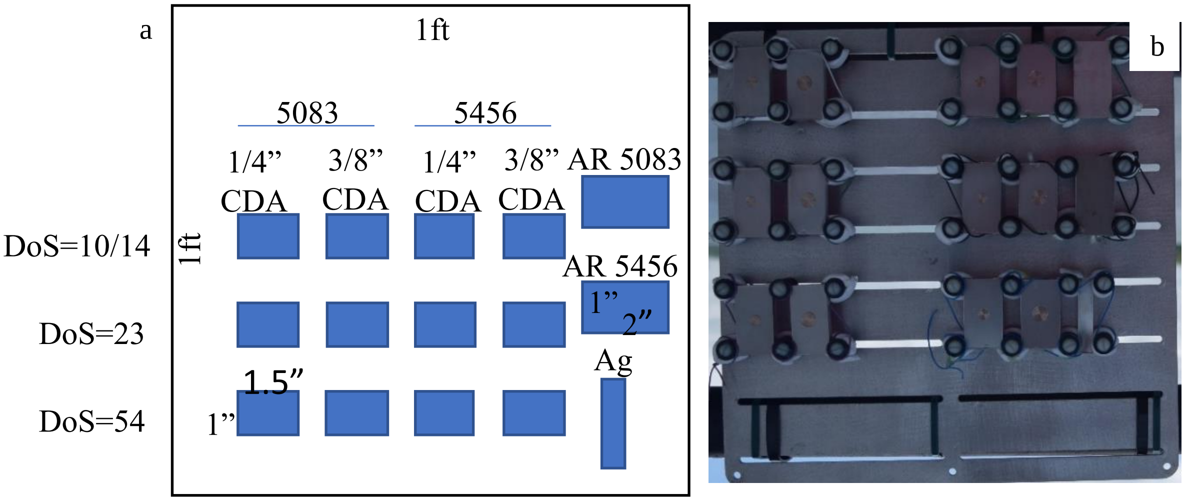

Figure 3.2: a. Matrix of each outdoor exposure panel measuring 1ft^2. Each panel contained 6 AA5083-H116 and six AA5456-H116 samples heat treated to varying degrees of sensitization with either ¼” or 3/8” CDA 706 inserts. As received (AR) unsensitized AA5083-H116 and AA5456-H116 samples and one Ag sample were also placed on each panel. b. Assembled panel

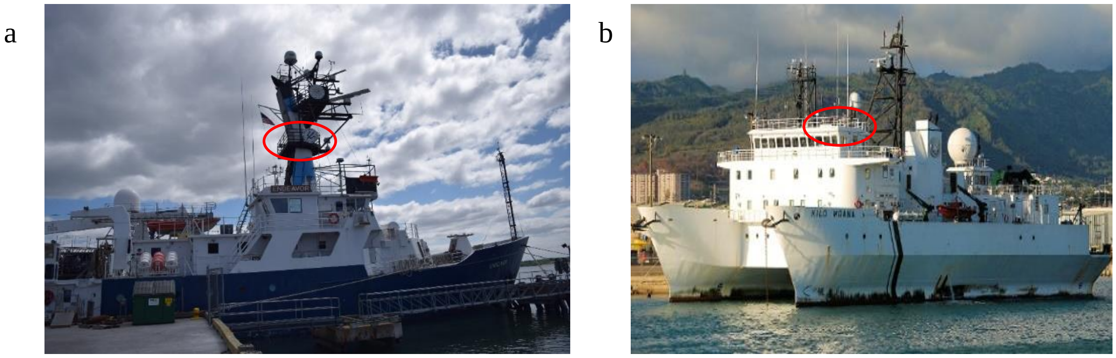

Figure 3.3: a. Location of samples exposed on the R/V Endeavor b[8]*. Locations of samples exposed on the R/V Kilo Moana*

3.5.2 Exposure Data Collection

Each research vessel collects large amounts of meteorological data for their own research purposes. The *R/V Endeavor* collects data every 10 minutes at port as well as at sea. The *R/V Kilo Moana* collects data every second while at sea, however data were scaled down to one point per minute for easier data analysis. For the days the *R/V Kilo Moana* did not collect data, it remained in port in Honolulu, Hawaii. Thus, no data points exist for those times. There are a few days that the *R/V Endeavor* failed to collect data, however not enough to influence any determinations made over the 6 and 12-month retrievals. For this research, geolocation and relative humidity were the only two data collections investigated.

For geolocation determination, the average of 10 latitude and longitude points in the middle of the record for each day were taken to be the ships location. These locations were plotted to show the samples cruise on the *R/V Endeavor* and *R/V Kilo Moana* shown in Figure 3.4 a & b respectively using copypastemap.com. The first six months are highlighted in red, the second six months are highlighted in blue resulting in the 12-month samples being exposed at all those locations. All the humidity data was plotted over time for using a MATLAB code[41]. This code was written to calculate the percentage of RH values above 76%, below 50%, and for values between, if they are increasing or decreasing in RH from point to point. Based on past work by Macha and Dante, values >76% were assumed to be wet, <50% were assumed to be dry, and in between was rising and falling humidity[42].

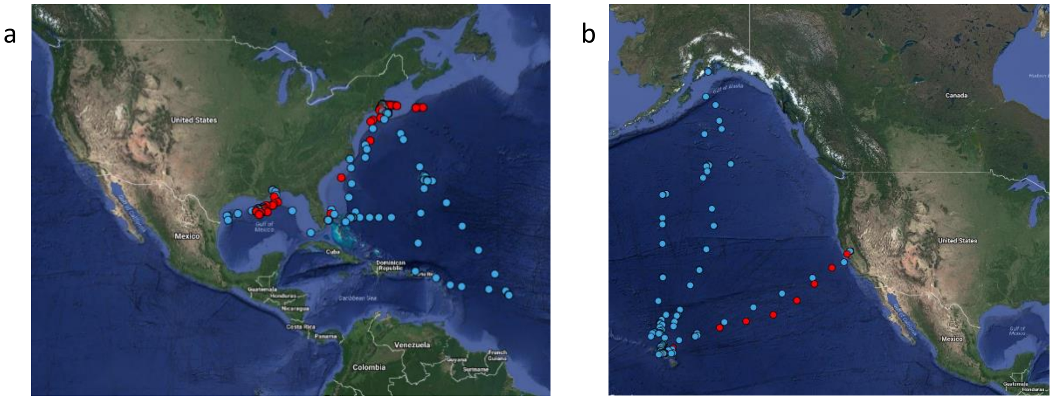

Figure 3.4: a. Locations of R/V Endeavor (1st 6 months in red, in 2nd 6 months blue) b. Locations of R/V Kilo Moana (1st 6 months in red, in 2nd 6 months blue)

3.5.3 ASTM G-67

As-received samples placed on exposure panels, were tested for a change in sensitization upon return. When returned, both 5XXX samples were cut to size and tested following ASTM-G67[35] nitric acid mass loss test (NAMLT).

3.5.4 Coulometric Reduction – Silver

Each of the returned Ag samples had three reduction trials performed using a Princeton Applied Research 263A potentiostat. A 0.1M Na_2SO_2, pH=10 electrolyte was de-aerated with N_2 for one hour and sequentially transferred to a flat cell, where it was de-aerated for an additional 10 minutes prior to reduction. Ag samples, with an area of 1 cm^2, were galvanostatically reduced utilizing a constant current of -0.1 mA. Following reduction, as shown in Figure 3.5, the 1st derivative of each scan was plotted against the original data. Following Neiser's work[43], the 1st derivative of reduction is known to correlate to time of reduction. The charge of reduction was calculated using equation 1 and converted to thickness using equation 2 and 3 from ASTM B825[44].

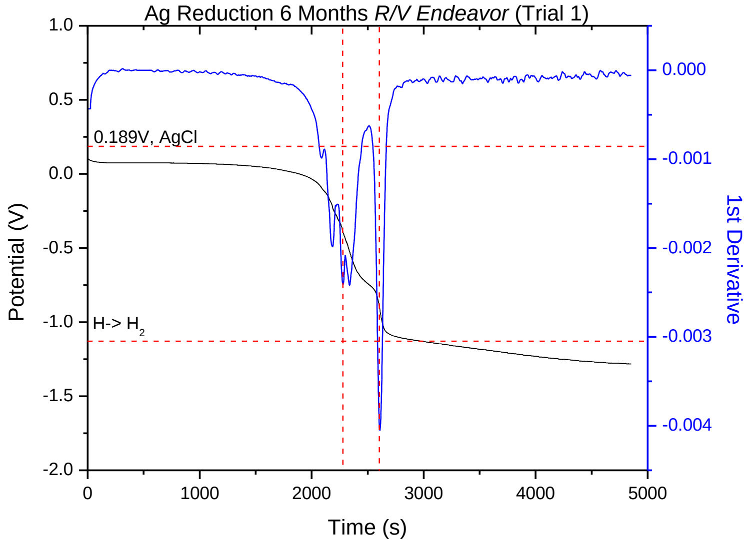

Figure 3.5: Ag Reduction curve for 1 trial of R/V Endeavor 6-month return, plotting potential (V_{SCE}) vs time (s), and the derivative of the potential vs time to show reduction time

$$\boldsymbol{Q = It} \qquad \text{Equation 1}$$

Where Q=Charge (C)

I=current (mA)

t=time (s)

$$\boldsymbol{T = \frac{itK}{a}} \qquad \text{Equation 2}$$

$$\boldsymbol{K = \frac{10^5 M}{NFd}} \qquad \text{Equation 3}$$

Where T=thickness (Å)

i=current (mA)
t=time (s)
a=area (cm^2)
K=conversion factor
M=gram-molecular weight of substance
N=number of faradays to reduce 1-gram substance (1 for AgCl, 2 for Ag_2S)
F=Faraday's constant ($9.65x10^4$ C)
d=density substance reduced (g/cm^3)

3.5.5 Coulometric Reduction – CDA 706

CDA 706 3/8" inserts from AA5083-H116 DoS 10 mg/cm^2 and AA5456-H116 DoS 14 mg/cm^2 were coulometrically reduced. For one hour, a solution of 0.1M Na_2CO_4, pH=10 was de aerated with N_2, and subsequently transferred to a flat cell and de aerated for an additional 10 minutes. CDA 706 samples were galvanostatically reduced utilizing a constant current and a scan rate of 1 pt/sec vs SCE using a PAR 263A. Samples were reduced with an area of 0.5 cm^2, at -0.05 mA, collecting data 1 pt/sec. The first derivative of reduction data was plotted against the potential vs time data to determine the reduction time, as was done with Ag. This time was used in equations 1-3 to determine the Q and thickness of corrosion products.

Six-month CDA 706 exposure returns were reduced. Twelve month returns reductions were attempted with unreliable results. Samples, after many attempts were not able to be coulometrically reduced. To investigate these corrosion products, Raman, x-ray photoelectron spectroscopy (XPS), and x-ray diffraction (XRD) were utilized. These data can be found in the Appendix A. The scans from these varying techniques showed varying corrosion products on the surface of CDA 706, however they do not support each other.

3.5.6 Surface Damage

Image J[45] was used for surface damage quantification of surface damage on AA5456-H116 and cathodically protected CDA 706. Macroscopic images of each sample, without cleaning and pre-cross-sectioning, upon return were used to quantify surface damage of the AA5456-H116. Eight equidistant measurements were collected and averaged around the AA5456-H116 to measure the distance of visible surface damage surrounding the AA5456-H116 and CDA 706 interface as shown in Figure 3.6a. These measurements were used to determine throwing power of CDA 706 across the AA5XXX surface.

Following all CDA 706 testing above, samples were sonicated in methanol followed by isopropyl alcohol for 10 minutes each. Each CDA 706 had ¼ of each insert imaged using a HIROX KH 7700. Eight distances were measured and averaged to show the distance of CDA 706 cathodically protected, as seen in Figure 3.6b. This cathodically protected area was highly reflective in the optical microscope.

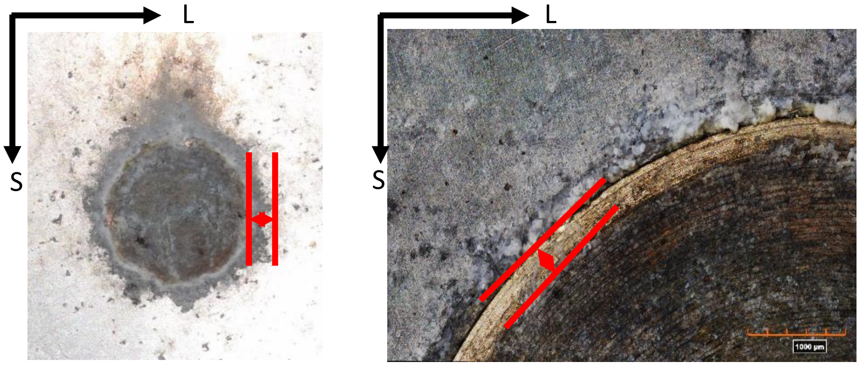

Figure 3.6: a. Surface damage measurement on AA5456-H116 surface b. Un-corroded CDA 706 measurement

3.5.7 Cross Sectioning – IGC Characterization

Exposure samples were cut in 4 cross sections along the L direction, with the two edge pieces halved along the T direction as diagramed in Figure 3.7. After cross-sectioning, the center pieces were mounted to expose the CDA 706 and the AA5XXX SL face, while the four edge pieces were mounted to expose the ST faces. All samples were polished to 1200 grit using silicon carbide paper, followed by 3 and 1 μm diamond suspension, and 0.05 μm colloidal silica for imaging using an optical microscope. For edge pieces, not having any influence from the CDA 706 due to being ample distance away, the maximum edge IGC observed in the S direction was measured as a baseline for IGC on the sample.

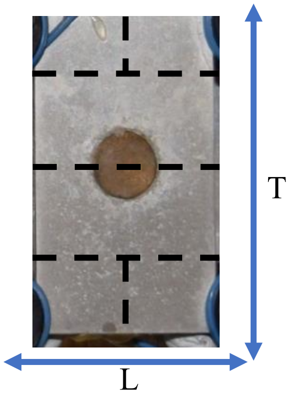

Figure 3.7: Diagram of Cross-Sectioning of Exposure Returns

Summations of IGC corrosion area was analyzed using Image J. Each image was opened in Image J, shown in Figure 3.8a, and using the analyze tool, the scale was set to the known distance using the line measurement tool. Shown in Figure 3.8b, the area of inerest was cropped, and the polygon tool was used to select and fill the corner that is not corroded, but a result of assembly, shown in Figure 3.8c. The polygon tool was used to selectively edit, and fill areas of constituent particles in Figure 3.8d. The cropped image was changed to 8bit, and the threshold was was selected, represented in Figure 3.8e. The analyze particles tool was utilized with display results, clear results, summarize, and include holes selected. Summarize was then selected to calculate the area of damage in red in Figure 3.8e and subsequent samples. Each sample was polished to two depths, resulting in total fields of view where one field of view is the coupling interface to the edge of the sample.

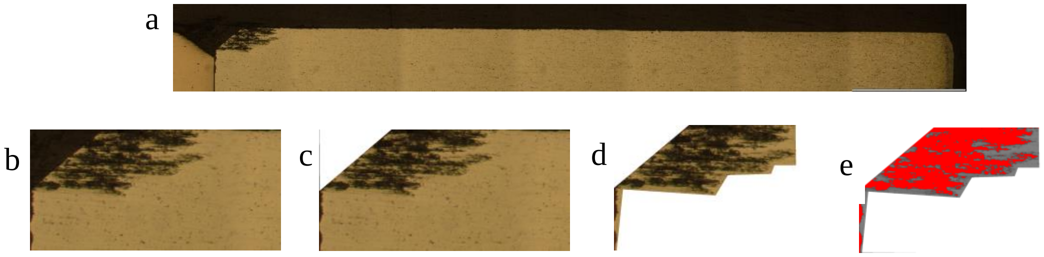

Figure 3.8: Image J Area Analysis a. Original image for analysis b. Image cropped c. Image after filling in machined area d. Image after filling in constituent particles e. Image after turned changed to black and white and threshold adjusted for area analysis

The throwing power CDA 706 of the AA5xxx samples was measured using Image J. The scale was adjusted, and using the measurement tool, the depth of IGC and distance from the edge of the coupling interface were measured. The depth of IGC every 500 µm, from 0 to 8000 µm from the coupling interface across the sample was also measured. Figure 3.9 shows a visualization of the throwing power across a cross section of one of eight fields of view of an exposure sample. These eight fields of view, again, are representative of two depths of polish and the four sides of the coupling interface following cross-sectioning.

Distance of damage away from the coupling interface was measured from the far right vertical red dashed line in Figure 3.9 at the CDA 706 and AA5XXX interface across the horizontal red dashed line to the intersection of IGC down the S direction of the sample. Depth of polish was measured from the surface datum, being the horizontal red dashed line, down the S face, to measure the IGC depth. The exception to this is the corner at the coupling interface. Due to unavoidable assembly issues, the corners where CDA 706 inserts were press fitted are slightly angled. The depths at these angled edges was measured from the AA5XXX original surface, as depicted by a diagonal dashed line. These measurements were used to investigate IGC decay over distance from the galvanic couple interface of CDA 706 and AA5XXX.

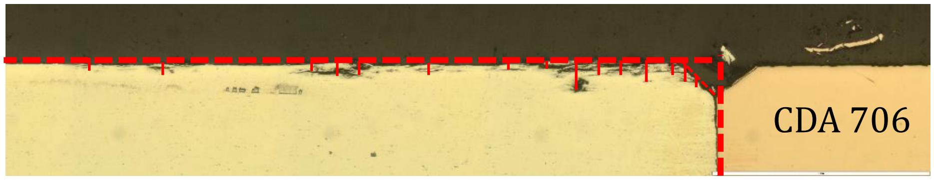

Figure 3.9: One of four fields of view, showing throwing power from CDA 706 over AA5XXXX-H116

3.6 Results

3.6.1 Humidity for *R/V Endeavor* and *R/V Kilo Moana*

Exposure samples and returned data from 6 and 12 months of the *R/V Endeavor* and the *R/V Kilo Moana* were investigated. Humidity plots for 0-6 months and 0-12 months were plotted. The *R/V Endeavor* 0-12-month RH (%) vs time (mins) is plotted in Figure 3.10, the rest of the RH over time plots can be found in the appendix. From this plot, black values represent RH >76%, red represent <50%. For values between 50 and 76%, values where RH is increasing are green, and decreasing RH values are blue. Missing values in these plots are days that data was not collected on the research vessels.

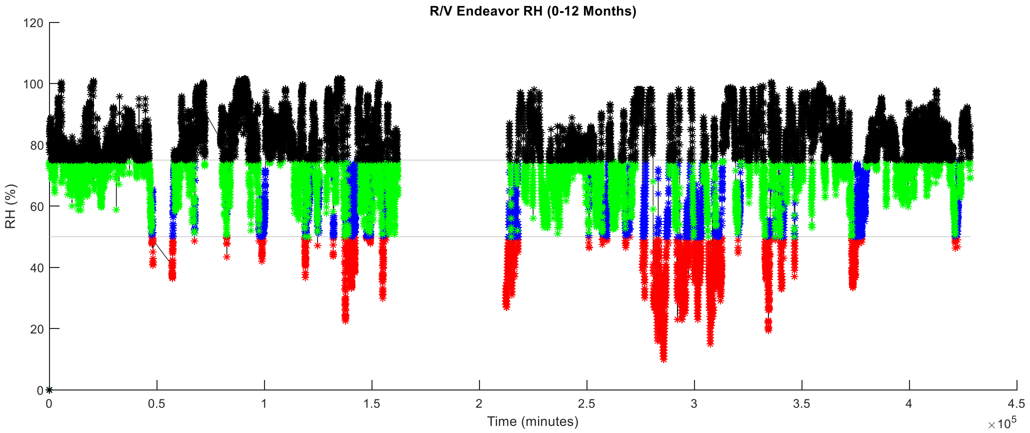

Figure 3.10: RH (%) plot vs time (min) showing humidity fluctuations based on set standards of 50% being low humidity, and 76% being high humidity

The percentage of these humidity occurrences were collected and plotted in Figure 3.11, showing high (>76%), low (<50%), and increasing and decreasing humidity's (76% ≤ 50%). The *R/V Kilo Moana*, for the first 6-months was only at sea for about 2 weeks, with the rest of the time being ported in Honolulu, HI. When comparing the data that was collected for the first 6 months, it can be noted that the *R/V Kilo Moana* sat at both low and high humidity's for a longer duration than the *R/V Endeavor*. Over the 12-month exposures, the *R/V Endeavor* sat at high humidity 45% of the exposure, while the *R/V Kilo Moana* was in this type of exposure only about 20% of the time.

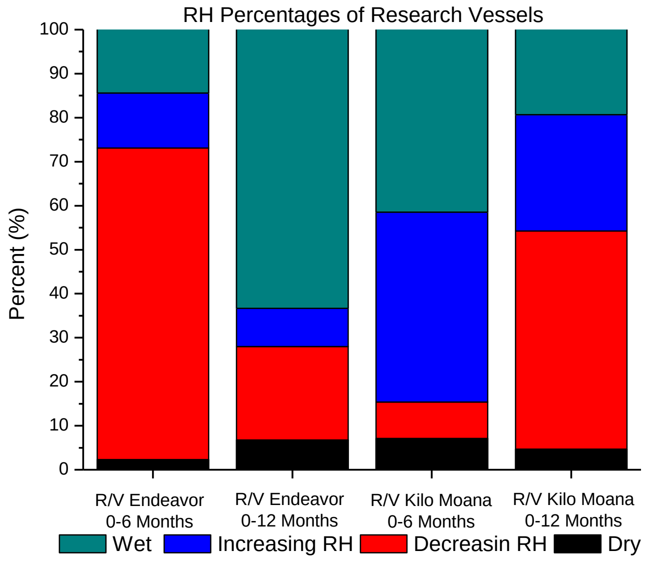

Figure 3.11: Percentage of RH values for each sample removal where high (>76%), low (<50%), and increasing and decreasing humidity's (76% ≤ 50%)

3.6.2 DoS Change over Exposures

DoS measurements on samples returned from each vessel are shown in Figure 3.12. Initial DoS measurements pre-exposure are 6 and 2 mg/cm^2 for AA5456-H116 and AA5083-H116 respectively. Sensitization for AA5456-H116 went up at most 3 mg/cm^2 to a DoS of 9 mg/cm^2. Considering the error in the standard (+/- 5 mg/cm^2), these small changes show that the DoS change over one-year exposure are negligible. Therefore, the original sensitizations used in the matrix, as described in Figure 3.2, have not changed substantially enough to take into consider.

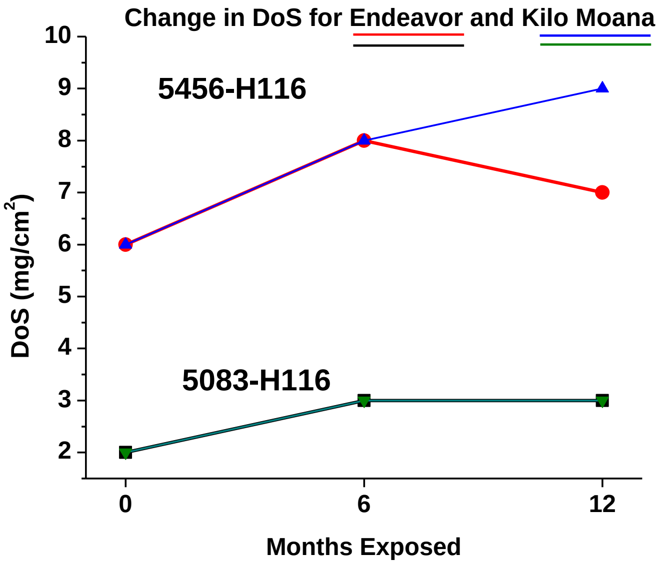

Figure 3.12: Degree of sensitization (mg/cm^2) change over duration of exposure for AA5083-H116 and AA5456-H116 samples returned from the R/V Endeavor and the R/V Kilo Moana

3.6.3 Ag Reductions

Silver was used as a standard to determine corrosion behavior of exposure locations, in support of humidity data. Ag reductions, as in past studies, have variations in reductions over the sample surface as seen below in Figure 3.13. The horizontal lines show reduction potentials of various corrosion products that can be found on Ag. The locations of the AgCl and Ag_2S reduction potentials correlate well with the reduction plateaus obsered. Therefore, it is assumed the reducing products are AgCl and Ag_2S.

The charge and thickness of each trial performed on each sample are shown in Figure 3.14 a&b. The calculated charges and thicknesses show that with increased time, from 6 months exposure to 12 months, the amount of AgCl and Ag_2S deposited increases. It should also be noted that the *R/V Endeavor*, over both 6 and 12-month exposures has more Ag corrosion products deposited. This result implies that the *R/V Endeavor* ported out of Narragansett, RI was in a more corrosive environment than the *R/V Kilo Moana* ported out of Honolulu, HI. Due to Ag being a measure of atmospheric chlorides, this trends along with the fact that the *R/V Endeavor* was at sea for a longer duration than the *R/V Kilo Moana* which remained in port for majority of the exposure time.

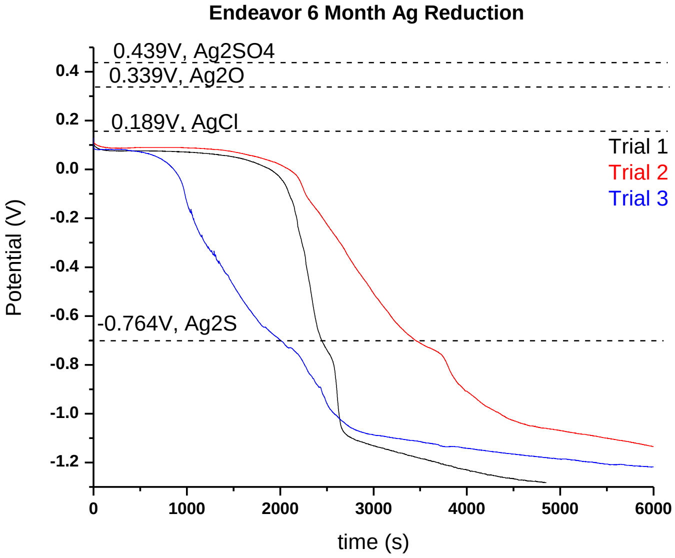

Figure 3.13: Three reduction plots of Ag returned from the R/V Endeavor after 6 months, showing reduction potentials for varying corrosion products

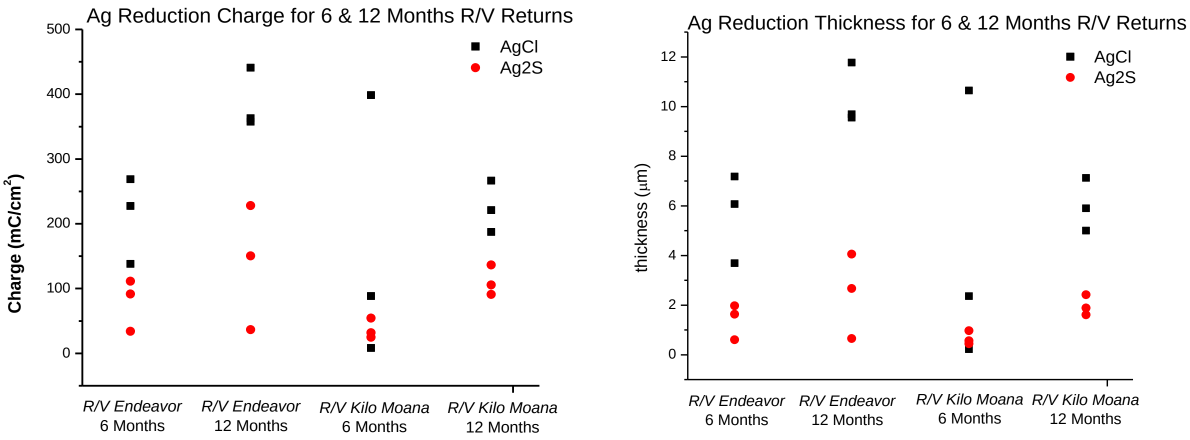

Figure 3.14: a. Ag reduction Q (mC/cm2) for R/V Endeavor and R/V Kilo Moana 6 and 12 month returns b. Thickness (µm) of AgCl and Ag_2S deposited on Ag returned samples from 6 & 12 months returns of the R/V Endeavor and R/V Kilo Moana

3.6.4 CDA 706 Reductions

CDA 706 reductions, performed on AA5083-H116 DoS 10 mg/cm^2 and AA5456-H116 DoS 14 mg/cm^2 for 6 months returns from both research vessels. The plots of reduction potential (V_{SCE}) over time, shown in Figure 3.15, show reduction occurs below the Cu_2O and CuO reduction potentials. Therefore, the reducing product can be any combination of these Cu corrosion products. These results were quantified to Q (mC/cm^2) and plotted in Figure 3.16, from which it is evident that for each exposure site, the AA5456-H116 CDA 706 insert has more corrosion products than the AA5083-H116 CDA 706 insert. AA5456-H116, with its added Mg content, is less corrosion resistant than AA5083-H116. Because of this, the AA5456-H116 is more active. It would be expected that, if CDA corrodes, the more noble AA5083-H116 couple would allow CDA 706 to oxidize more readily. CDA 706, however corrodes due to diurnal wetting and drying following salt spray and exposure. Wetting and drying will not be fully consistent across all samples. There is also bound to be some error in reduction, as evident from

Ag plots shown in Figure 3.13. The *R/V Endeavor* has more corrosion products than the *R/V Kilo Moana*, consistent with the measured corrosivity from Ag reductions from Figure 3.13 for both exposure environments.

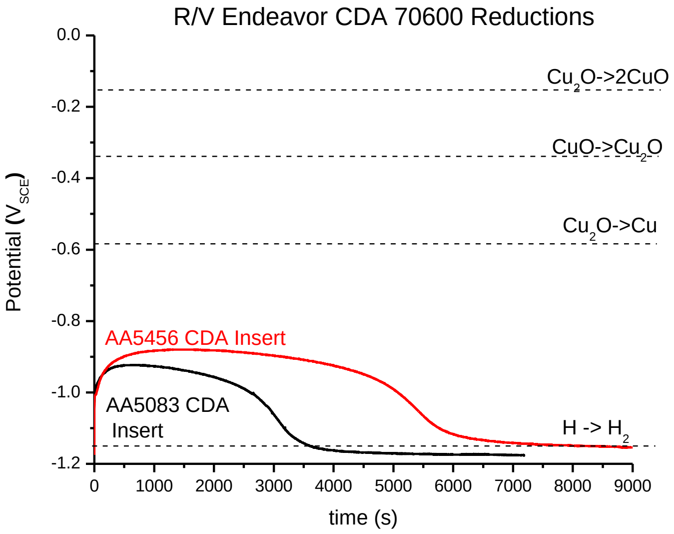

Figure 3.15: Reduction plots for R/V Endeavor 6 month returns of AA5083-H116 and AA5456-H116 DoS 10 & 14 mg/cm2 CDA 706 3/8" inserts respectively

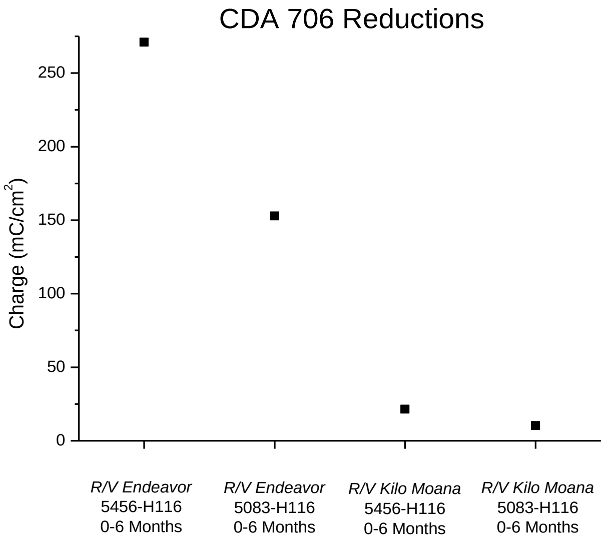

Figure 3.16: Charge values of CDA 706 insert reductions for the R/V Endeavor and R/V Kilo Moana 6 month returns from both AA5083-H116 and AA5456-H116

12-month returns were not able to be reduced using coulometric methods. As shown in Figure 3.17, 12-month exposure reductions resulted in straight H_2O reduction even though there were visible corrosion products on the CDA 706 inserts. Horton et al. found that copper exposures have calcium carbonate ($CaCO_3$) products deposited on the surface in natural marine environments that protect and prevent coulometric reduction testing[46]. Due to corrosion products prevented reduction, these deposits were investigated via Raman, XRD, and XPS. These results are in Appendix A, section 3.11.2-3.11.4. There was a variety of corrosion products detected on the CDA inserts after 12-months with all three analysis tools, however the results are not fully consistent with each other. Although $CaCO_3$ was not consistently seen across all analysis tools, it was evident, some was present on Raman and XPS spectra.

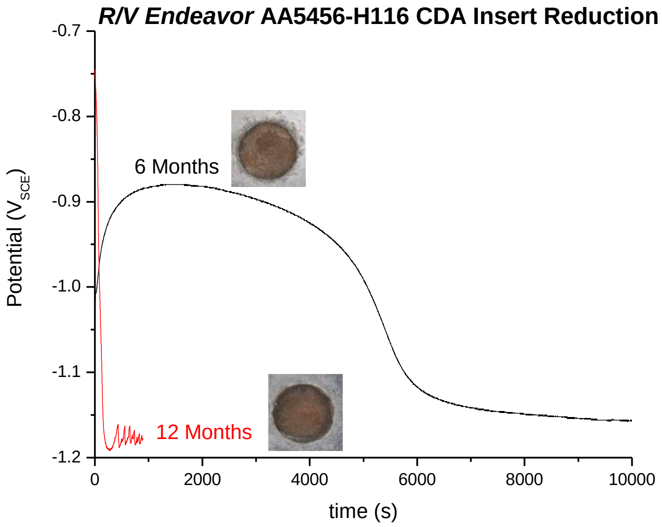

Figure 3.17: Reduction plots for R/V Endeavor 6 & 12 month returns of AA54563-H116 DoS 14 mg/cm2 CDA 706 3/8"

3.6.5 Surface Damage of AA5XXX and CDA 706

Surface damage on AA5XXX samples at varying sensitizations, shown in Figure 3.18 a-c for both exposure sites and durations show minor trends. For DoS of 54 and 23 mg/cm^2, with the exclusion of AA5083 ¼" CDA 706 R/V Endeavor 6-month return, the 3/8" CDA 706 inserts have more throwing power than the ¼" inserts. The lowest DoS used, in Figure 3.18c, shows for the 12 month returns, the larger cathode has the same increased throwing power trend across both AA5XXX alloys. For DoS 54 mg/cm^2, the throwing power is higher for AA5083-H116 than AA5456-H116, independent of cathode size. With increased DoS, there is slightly more visible surface throwing power across the AA5XXX interface from the CDA 706 insert. This damage was again measured following Figure 3.6a methodology.

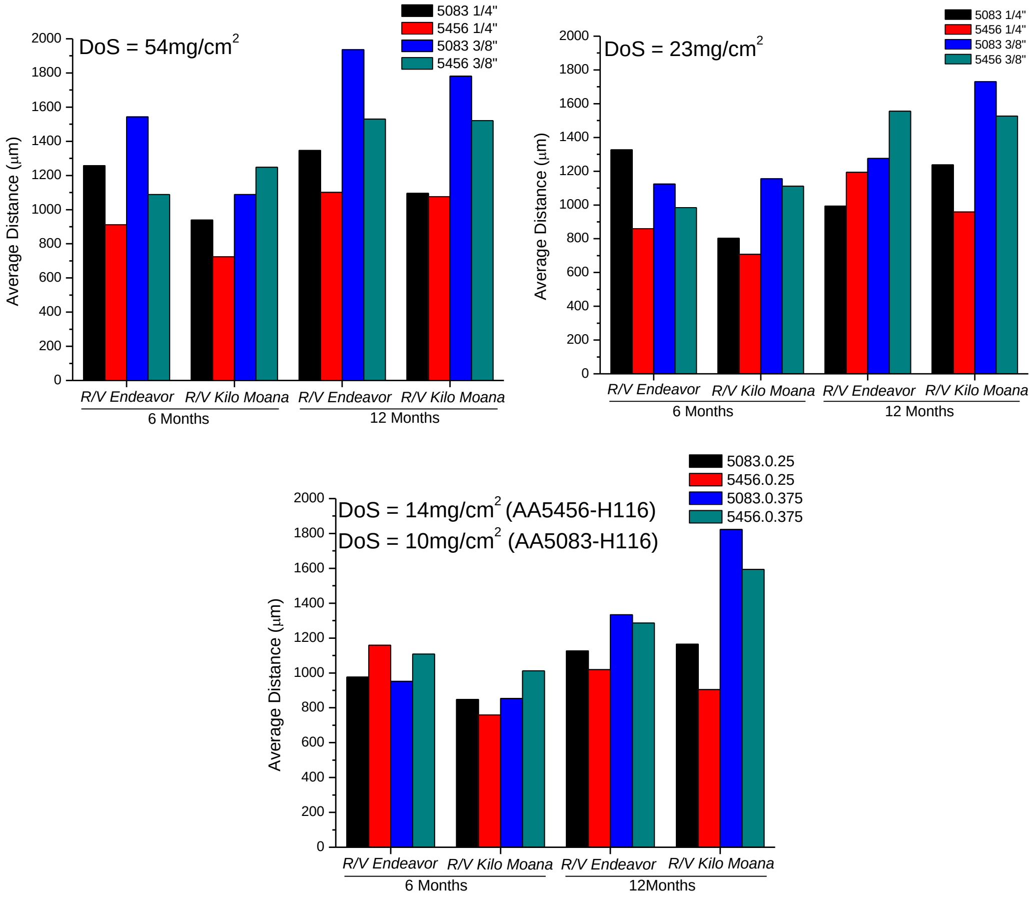

Figure 3.18: Visible Surface Damage on AA5456-H116 and AA5083-H116. Average damage distance (μm) averaged from galvanic interface across AA5XXX sample for each research vessel for 6 and 12-month exposures for a. DoS 54 mg/cm^2 b. DoS 23 mg/cm^2 c. DoS 10 & 14 mg/cm^2

The CDA 706 uncorroded distance along the galvanic couple, shown in Figure 3.19, shows minimal to no dependence on their DoS of AA5XXX. The 3/8” CDA 706 inserts have slightly more uncorroded area than the ¼” CDA 706 insets. The AA5083-H116 CDA 706 inserts have slightly more uncorroded CDA 706 than the AA5456-H116.

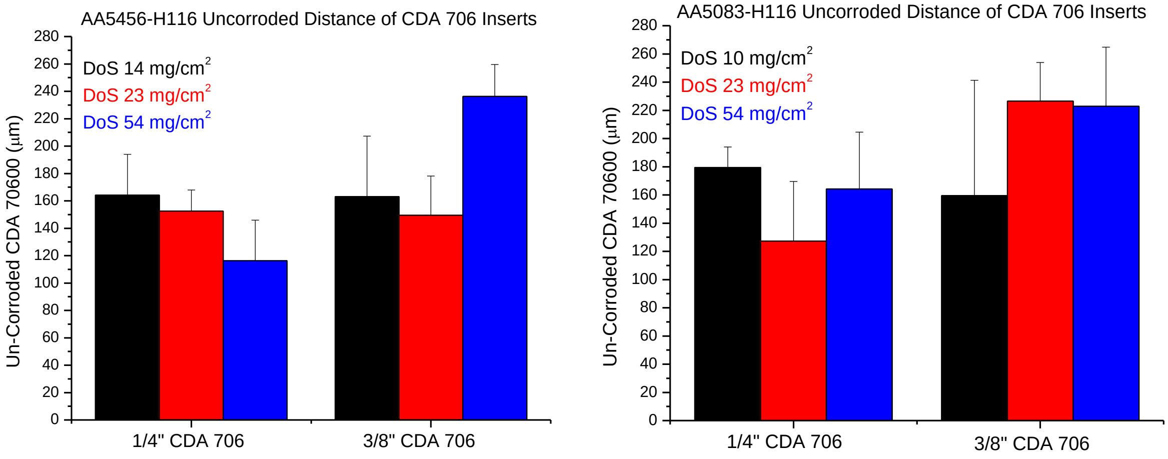

Figure 3.19: Un-corroded CDA 706 distance (µm) from coupling interface for R/V Kilo Moana 12 month returns AA5083-H116 and AA5456-H116 ¼" and 3/8" CDA 706 inserts.

3.6.6 Area Corrosion Damage for Exposures

Area of IGC damage, for DoS 10/14, 23, and 54 mg/cm^2 are shown in Figure 3.20a-c. It should be noted that the R/V Kilo Moana AA5083-H116 3/8" CDA insert sample was misplaced and therefore has no data to report. For all three levels of sensitization, at 6-month durations the area of corrosion was comparable. The 12-month returns have comparable area IGC damage at DoS 10/14 and 23 mg/cm^2. However, at DoS 54 mg/cm^2, the damage is substantially greater on samples from both the *R/V Endeavor* and *R/V Kilo Moana*.

Area damage over 12 months is more extensive on the R/V Kilo Moana DoS 54 mg/cm^2 samples than the R/V Endeavor, with the exception of AA5083-H116 with a 3/8" CDA insert. There is not an easily definable difference between the damage on the two AA5XXX alloys. Seven out of the twelve returns show increased damage with a larger CDA 706 insert with great variation across DoS, research vessel, and duration of exposure.

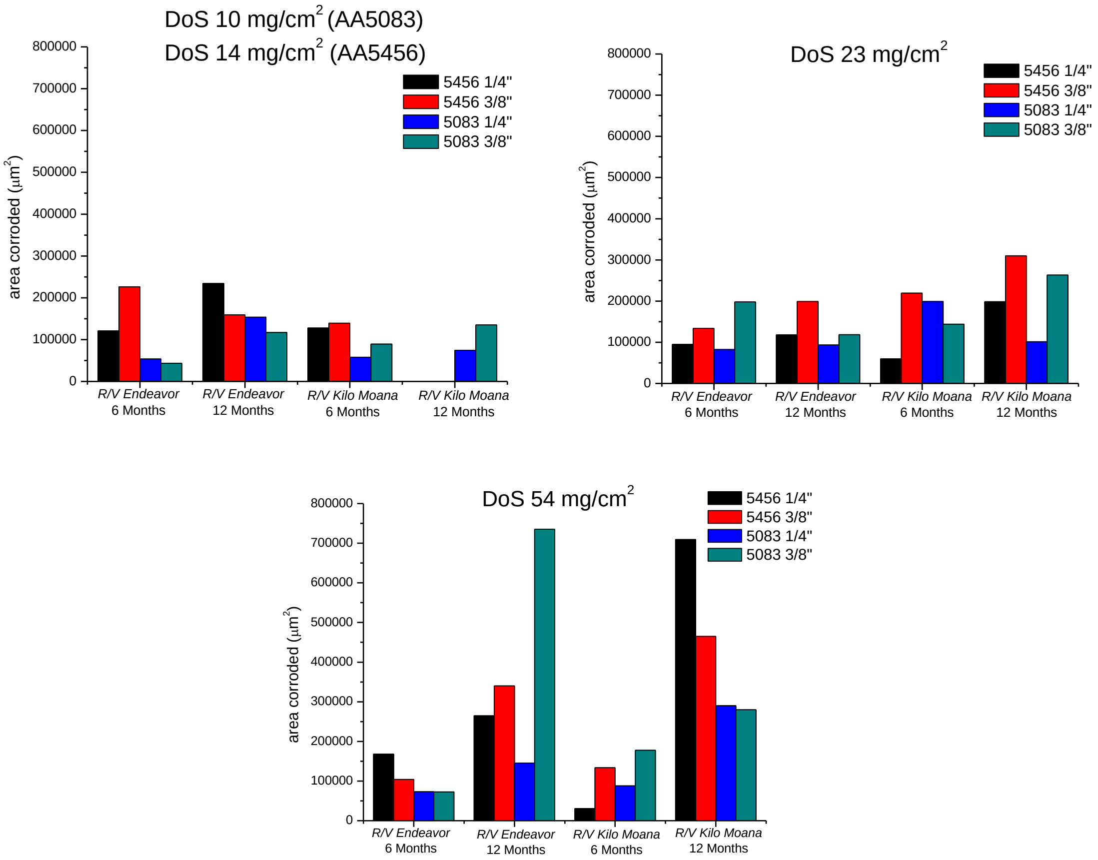

Figure 3.20: Area of corrosion damage on AA5XXX samples with ¼" and 3/8" CDA inserts for R/V Endeavor and R/V Kilo Moana 6 & 12 month returns for a. DoS 10 & 14 mg/cm^2 b. DoS 23 mg/cm^2 c. DoS 54 mg/cm^2

3.6.7 Throwing Power for Exposures

Results showing throwing power and IGC depth damage are shown in below sub-sections with additional plots being shown in the Appendix A sections 3.11.5.1-3.11.5.5.

3.6.7.1 Location Comparisons

Select location comparisons for maximum IGC depth as a function of distance from the AA5XXX and CDA 706 interface are shown in Figures 3.21 and 3.22. AA5083-H116 & AA5456-H116 DoS 54 mg/cm^2 12-month returns are shown in Figure 3.21 a & b respectively.

Maximum IGC for the R/V Endeavor is higher in AA5083-H116 and higher in AA5456-H116 with the exception of one point about 1500 µm away from the CDA 706 interface. Throwing power is greater for the *R/V Endeavor*, both visually from surface damage as depicted by vertical dashed lines, as well as by number of fissures depicted in the scatter plot. There are a good number of fissures past the visible surface damage as well as damage above the baseline IGC on the samples, depicted by the horizontal dashed lines.

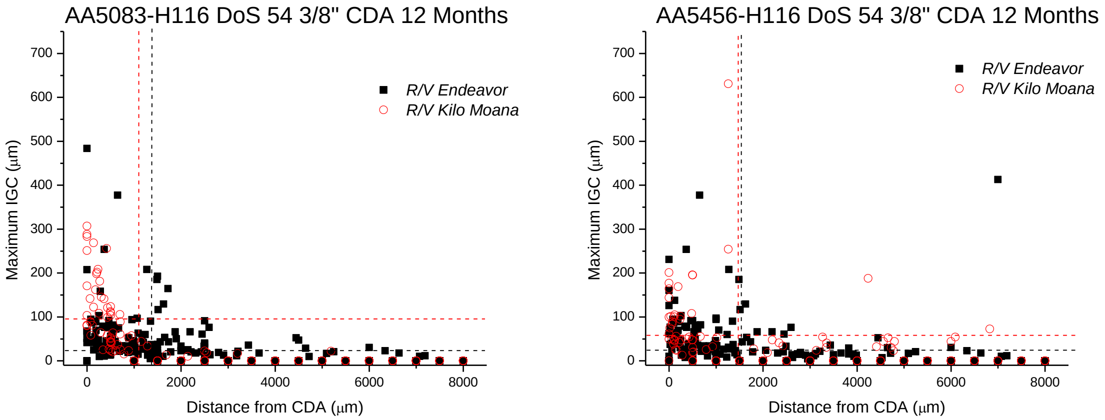

Figure 3.21: a. AA5083-H116 DoS 54 mg/cm^2 with a 3/8" CDA insert showing maximum IGC vs throwing distance from the coupling interface for R/V Endeavor and R/V Kilo Moana 12-month exposure b. AA5456-H116 DoS 54 mg/cm^2 with a 3/8" CDA insert showing maximum IGC vs throwing distance from the coupling interface for R/V Endeavor and R/V Kilo Moana 12-month exposure

AA5083-H116 & AA5456-H116 DoS 14 mg/cm^2 12-month returns are shown in Figure 3.22 a & b respectively. Maximum IGC is highest on the AA5083 exposure for the *R/V Endeavor*, while for AA5456 it is highest on the *R/V Kilo Moana*. There are more fissures on the *R/V Kilo Moana* returns close to the interface, however they have comparable throwing power. It is noted however, that the majority of fissures past the macroscopically observed damage are below the IGC baseline as compared to the samples with a 3/8" CDA insert.

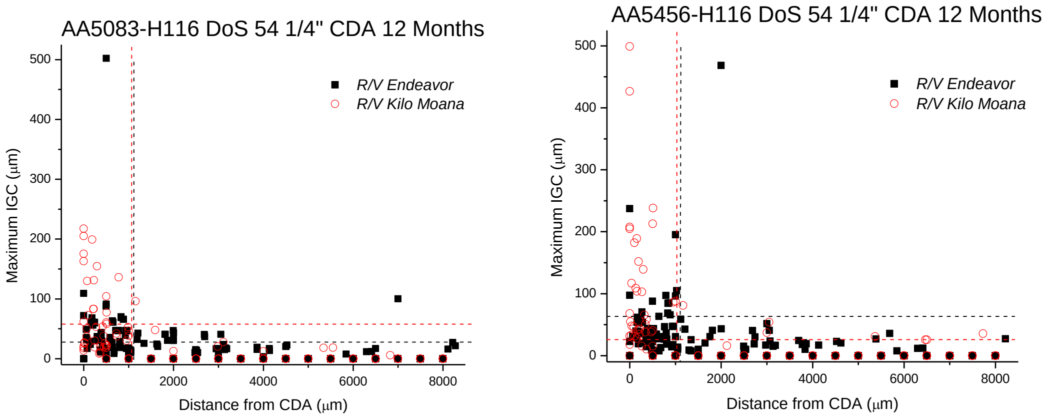

Figure 3.22: a. AA5083-H116 DoS 54 mg/cm^2 with a 1/4" CDA insert showing maximum IGC vs throwing distance from the coupling interface for R/V Endeavor and R/V Kilo Moana 12-month exposure b. AA5456-H116 DoS 54 mg/cm^2 with a 1/4" CDA insert showing maximum IGC vs throwing distance from the coupling interface for R/V Endeavor and R/V Kilo Moana 12-month exposure

3.6.7.2 Duration Comparisons

Select location comparisons for maximum IGC depth as a function of distance from the AA5XXX and CDA 706 interface are shown in Figures 3.23 and 3.24. AA5083-H116 & AA5456-H116 DoS 54 mg/cm^2 with a 3/8" CDA insert exposure returns are shown in Figure 3.23 a & b respectively. The maximum IGC depth is highest for the 12-month return on the AA5083-H116 exposure, and highest on the 6-month exposure for AA5456-H116. Fissures on the AA5083-H116 12-month return are consistently deeper than the 6 month returns, which mainly damaged to depths around 500 μm. The majority of damage sits within the macroscopically observed surface damage, with the exceptions generally occurring below the baseline IGC measurement.

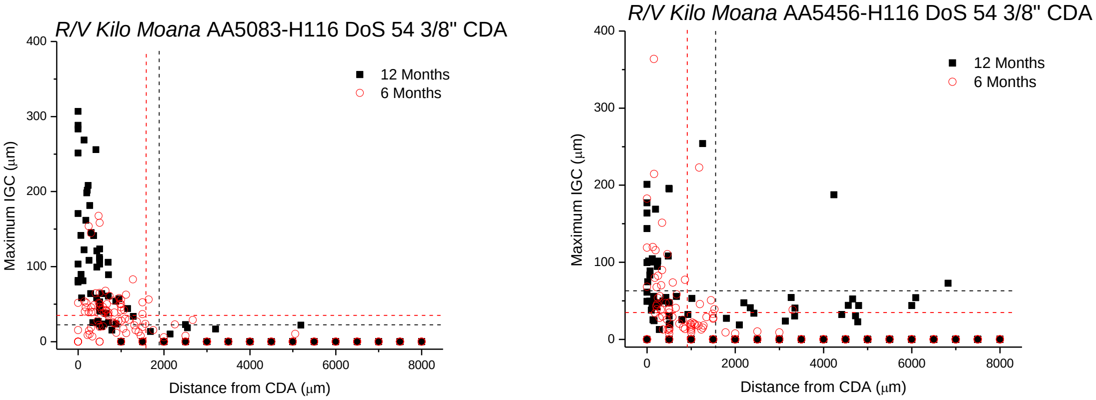

Figure 3.23: a. AA5083-H116 DoS 54 mg/cm^2 with a 3/8" CDA insert showing maximum IGC vs throwing distance from the coupling interface for the R/V Kilo Moana 6 & 12-month exposure b. AA5456-H116 DoS 54 mg/cm^2 with a 3/8" CDA insert showing maximum IGC vs throwing distance from the coupling interface for the R/V Kilo Moana 6 & 12-month exposure

AA5083-H116 & AA5456-H116 DoS 54 mg/cm^2 with a 1/4" CDA insert exposure returns are shown in Figure 3.24 a & b respectively. The maximum IGC depth is highest for the 12-month return on the AA5083-H116 exposure, and highest on the 6-month exposure for AA5456-H116. Fissures on the AA5083-H116 12-month return are consistently deeper than the 6 month returns, which mainly sit around 500 μm. The majority of damage sits within the macroscopically observed damage, with the exceptions for the most part being below the baseline IGC measurement. IGC depth, when comparing a & b, is comparable between both alloys AA5083-H116 and AA5456-H116.

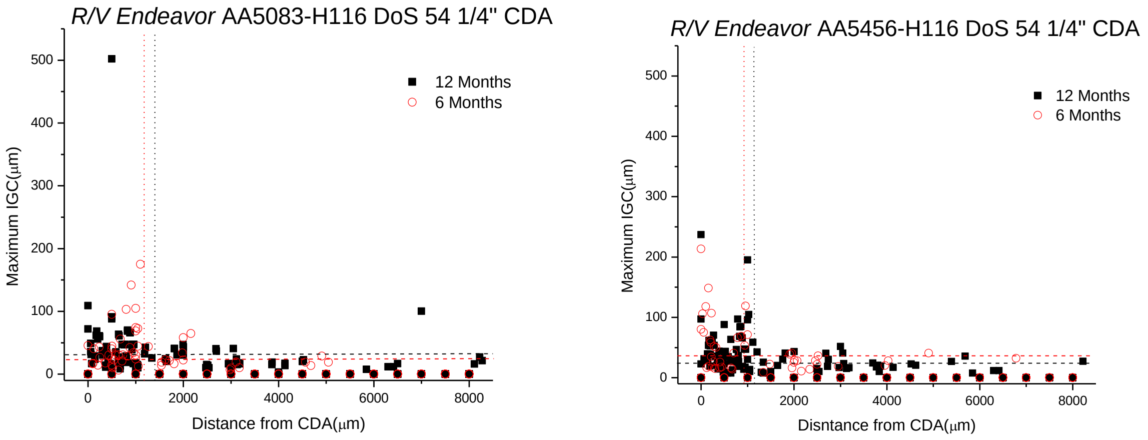

Figure 3.24: a. AA5083-H116 DoS 54 mg/cm^2 with a 1/4" CDA insert showing maximum IGC vs throwing distance from the coupling interface for the R/V Endeavor 6 & 12-month exposure b. AA5456-H116 DoS 54 mg/cm^2 with a 1/4" CDA insert showing maximum IGC vs throwing distance from the coupling interface for the R/V Endeavor 6 & 12-month exposure

3.6.7.3 DoS Comparisons

Select DoS comparisons for maximum IGC depth as a function of distance from the AA5XXX and CDA 706 interface are shown in Figures 3.25 and 3.26. AA5083-H116 & AA5456-H116 with a 3/8" CDA insert exposure returns for R/V Endeavor 12-month returns comparing high and low DoS are shown in Figure 3.25 a & b respectively. The maximum IGC depth on AA5083-H116 return is on the DoS 54 mg/cm^2 which sits out at 3000 µm away from the interface, and outside the visible surface damage range. On both AA5083-H116 and AA5456-H116, the majority of damage sits below 300 µm. There is more throwing power, visible with the DoS 54 mg/cm^2 samples, both within and outside the visible surface damage.

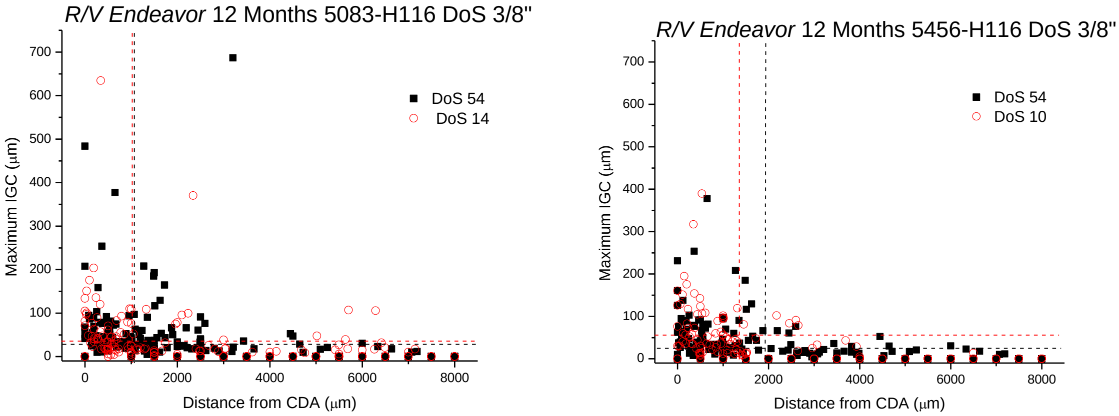

Figure 3.25: a. AA5083-H116 with a 3/8" CDA for the R/V Endeavor 12-month exposure insert showing maximum IGC vs throwing distance from the coupling interface for DoS 14 and DoS 54 mg/cm^2 b. AA5456-H116 with a 3/8" CDA for the R/V Endeavor 12-month exposure insert showing maximum IGC vs throwing distance from the coupling interface for DoS 14 and DoS 54 mg/cm^2

R/V Kilo Moana 12-month AA5456-H116 exposure returns comparing high and low DoS are shown in Figure 3.26 a (1/4" CDA insert) & b (3/8" CDA insert) respectively. The maximum IGC is greater for DoS 54 on the ¼" CDA insert, but not on the 3/8" CDA returned sample. There are less IGC measurements on the R/V Kilo Moana in Figure 3.26a than that observed in Figure 3.26b for the R/V Endeavor with all other parameters being the same.

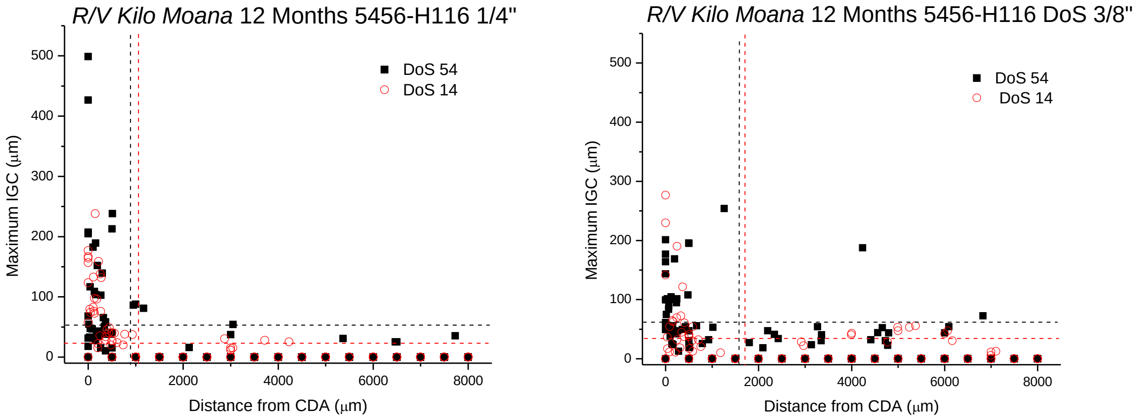

Figure 3.26: a. AA5083-H116 with a 1/4" CDA for the R/V Kilo Moana 12-month exposure insert showing maximum IGC vs throwing distance from the coupling interface for DoS 14 and DoS 54 mg/cm^2 b. AA5456-H116 with a 31/4" CDA for the R/V Kilo Moana 12-month exposure insert showing maximum IGC vs throwing distance from the coupling interface for DoS 14 and DoS 54 mg/cm^2

3.6.7.4 CDA 706 Insert Size Comparisons

Select CDA insert size comparisons for maximum IGC depth as a function of distance from the AA5XXX and CDA 706 interface are shown in Figures 3.27 and 3.28. AA5083-H116 & AA5456-H116 DoS 54 mg/cm^2 for *R/V Endeavor* 12-month returns comparing CDA inserts of ¼" and 3/8" are shown in Figure 3.27 a & b respectively. The visible surface damage throwing power for the 3/8" CDA insert is greater than that of the ¼" insert on both alloys. The maximum IGC depth is 3/8" for AA5083-H116 and is ¼" for AA5456-H116. However, there is more prominence of 3/8" fissures with the 3/8" CDA insert than that of the ¼" CDA. About 1000 µm past the visible surface damage there is IGC above the baseline damage for both alloy cases.

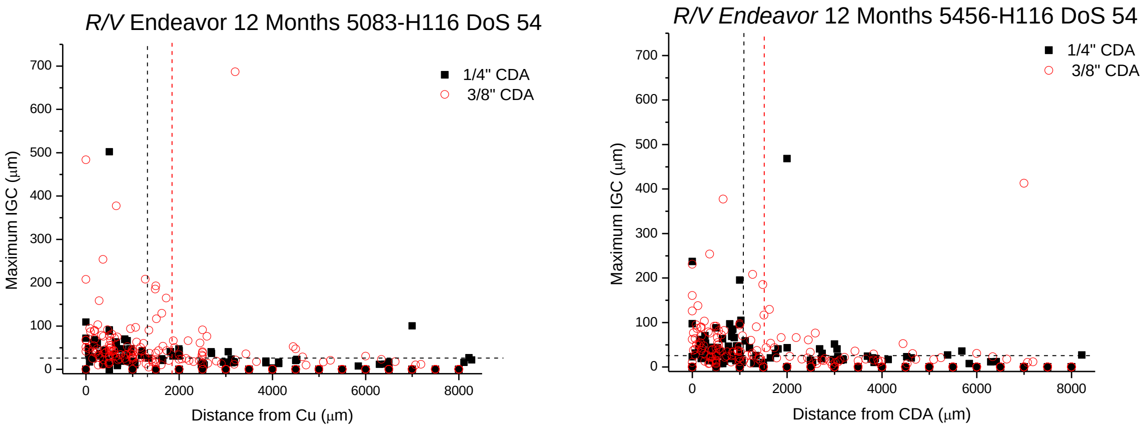

Figure 3.27: a. AA5083-H116 DoS 54 mg/cm^2 for the R/V Endeavor 12-month exposure showing maximum IGC vs throwing distance from the coupling interface for ¼" and 3/8" CDA inserts b. AA5456-H116 DoS 54 mg/cm^2 for the R/V Endeavor 12-month exposure showing maximum IGC vs throwing distance from the coupling interface for ¼" and 3/8" CDA inserts

AA5083-H116 & AA5456-H116 DoS 54 mg/cm^2 for *R/V Kilo Moana* 12-month returns comparing CDA inserts of ¼" and 3/8" are shown in Figure 3.28 a & b respectively. The maximum IGC, for both alloys is comparable for both insert sizes. The 3/8" insert results in greater throwing power, particularly evident by Figure 25b with IGC depths in the 50 µm range out to 7500 µm. These fissures, however, fall at or below the baseline depth. *R/V Endeavor* plots, from Figures 3.28 a & b, have more fissures than that of the *R/V Kilo Moana* in Figures 3.28 a & b.

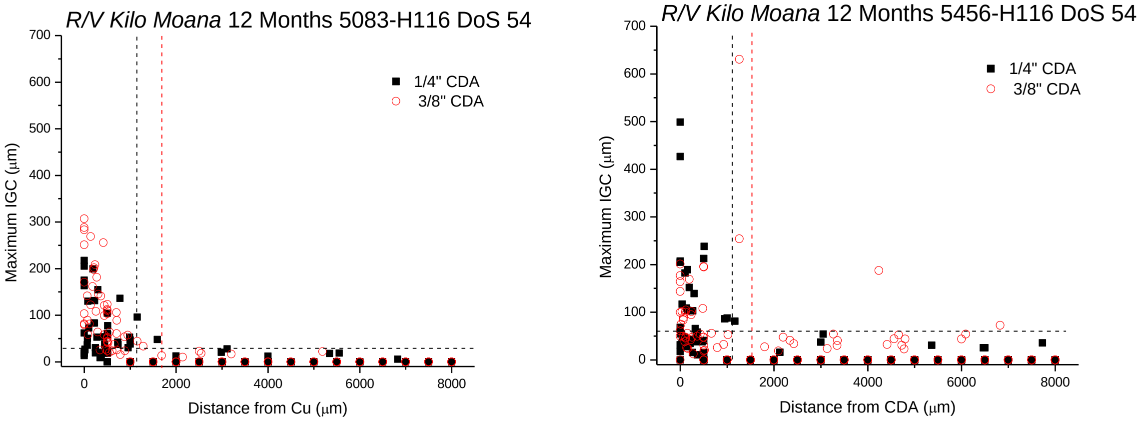

Figure 3.28: a. AA5083-H116 DoS 54 mg/cm^2 for the R/V Kilo Moana 12-month exposure showing maximum IGC vs throwing distance from the coupling interface for ¼" and 3/8" CDA inserts b. AA5456-H116 DoS 54 mg/cm^2 for the R/V Kilo Moana 12-month exposure showing maximum IGC vs throwing distance from the coupling interface for ¼" and 3/8" CDA inserts

3.6.7.5 Alloy Comparisons

Select alloy comparisons for maximum IGC depth as a function of distance from the AA5XXX and CDA 706 interface are shown in Figures 3.29 and 3.30. *R/V Endeavor* DoS 54 mg/cm^2 12-month returns comparing AA5083-H116 and AA5456-H116 for 3/8" and ¼" CDA inserts are shown in Figure 3.29 a & b respectively. The maximum IGC depth for both 3/8" and ¼" CDA inserts are AA5083-H116. From Tables 3.1 & 3.2, it is known that AA5456-H116 has slightly more magnesium and is less corrosion resistant that AA5083-H116. IGC trends are very comparable, with slightly more fissures on the AA5456-H116 than AA5083-H116 alloy.

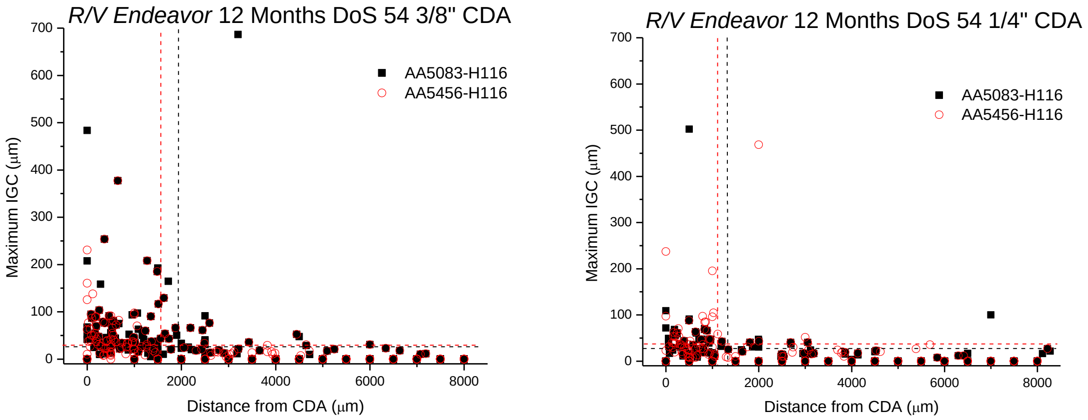

Figure 3.29: a. R/V Endeavor 12-month exposure for DoS 54 mg/cm^2 with a 3/8" CDA insert showing maximum IGC vs throwing distance from the coupling interface for AA5083 and AA5456 b. R/V Endeavor 12-month exposure for DoS 54 mg/cm^2 with a 1/4" CDA insert showing maximum IGC vs throwing distance from the coupling interface for AA5083 and AA5456

The *R/V Endeavor* DoS 10 & 14 mg/cm^2 12-month returns comparing AA5083-H116 and AA5456-H116 for 3/8" and ¼" CDA inserts are shown in Figure 3.30 a & b respectively. The maximum IGC for the 3/8" CDA insert is highest for AA5083-H116 alloy sample, but for the ¼" CDA, AA5456-H116 has the deepest fissure. Both alloys, however have very comparable throwing power amongst both CDA insert sizes.

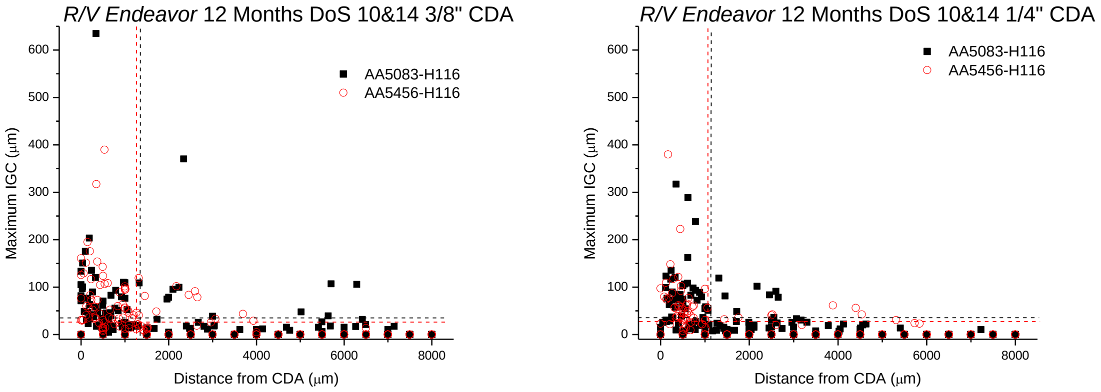

Figure 3.30: a. R/V Endeavor 12-month exposure for DoS 10&14 mg/cm^2 with a 3/8" CDA insert showing maximum IGC vs throwing distance from the coupling interface for AA5083 and AA5456 b. R/V Endeavor 12-month exposure for DoS 10&14 mg/cm^2 with a 1/4" CDA insert showing maximum IGC vs throwing distance from the coupling interface for AA5083 and AA5456

The *R/V Kilo Moana* DoS 54 mg/cm^2 12-month returns comparing AA5083-H116 and AA5456-H116 for 3/8" and ¼" CDA inserts are shown in Figure 3.31 a & b respectively. Figure 3.31 a show that for the 3/8" CDA insert sample, AA5083-H116 has a higher maximum IGC depth than AA5456-H116. For the ¼" CDA insert shown in Figure 3.31b, AA5456-H116 has a higher maximum IGC. The throwing power trends of both alloys, are however comparable, with the 3/8" CDA insert being greater than the ¼" CDA insert.

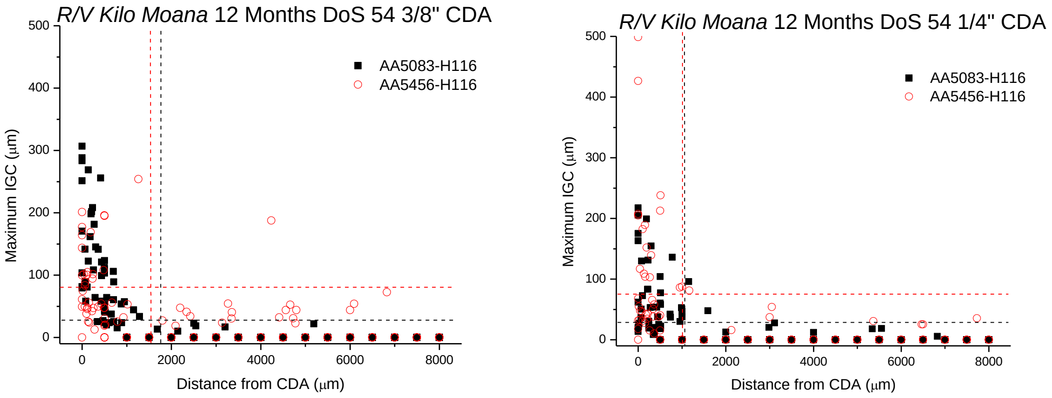

Figure 3.31: a. R/V Kilo Moana 12-month exposure for DoS 54 mg/cm^2 with a 3/8" CDA insert showing maximum IGC vs throwing distance from the coupling interface for AA5083 and AA5456 b. R/V Kilo Moana 12-month exposure for DoS 54 mg/cm^2 with a 1/4" CDA insert showing maximum IGC vs throwing distance from the coupling interface for AA5083 and AA5456

3.7 Discussion

3.7.2 Weather Influence on Corrosion

Ag reduction charges, from Figure 3.15 shows greater charge on *R/V Endeavor* returns than *R/V Kilo Moana*. The same trend stands for CDA 706 reductions, shown in Figure 3.17. The *R/V Kilo Moana*, particularly for the first 6 months, remained in port for the majority of exposure as evident from maps in Figure 3.4. *R/V Endeavor*, when at sea, spent little time at low humidity's. Over the first six months, samples from the *R/V Endeavor* spent a majority of time wetting/drying as seen in Figure 3.12 RH values compared to those of the *R/V Kilo Moana*. It would be expected that at higher humidity's, corrosion would increase. However, the *R/V Kilo Moana* for the first 6 months remained in port for all but 2 weeks. When in port, samples are protected from salt spray that would be experienced if the research vessel remained at sea due to splash and wind. From 0 to 12 months, the *R/V Endeavor*, again was at sea for a longer duration, but samples remained at high RH values, and remained wet compared to the *R/V Kilo Moana* which sat mostly at mid RH values.

Visible surface damage, shown in Figure 3.19, shows the general trend, particularly at higher DoS values, that the *R/V Endeavor* has larger damage from the CDA 706 interface across the AA5XXX surfaces. Over the first 6-months of exposure, since the *R/V Endeavor* is at sea for a much longer duration than the *R/V Kilo Moana*, it undergoes a much more aggressive salt spray. Over a full year, the *R/V Endeavor* was at a high humidity longer than the *R/V Kilo Moana*. This high humidity also keeps the sample wet to accelerate cathodic current across the surface of the samples. Area damage, however, shown in Figure 3.17 is comparable for both locations. From Figure 3.18 and 3.19, it can be seen that the *R/V Kilo Moana* has more IGC close to the galvanic coupling interface, while the *R/V Endeavor* samples have more throwing power. Since the *R/V Kilo Moana* samples remain wet longer, it allows for current from the CDA 706 cathode to be thrown and distributed further across the AA5XXX interface.

3.7.3 AA5083-H116 vs AA5456-H116 Exposures

As shown in Tables 3.1 and 3.2, AA5083-H116 has less Mg content than AA5456-H116. The increased Mg content in AA5456-H116 produces a slightly more active alloy, however likely not significant enough to have an impact. From Figure 3.19, it is evident that the majority of AA5083-H116 coupled samples, with only minor exceptions, have more visible surface damage away from the CDA 706 coupling interface. This same trend occurs for area of corrosion damage, shown in Figure 3.21. There are minor differences in IGC depth and throwing power trends shown in Figure 3.29-3.31. The slight variation in Mg content is not sufficient enough to result in a significant change in IGC propagation over 12-months of exposure. However, over time, due Mg content, alloy variations will likely have an impact as DoS increases more rapidly for AA5456 alloys than AA5083[47].

3.7.4 ¼ CDA 706 insert vs 3/8” CDA 706 insert Exposures

The 3/8” CDA inserts on the *R/V Kilo Moana* and R/V Endeavor 6 & 12-month returns, for the majority of samples, has more visible surface damage than that of the ¼” CDA returns as evident in Figure 3.19. Area of corrosion damage, however is not consistently larger for a larger cathode as seen in Figure 3.21. The larger cathode is expected to and does have more throwing power than the smaller cathode. This difference is not significant due to the thin water layer under atmospheric conditions. Figures 3.27 and 3.28 show IGC depth over the AA5XXX and CDA 706 interface. Samples with a 3/8” CDA insert have higher maximum IGC depth than those with a ¼” insert. The variation in area damage is based on the AA5XXX orientation. The LT face is exposed, resulting in IGC propagation down and horizontally due to grain structure, evident in Figure 3.1. The shorter fissures from the ¼” CDA inserts propagate horizontally across the L direction, while the 3/8” inserts propagate further down the S direction.

3.7.5 DoS Influence on Exposure IGC

With increased DoS, comes increased amounts of the anodic β phase at the grain boundaries. This results in accelerated IGC propagation. After 12 month returns, area damage plots, shown in Figure 3.21 show greater corrosion damage for DoS 54 mg/cm^2 than DoS 23, 14 & 10 mg/cm^2. Figures 3.25 & 3.26 validate the trend that on the surface, there is more throwing power evident on DoS 54 mg/cm^2 samples than DoS 10 & 14 mg/cm^2. In addition, subsurface, the exponential decay trends for DoS 54 mg/cm^2 carries further away from the coupling interface.

Mizuno et al. found that throwing distance on AA5083-H116 coupled to AISI 4340 was higher with a lower DoS, while the highest DoS has a larger maximum IGC depth[28]. While this throwing power phenomena occurs when IGC propagates in the L direction, exposure samples in this work have IGC propagation in the S direction. Because of the shape of grains being elongated parallel with the sample surface, IGC more easily propagates horizontally over the S direction than vertically.

3.8 Conclusions

A multitude of variables effect IGC propagation on AA5XXX when galvanically coupled in outdoor exposure testing. The influence of location, duration of exposure, DoS, CDA insert size, and aAA5XXX alloy were investigated.

(1) Location

Locations of exposures changed due to the research vessels being at sea for much of the exposures. Ag reductions validate that the *R/V Endeavor* was exposed to more corrosive conditions, as an effect of RH and remaining at sea for a majority of exposures while the *R/V Kilo Moana* remained mainly in port. With increased TOW and salt spray from being at sea on the *R/V Endeavor*, the cathodic CDA 706 insert had more throwing power across the AA5XXX interface.

(2) Duration

The time of exposures was shown to influence IGC propagation. Both 6 & 12-month exposures result in damage, however, the additional 6-months exposure resulting in a 12-month exposure accelerated IGC propagation. Specifically, at DoS 54 mg/cm^2, corroded AA5XXX doubles or greater in area from 6 to 12-month exposures.

(3) DoS

Increased DoS resulted in increased throwing power, both visible on and below the surface. Maximum fissure depth also increased with increased DoS. With increased β phase, IGC fissures propagate deeper down the AA5XXX samples and across the AA5XXX surface.

(4) CDA Insert Size

With increased CDA 706 insert diameter, 3/8” vs ¼”, cathodic current across the AA5XXX increases. Maximum IGC depth increases across the surface with increased cathode size. The throwing power across the surface increase with increased CDA insert diameter.

(5) Alloy: AA5083-H116 vs AA5456-H116

Over 12-month exposures, there is little trend in IGC propagation based on alloy composition. AA5083-H116 and AA5456-H116, with a minor difference in Mg composition, does not have a large enough effect on IGC and throwing power trends as the DoS values are comparable amongst alloys.

3.9 Acknowledgments

Financial support from the Office of the Undersecretary of Defense Technical Corrosion Collaboration via the USAFA Contract FA7000-14-2-0010 is gratefully acknowledged. Much thanks to the crew of the *R/V Endeavor*: Lynne Butler, Tina Thomas, and particularly William L. Fanning for their aid exposure, meteorological data collection, and retrievals. Thanks also to the crews of the *R/V Kilo Moana*: Trevor Young, Kim Kreuger, and particularly Alan C. Hilton. Thanks to undergraduate research assistants: Cameron Aadahl, John Brownhill, Harris Dunlap, and James Perry for assistance in outdoor exposure sample analysis.

3.10 References

1. McCafferty, E. *Introduction to Corrosion Science*. (2009).
2. Kelly, R., Scully, J., Shoesmith, D. & Buchheit, R. *Electrochemical Techniques in Corrosion Science and Engineering*. **20021014,** (2002).
3. Mizuno, D. & Kelly, R. G. Galvanically Induced Intergranular Corrosion of AA5083-H131 Under Atmospheric Exposure Conditions - Part I –Experimental Characterization. 1–6 (2013).
4. Golumbfskie, W. private communication.
5. Lim, M. L. C., Kelly, R. G. & Scully, J. R. Overview of intergranular corrosion mechanisms, phenomenological observations, and modeling of AA5083. *Corrosion* **72,** 198–220 (2016).
6. Birbilis, N. *et al.* A Survey of Sensitisation in 5xxx series Aluminium Alloys. *Corrosion* **72,** 144–159 (2016).
7. McMahon, M., Steiner, P., Lass, A. & Burns, J. The Effect of Loading Orientation on the Stress Corrosion Cracking of Al-Mg Alloys. *Corrosion* **73,** 347–361 (2017).
8. https://www.vesseltracker.com/en/Ships/Kilo-Moana-9229037.html.
9. Mary Parker (personal communication). (2018).
10. Greene, H. J. Evaluation of Corrosion Protectin Methods for Aluminum Metal Matrix Composites. (1992).
11. Khullar, P., Badilla, J. V & Kelly, R. G. Intergranular Corroson in Al-Mg 5XXX Alloys Under Atmospheric Exposures. in *NACE* 1–10
12. Montgomery, J. S. & Chin, E. . The AMPTIAC Quarterly. **8,** 15–20 (2004).
13. Searles, J. L., Gouma, P. I. & Buchheit, R. G. Stress corrosion cracking of sensitized AA5083 (Al-4.5Mg-1.0Mn). *Metall. Mater. Trans. A Phys. Metall. Mater. Sci.* **32,** 2859–2867 (2001).
14. Oguocha, I. N. A., Adigun, O. J. & Yannacopoulos, S. Effect of sensitization heat treatment on properties of Al-Mg alloy AA5083-H116. *J. Mater. Sci.* **43,** 4208–4214 (2008).
15. Lerman, D. & Capaccio, T. Navy Finds ‘Aggressive’ Corrosion on Austal’s Combat Ship. *Bloomberg* (2011). Available at: https://www.bloomberg.com/news/articles/2011-06-17/navy-finds-aggressive-corrosion-on-austal-s-combat-ship-1-.
16. CORROSION FAILURE: LCS 2 USS Independence Naval Ship Engine Corrosion. *NACE International* Available at: https://www.nace.org/CORROSION-FAILURE-LCS-2-USS-Independence-Naval-Ship-Engine-Corrosion.aspx.
17. Schleich, W. *Typical failures of CuNi 90/10 seawater tubing systems and how to avoid them*.
18. Davis, J. R. Corrosion of Aluminum and Aluminum Alloys. *Mater. Park. OH ASM Int.* 75–83 (1999).
19. Crane, C. B. & Gangloff, R. P. Stress Corrosion Cracking of Low Temperature Sensitized AA5083. *Corrosion* **72,** 1–14 (2011).
20. Jones, R. H., Baer, D. R., Danielson, M. J. & Vetrano, J. S. Role of Mg in the Stress Corrosion Cracking of an Al-Mg Alloy. *Metall. Mater. Trans. A* **32,** 1699–1711 (2001).
21. McMahon, M. E., Steiner, P. J., Lass, A. B. & Burns, J. T. The Effect of Temper and Composition on the Stress Corrosion Cracking of Al-Mg Alloys. *Corrosion* **73,** 347–361 (2017).

22. Aylor, D. M., Hays, R. A. & Marshall, L. S. *Galvanic Corrosion Evaluation of High Performance Naval Seawater Valve Materials in Quiescent, Natural Seawater*. (2000).
23. Hack, H. P. & Wheatfall, W. W. Evaluation of Galvanic and Stray Current Corrosion in 70/30 Copper-Nickel/Alloy 625 Piping Systems. *CARDIVNSWC-TR-61--94/15* (1995).
24. Hack, H. P. & Wheatfall, W. W. *Comparison of Cathodic Protection Currents on 70/30 Copper-Nickel and Alloy 625 Piping Systems*. *CARDIVNSWC-TR-61--94/14* (1995).
25. Srinivasa Rao, A. *Characterization of the Surface Film Growth During the Electrochemical Process: Part III (70 % Copper- 30 % Nickel System). CARDIVNSWC - TR - 61 - 98 - 24* (1998).
26. Tuthill, A. H. Guidelines For the Use of Copper Alloys In Seawater. *Mater. Perform.* **26,** 12–22 (1987).
27. North, R. F. & Pryor, M. J. The Influence of Corrosion Product Structure on the Corrosion Rate of Cu-Ni Alloys. *Corros. Sci.* **10,** 297–311 (1970).
28. Mizuno, D. & Kelly, R. G. Galvanically Induced Intergranular Corrosion of AA5083-H131 Under Atmospheric Conditions Part 2 Modelling the damage. *Corrosion* **69,** 681–692 (2013).
29. Khullar, P. & Kelly, R. G. *Investigation of Corrosion Testing Methods and Selected Corrosion Protection Strategies on Modern High-Performance Alloys that Affect Land Vehicle Structural Integrity (2012-2016)*. (2016).
30. Mizuno, D. & Kelly, R. G. Galvanically Induced Intergranular Corrosion of AA5083-H131 Under Atmospheric Conditions Part 2 Modelling the damage. *Corrosion* **69,** 681–692 (2013).
31. Holtz, R. L., Pao, P. S., Bayles, R. A., Longazel, T. M. & Goswami, R. Corrosion-fatigue behavior of aluminum alloy 5083-H131 sensitized at 448 K (175 C). *Metall. Mater. Trans. A Phys. Metall. Mater. Sci.* **43,** 2839–2849 (2012).
32. Lim, M. L. C. *et al.* Model to predict intergranular corrosion propagation in three dimensions in AA5083-H131. *Mater. Des.* **96,** 131–142 (2016).
33. Lim, M. L., Scully, J. R. & Kelly, R. G. Intergranular Corrosion Penetration in AA5083 as a Function of Electrochemical and Metallurgical Conditions service. **69,** 35–47 (2013).
34. Schleich, W. Typical failures of CuNi 90/10 seawater tubing systems and how to avoid them. *Eng. Struct.* **49,** (2004).
35. ASTM G67-04, 'Standard Test Method for Determining the Susceptibility to Intergranular Corrosion of 5XXX Series Aluminum Alloys by Mass Loss After Exposure to Nitric Acid (NAMLT Test)'. (2004).
36. M. Tiryakioglu, J. T. S. Physical Metallurgy and the Effect of Alloying Additions in Aluminum Alloys. in *Handbook of Aluminum* (ed. G.E. Totten, D. S. M.) (Marcel Dekker, Inc, 2003).
37. Tattersall, C. Manual for Depth Analysis Code.
38. Tattersall, C. & Kelly, R. G. Automated Quantification of Corrosion Damage from Cross-sectional Micrographs. *to be Submitt. to Corros.*
39. Burns, C. *Understanding the Intergranular Corrosion Kinetics in AA5456-H116 as a Function of Electrochemical and Metallurgical Variables*. (2017).
40. Abbott, W. H. A Decade of Corrosion Monitoring in the World ' s Military Operating Environments -A Summary of Results. *Columbus, OH DoD CorrDefense* (2008).
41. Katona, R. Personal Communication. (2017).
42. Macha, Erica N.;Dante, J. F. Effect of Cyclic RH & Preliminary Sensor Analysis.

Personal Communication. (2018).
43. Neiser, E. B. Atmospheric Corrosion of Silver and its Relation to Accelerated Corrosion Testing. (University of Virginia, 2010).
44. ASTM B825-13: Standard Test Method for Coulometric Reduction of Surface Films on Metallic Test. *Annu. B. ASTM Stand.* (2002). doi:10.1520/B0825-13.2
45. NIH. Image J.
46. Horton, D. J., Sanders, C. E., Anderson, R. M., Davis, R. S. & Lemieux, E. J. Accelerated Field Exposure using Seawater Spray: A Comparison to Traditional Atmospheric Test Methods. *NACE Corros. Conf.* **Paper No.,** 1–11 (2017).
47. Lim, M. L. C. Intergranular Corrosion Propagation in Sensitized Al-Mg Alloys. (University of Virginia, 2016).

3.11 Appendix A

3.11.1 Humidity

Additional RH (%) vs time (min) plots are displayed below in Figures X-X for the *R/V Endeavor* 0-6 months and the *R/V Kilo Moana* 0-6 and 0-12-month exposures. Blank spaces on the *R/V Endeavor* plot represent times that meteorological data was not collected. Blank spaces on *the R/V Kilo Moana* plot represent dates the vessel was in port. These days in port data was not collected.

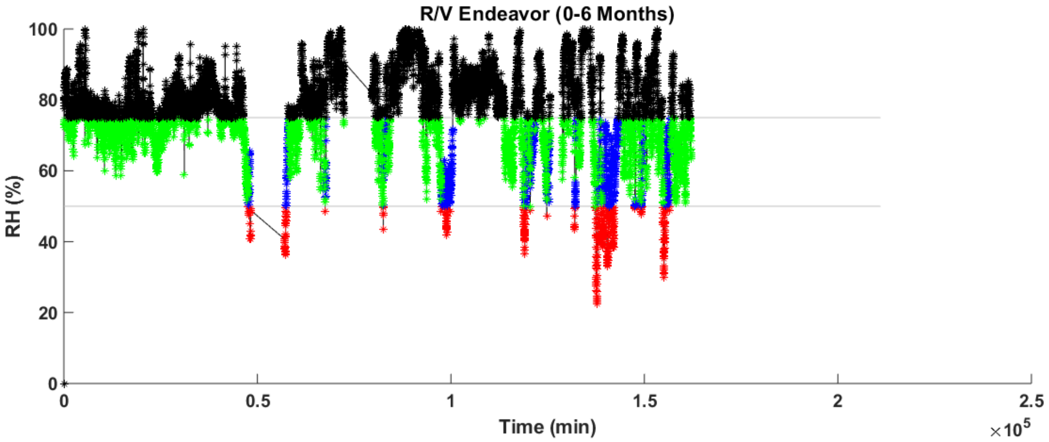

Figure 3.31: MATLAB plot RH (%) plot vs time (min) showing humidity fluctuations based on set standards of 50% being low humidity, and 76% being high humidity for R/V Endeavor (0-6 Months)

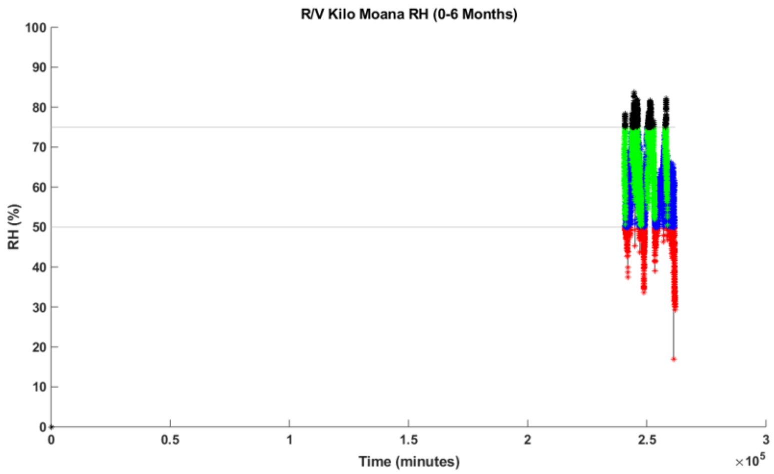

Figure 3.32: MATLAB plot RH (%) plot vs time (min) showing humidity fluctuations based on set standards of 50% being low humidity, and 76% being high humidity for R/V Kilo Moana (0-6 Months)

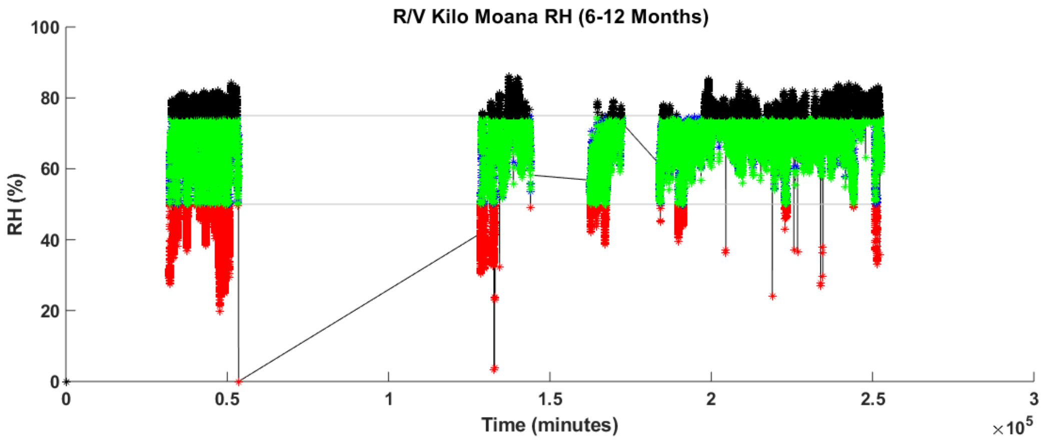

Figure 3.33: MATLAB plot RH (%) plot vs time (min) showing humidity fluctuations based on set standards of 50% being low humidity, and 76% being high humidity for R/V Kilo Moana (0-12 Months)

3.11.2 Raman

Raman was performed on *R/V Endeavor* and *R/V Kilo Moana* 12-month return CDA inserts. A 532 nm laser was utilized at varying powers to retrieve data. For the *R/V Endeavor*, only the AA5083-H116 with a 3/8” CDA insert was scanned in the middle of the CDA insert. For the

R/V Kilo Moana, the center and edge of the CDA 706 inserts were scanned to investigate corrosion products.

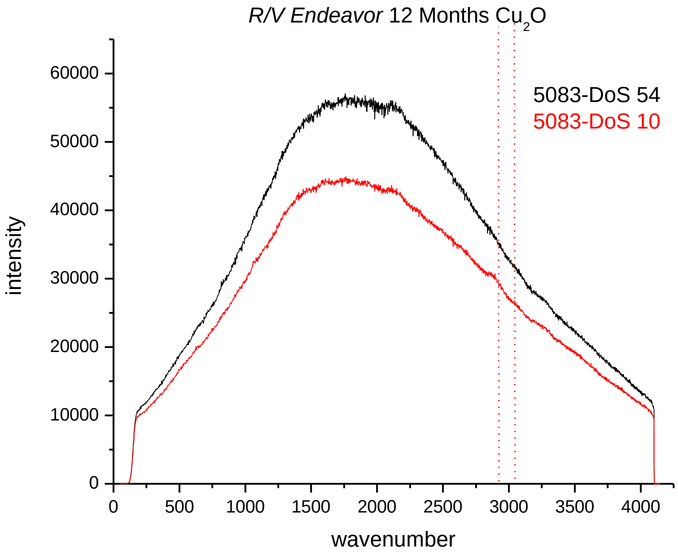

Figure 3.34: R/V Endeavor 12 Month AA5083-H116 DoS 10 & 54 mg/cm^2 sample with 3/8" CDA insert highlighting Cu_2O peak locations

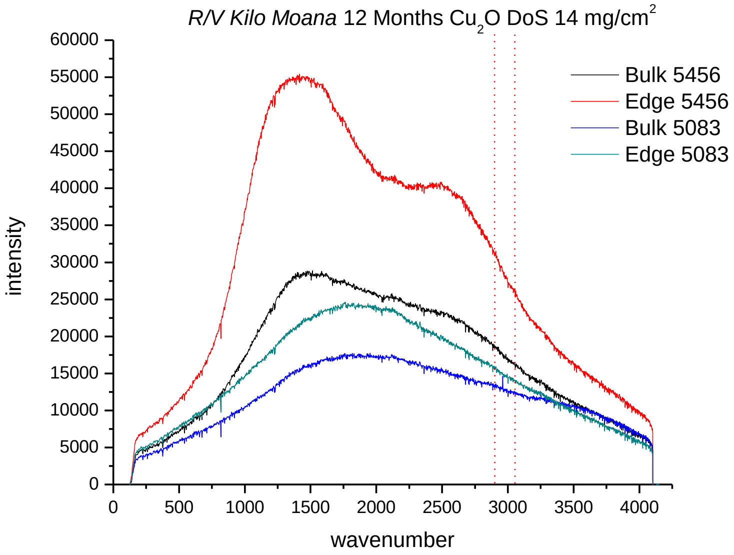

Figure 3.35: R/V Kilo Moana 12 Month AA5083 and AA5456 DoS 10/14 mg/cm^2 highlighting Cu_2O peaks for the center (bulk) and edge of 3/8" CDA inserts

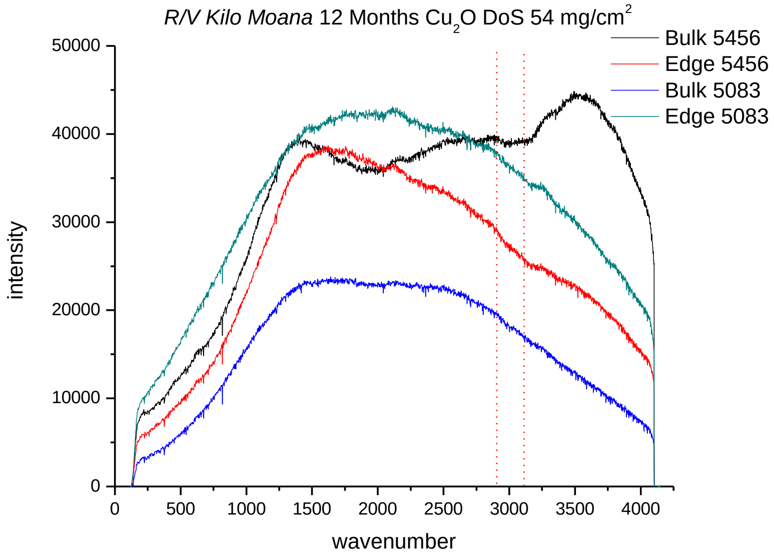

Figure 3.36: R/V Kilo Moana 12 Month AA5083 and AA5456 DoS 54 mg/cm^2 highlighting Cu_2O peaks for the center (bulk) and edge of 3/8" CDA inserts

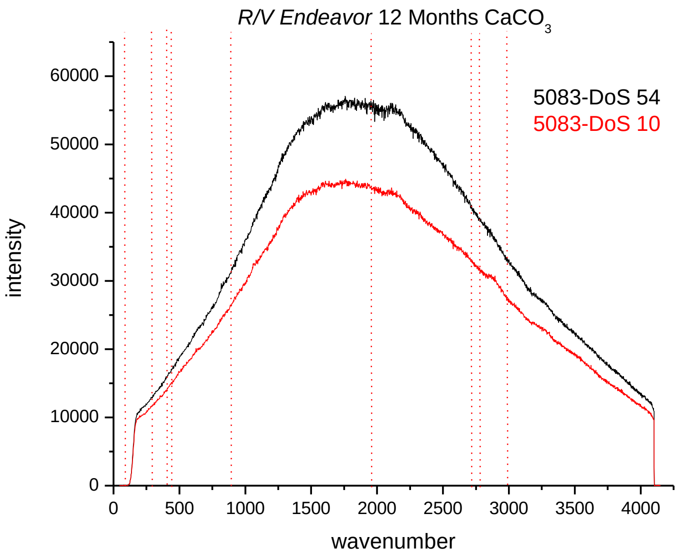

Figure 3.37: R/V Endeavor 12 Month AA5083-H116 DoS 10 & 54 mg/cm^2 sample with 3/8" CDA insert highlighting $CaCO_3$ peak locations

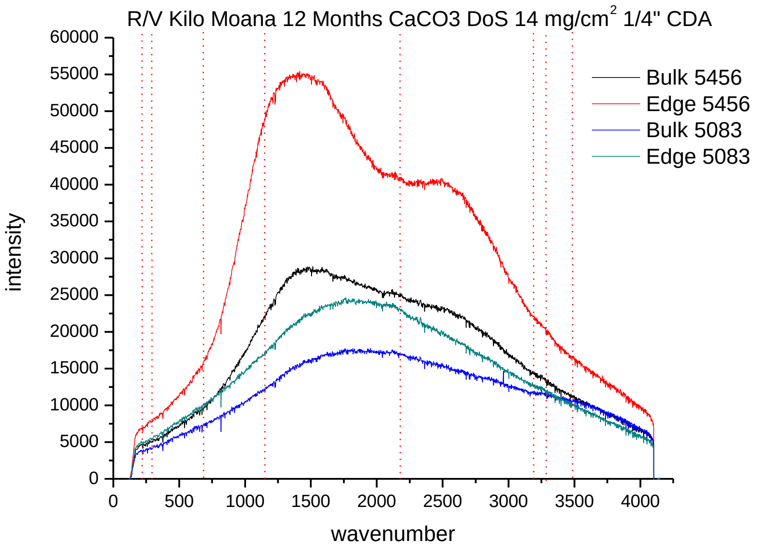

Figure 3.38: R/V Kilo Moana 12 Month AA5083 and AA5456 DoS 14 mg/cm^2 highlighting $CaCO_3$ peaks for the center (bulk) and edge of 1/4" CDA inserts

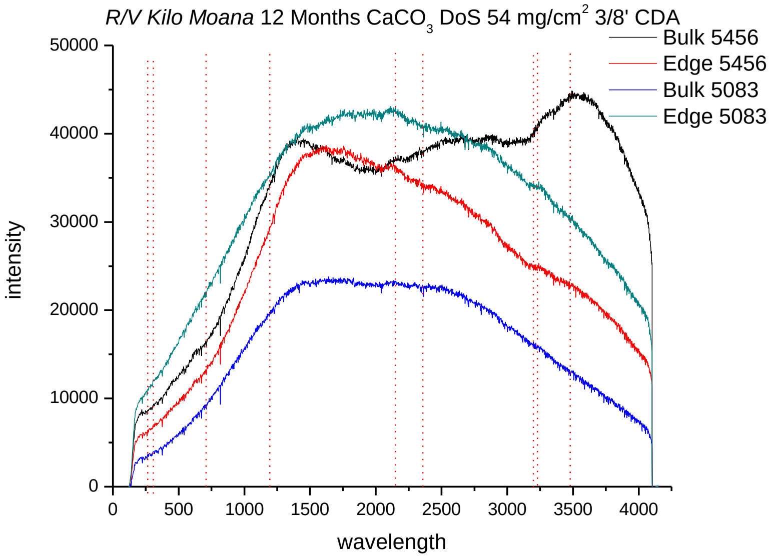

Figure 3.39: R/V Kilo Moana 12 Month AA5083 and AA5456 DoS 54 mg/cm^2 highlighting $CaCO_3$ peaks for the center (bulk) and edge of 3/8" CDA inserts

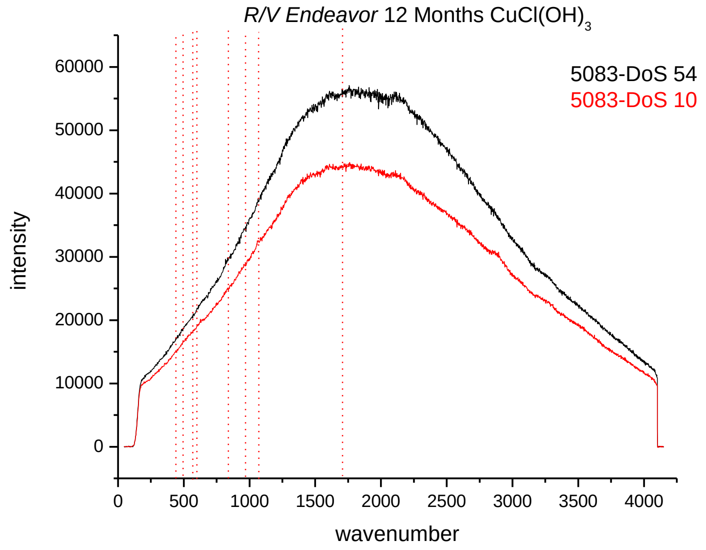

Figure 3.40: R/V Endeavor 12 Month AA5083-H116 DoS 10 & 54 mg/cm^2 sample with 3/8" CDA insert highlighting CuCl(OH)$_3$ peak locations

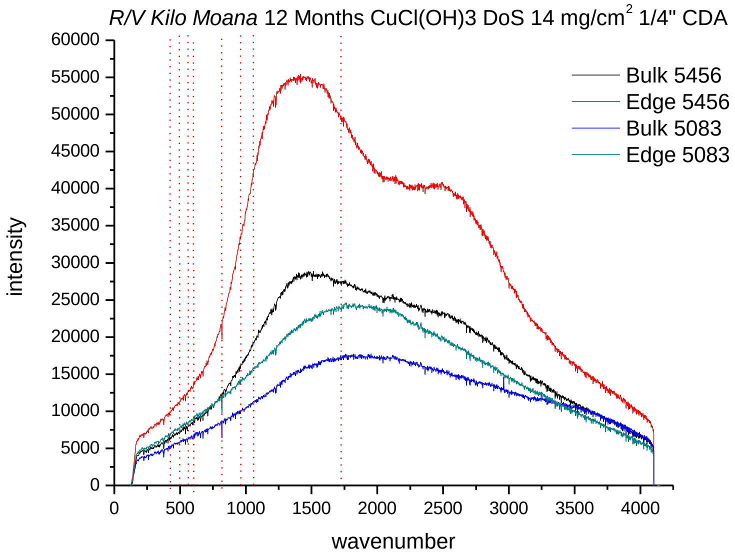

Figure 3.41: R/V Kilo Moana 12 Month AA5083 and AA5456 DoS 54 mg/cm^2 highlighting CuCl(OH)$_3$ peaks for the center (bulk) and edge of 1/4" CDA inserts

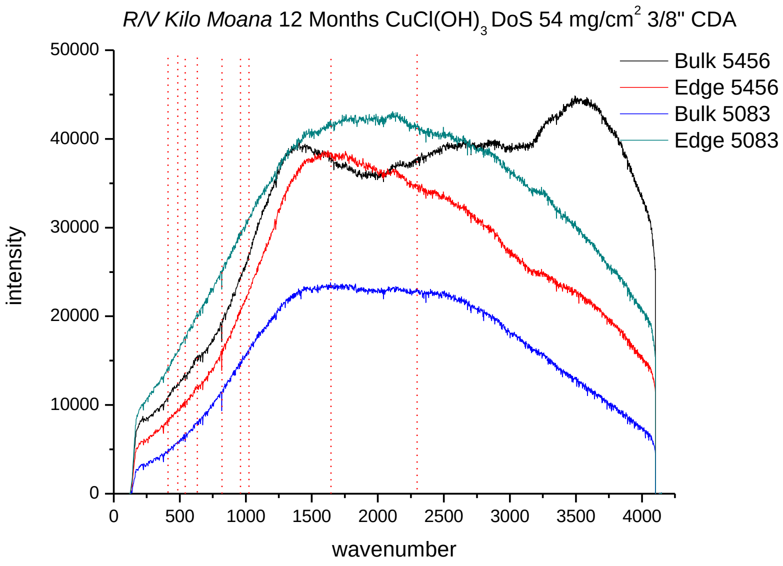

Figure 3.42: R/V Kilo Moana 12 Month AA5083 and AA5456 DoS 54 mg/cm^2 highlighting CuCl(OH)$_3$ peaks for the center (bulk) and edge of 3/8" CDA inserts

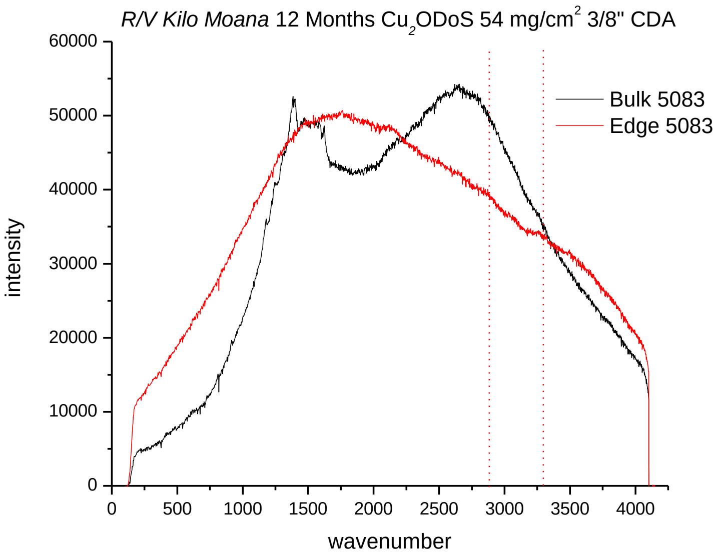

Figure 3.43: R/V Kilo Moana 12 Month AA5083-H116 DoS 54 mg/cm^2 sample insert highlighting Cu$_2$O peaks for the center (bulk) and edge of 3/8" CDA inserts

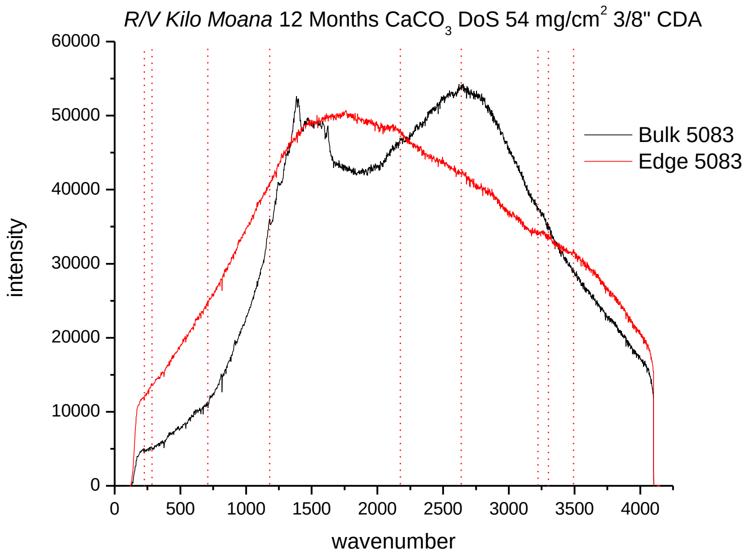

Figure 3.44: R/V Kilo Moana 12 Month AA5083-H116 DoS 54 mg/cm^2 sample insert highlighting $CaCO_3$ peaks for the center (bulk) and edge of 3/8" CDA inserts

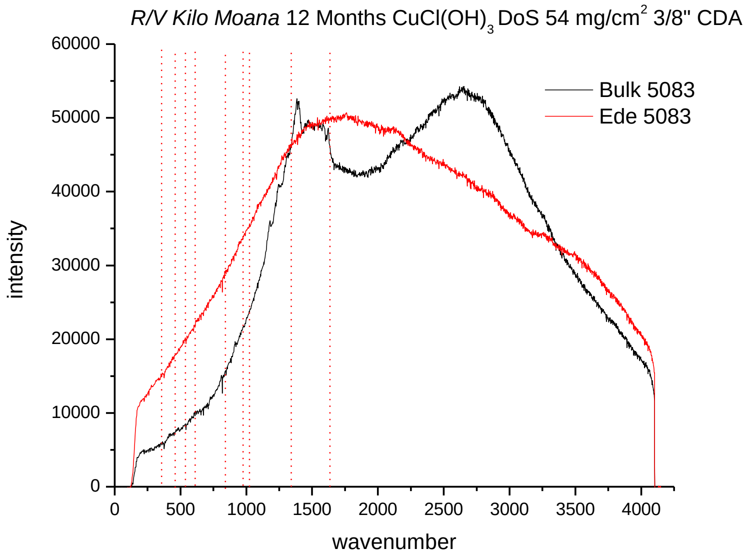

Figure 3.45: R/V Kilo Moana 12 Month AA5083-H116 DoS 54 mg/cm^2 sample insert highlighting $CuCl(OH)_3$ peaks for the center (bulk) and edge of 3/8" CDA inserts

3.11.3 XPS

XPS was performed on *R/V Endeavor* 12 month returns using a bracket holder. CDA 706 inserts were scanned and analyzed after the peaks were normalized to 1.

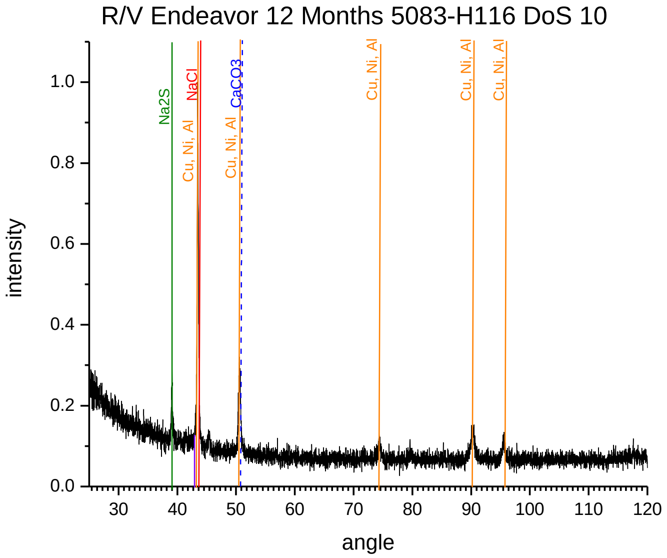

Figure 3.46: R/V Endeavor 12 Month AA5083-H116 DoS 10 mg/cm^2 sample insert highlight Na$_2$S, Cu, Ni, Al, NaCl, CaCO$_3$ corrosion products of 3/8” CDA inserts

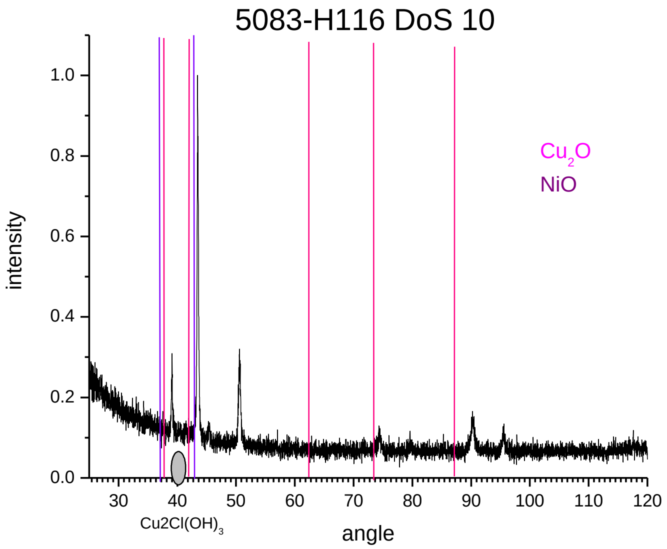

Figure 3.47: R/V Endeavor 12 Month AA5083-H116 DoS 10 mg/cm^2 *sample insert highlight* Cu_2O *and NiO corrosion products of 3/8" CDA inserts.* $Cu_2Cl(OH)_3$ *peaks are located very closely in the gray circle around an angle of 40.*

3.11.4 XRD

XRD scans were performed by Catherine Anne Dukes at the University of Virginia. Using a 200 µm beam, a pass energy (PE) of 280 eV, for 5 cycles and a time/step of 50 ms.

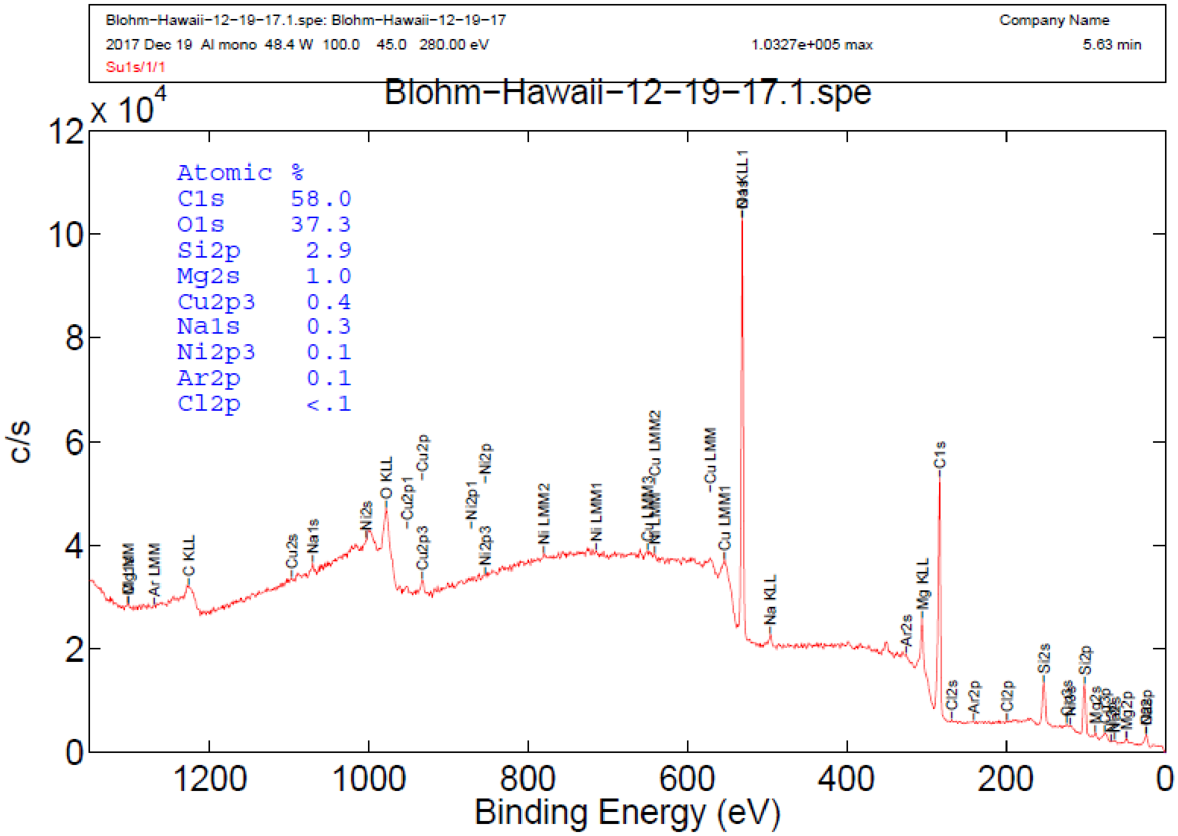

Figure 3.48: R/V Kilo Moana 12 Month AA5083-H116 DoS 10 mg/cm^2 with a 3/8" CDA insert. This scan was not sputtered, and scanned in the center of the CDA 706 insert

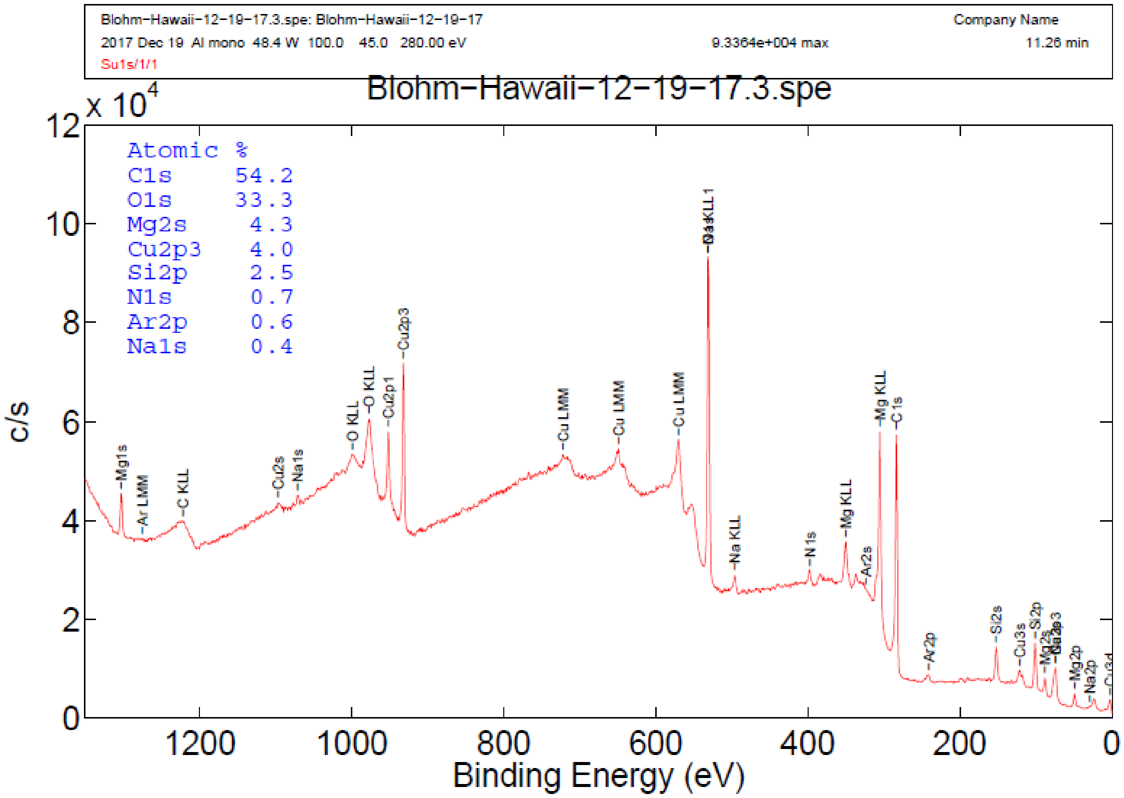

Figure 3.49: R/V Kilo Moana 12 Month AA5083-H116 DoS 10 mg/cm^2 with a 3/8" CDA insert. This scan was sputtered with 3keV Ar$^+$ 3x3mm using zalar motion, and scanned in the center of the CDA 706 insert

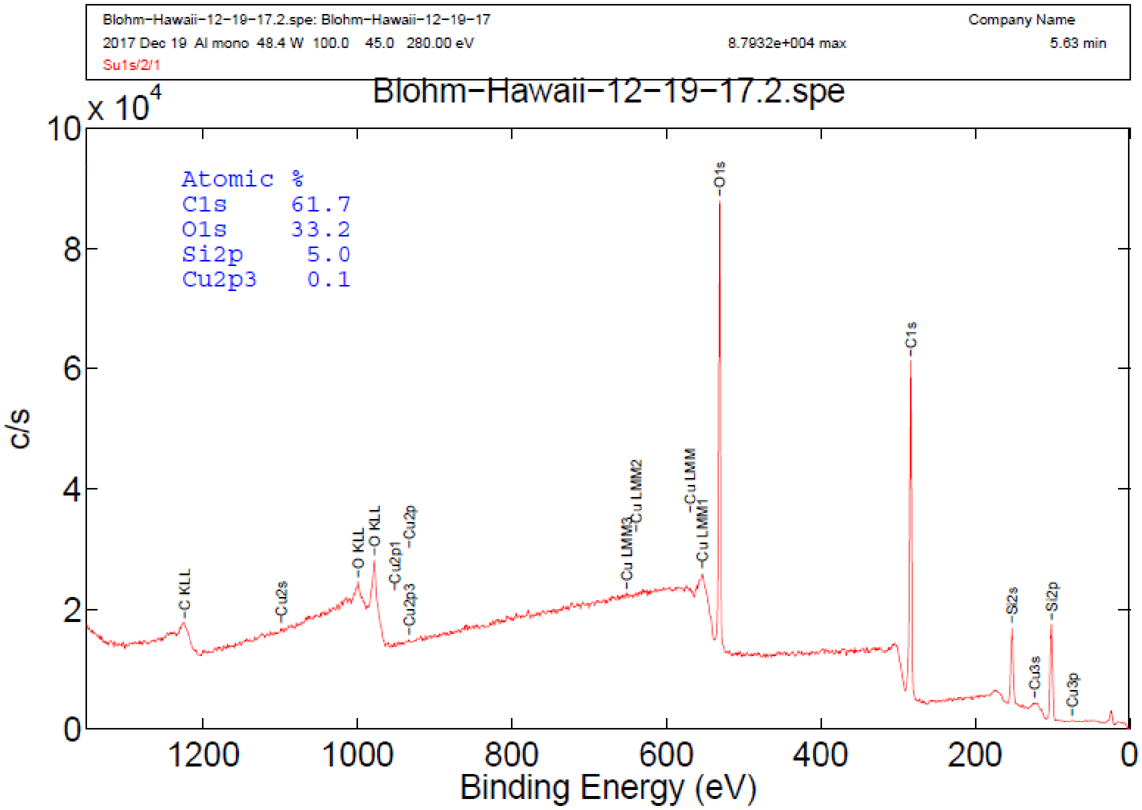

Figure 3.50: R/V Kilo Moana 12 Month AA5083-H116 DoS 10 mg/cm^2 with a 3/8" CDA insert. This scan was not sputtered, and scanned at the edge of the CDA 706 insert

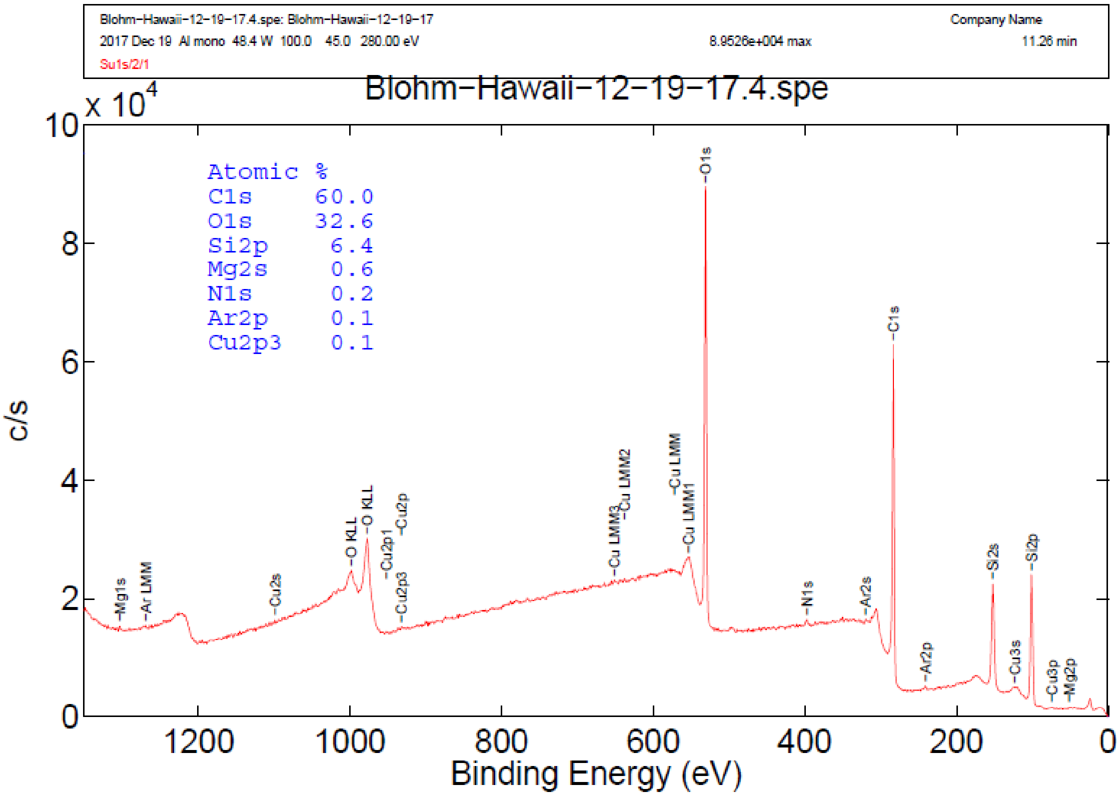

Figure 3.51: R/V Kilo Moana 12 Month AA5083-H116 DoS 10 mg/cm^2 with a 3/8" CDA insert. This scan was sputtered with 3keV Ar$^+$ 3x3mm using zalar motion, and scanned at the edge of the CDA 706 insert

3.11.5 Exposure Throwing Power Analysis

Additional IGC measurements vs throwing power comparisons are plotted below.

3.11.5.1 Location Comparisons

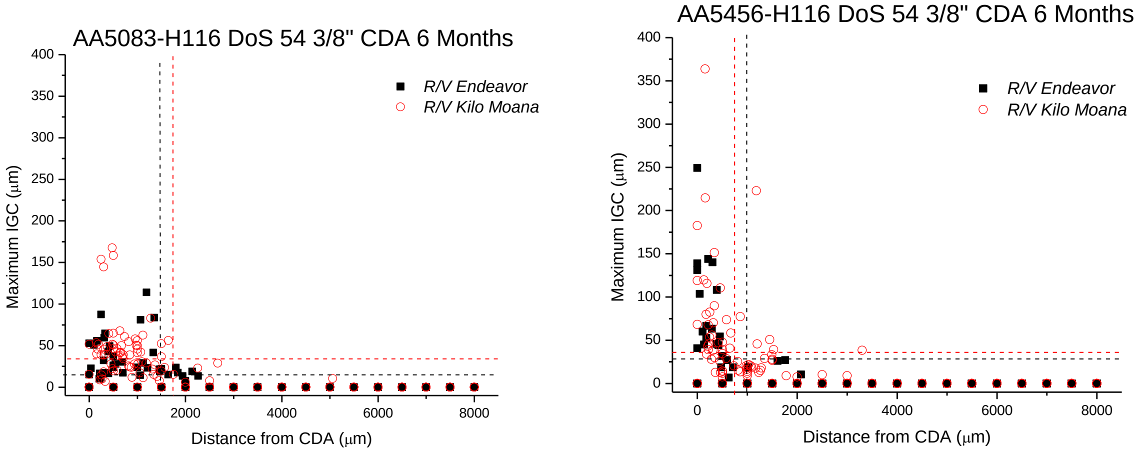

Figure 3.52: a. AA5083-H116 DoS 54 mg/cm^2 with a 3/8" CDA insert showing maximum IGC vs throwing distance from the coupling interface for R/V Endeavor and R/V Kilo Moana 6-month exposure b. AA5456-H116 DoS 54 mg/cm^2 with a 3/8" CDA insert showing maximum IGC vs throwing distance from the coupling interface for R/V Endeavor and R/V Kilo Moana 6-month exposure

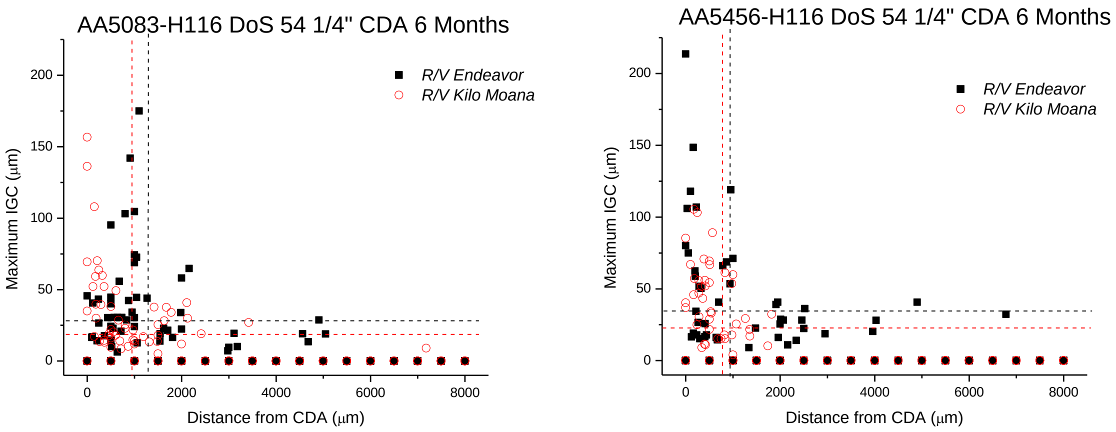

Figure 3.53: a. AA5083-H116 DoS 54 mg/cm^2 with a 1/4" CDA insert showing maximum IGC vs throwing distance from the coupling interface for R/V Endeavor and R/V Kilo Moana 6-month exposure b. AA5456-H116 DoS 54 mg/cm^2 with a 1/4" CDA insert showing maximum IGC vs throwing distance from the coupling interface for R/V Endeavor and R/V Kilo Moana 6-month exposure

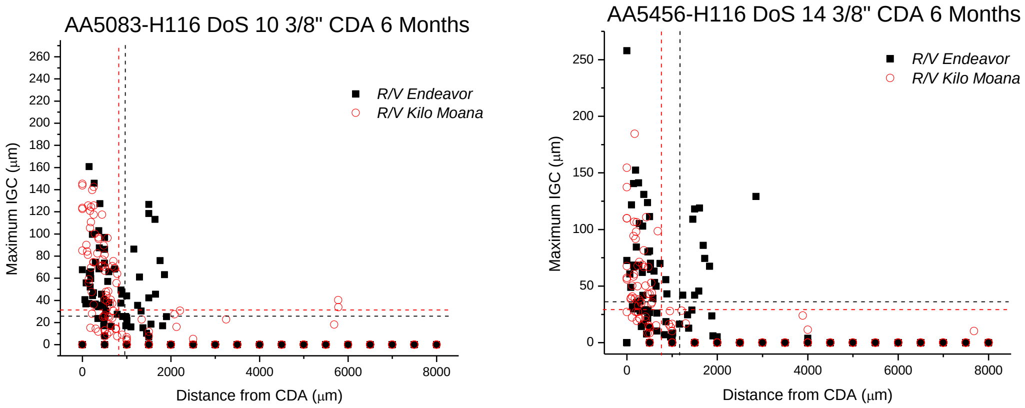

Figure 3.54: a. AA5083-H116 DoS 10 mg/cm^2 with a 3/8" CDA insert showing maximum IGC vs throwing distance from the coupling interface for R/V Endeavor and R/V Kilo Moana 6-month exposure b. AA5456-H116 DoS 14 mg/cm^2 with a 3/8" CDA insert showing maximum IGC vs throwing distance from the coupling interface for R/V Endeavor and R/V Kilo Moana 6-month exposure

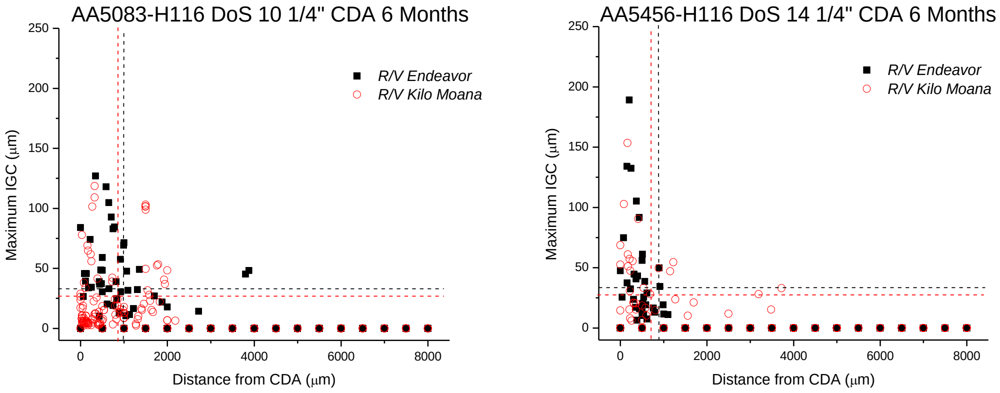

Figure 3.55: a. AA5083-H116 DoS 10 mg/cm^2 with a 1/4" CDA insert showing maximum IGC vs throwing distance from the coupling interface for R/V Endeavor and R/V Kilo Moana 6-month exposure b. AA5456-H116 DoS 14 mg/cm^2 with a 1/4" CDA insert showing maximum IGC vs throwing distance from the coupling interface for R/V Endeavor and R/V Kilo Moana 6-month exposure

3.11.5.2 Duration Comparison

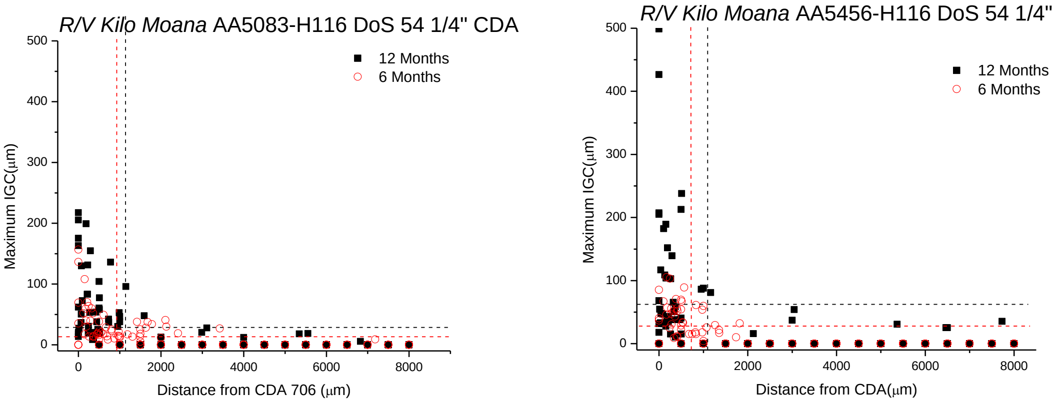

Figure 3.56: a. AA5083-H116 DoS 54 mg/cm^2 with a 1/4" CDA insert showing maximum IGC vs throwing distance from the coupling interface for the R/V Kilo Moana 6 & 12-month exposure b. AA5456-H116 DoS 54 mg/cm^2 with a 1/4" CDA insert showing maximum IGC vs throwing distance from the coupling interface for the R/V Kilo Moana 6 & 12-month exposure

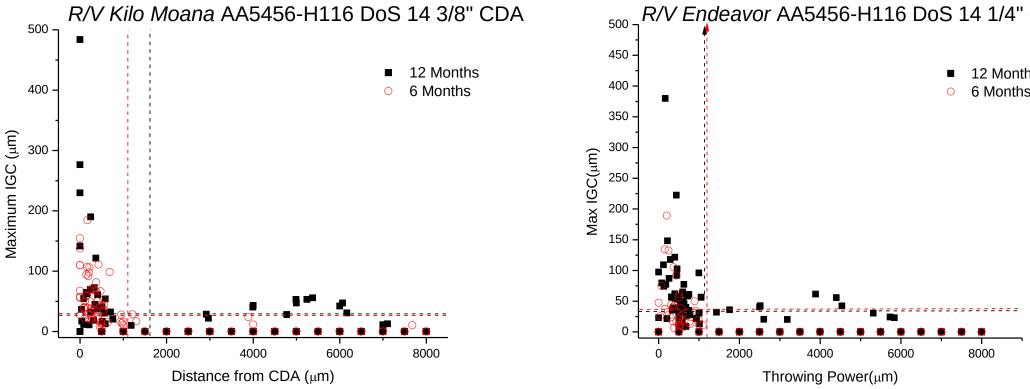

Figure 3.57: a. AA5456-H116 DoS 14 mg/cm^2 with a 3/8" CDA insert showing maximum IGC vs throwing distance from the coupling interface for the R/V Endeavor 6 & 12-month exposure b. AA5456-H116 DoS 54 mg/cm^2 with a 1/4" CDA insert showing maximum IGC vs throwing distance from the coupling interface for the R/V Endeavor 6 & 12-month exposure

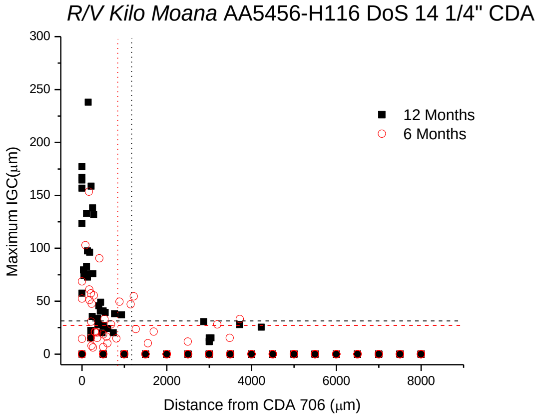

Figure 3.58: AA5456-H116 DoS 14 mg/cm^2 with a 1/4" CDA insert showing maximum IGC vs throwing distance from the coupling interface for the R/V Kilo Moana 6 & 12-month exposure

3.11.5.3 DoS Comparison

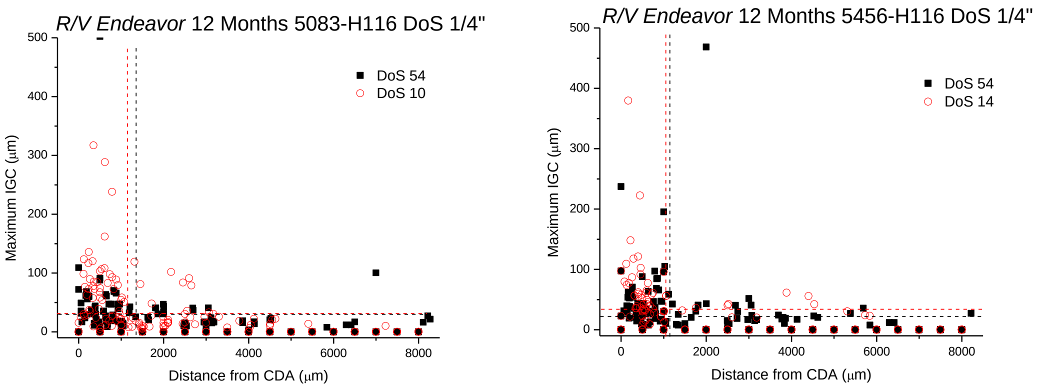

Figure 3.59: a. AA5083-H116 with a 1/4" CDA for the R/V Endeavor 12-month exposure insert showing maximum IGC vs throwing distance from the coupling interface for DoS 10 and DoS 54 mg/cm^2 b. AA5456-H116 with a 1/4" CDA for the R/V Endeavor 12-month exposure insert showing maximum IGC vs throwing distance from the coupling interface for DoS 14 and DoS 54 mg/cm^2

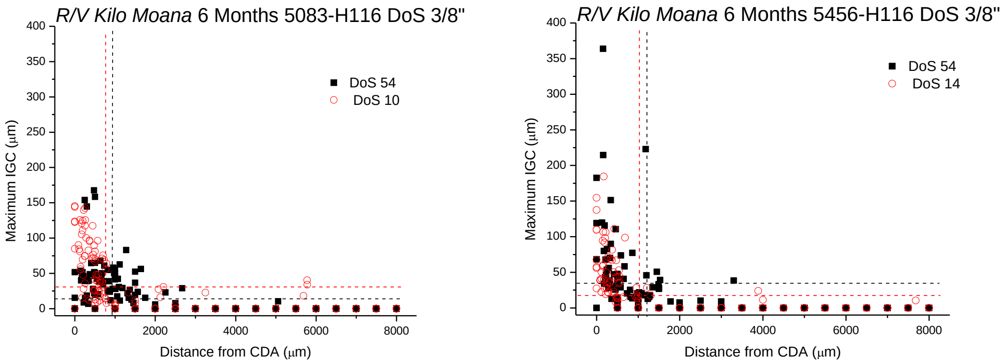

Figure 3.60: a. AA5083-H116 with a 3/8" CDA for the R/V Kilo Moana 6-month exposure insert showing maximum IGC vs throwing distance from the coupling interface for DoS 10 and DoS 54 mg/cm^2 b. AA5456-H116 with a 3/8" CDA for the R/V Kilo Moana 6-month exposure insert showing maximum IGC vs throwing distance from the coupling interface for DoS 14 and DoS 54 mg/cm^2

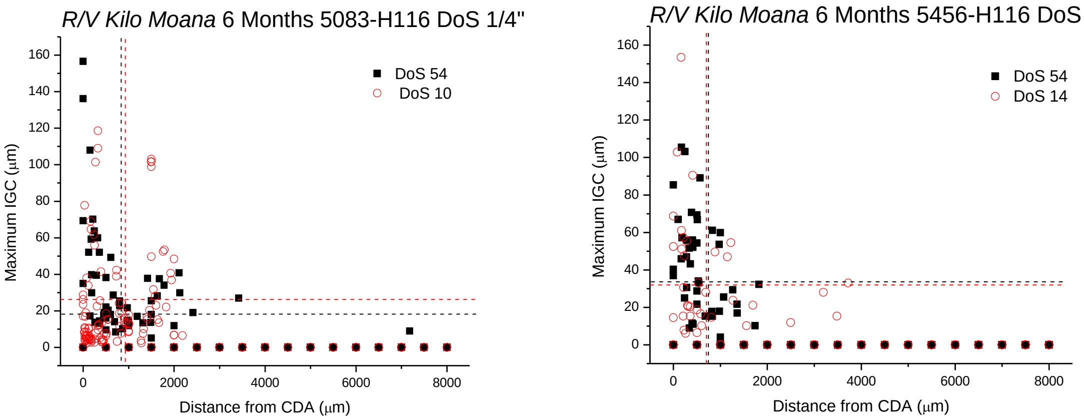

Figure 3.61: a. AA5083-H116 with a 1/4" CDA for the R/V Kilo Moana 6-month exposure insert showing maximum IGC vs throwing distance from the coupling interface for DoS 10 and DoS 54 mg/cm^2 b. AA5456-H116 with a 1/4" CDA for the R/V Kilo Moana 6-month exposure insert showing maximum IGC vs throwing distance from the coupling interface for DoS 14 and DoS 54 mg/cm^2

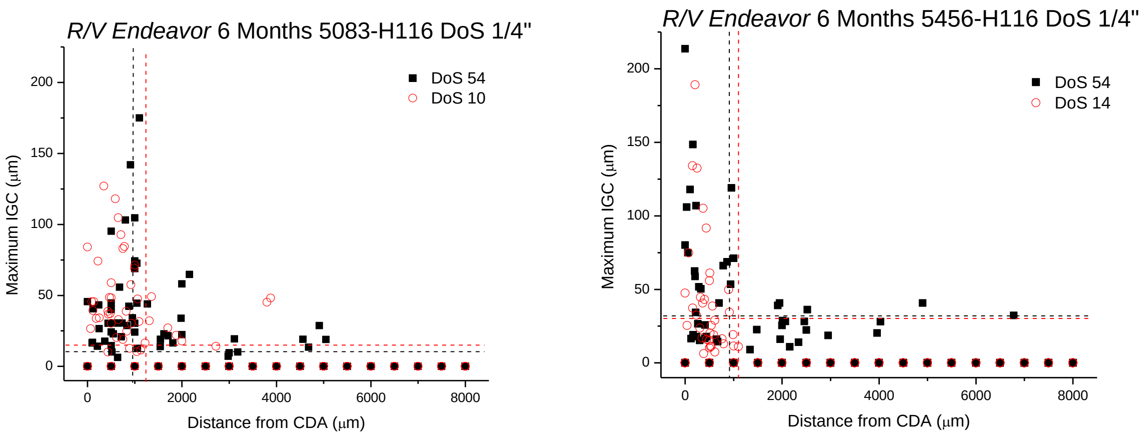

Figure 3.62: a. AA5083-H116 with a 1/4" CDA for the R/V Endeavor 6-month exposure insert showing maximum IGC vs throwing distance from the coupling interface for DoS 10 and DoS 54 mg/cm^2 b. AA5456-H116 with a 1/4" CDA for the R/V Endeavor 6-month exposure insert showing maximum IGC vs throwing distance from the coupling interface for DoS 14 and DoS 54 mg/cm^2

3.11.5.4 CDA Insert Comparison

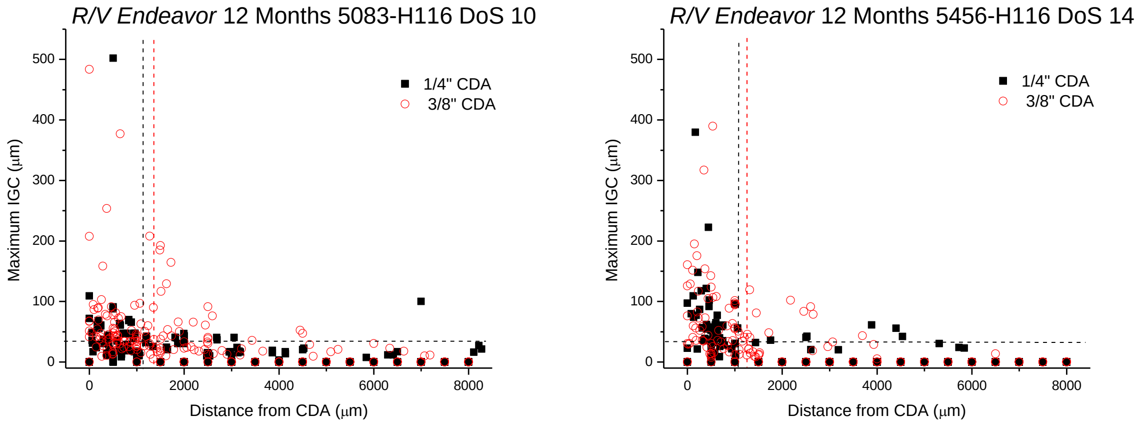

Figure 3.63: a. AA5083-H116 DoS 10 mg/cm^2 for the R/V Endeavor 12-month exposure showing maximum IGC vs throwing distance from the coupling interface for ¼" and 3/8" CDA inserts b. AA5456-H116 DoS 14 mg/cm^2 for the R/V Endeavor 12-month exposure showing maximum IGC vs throwing distance from the coupling interface for ¼" and 3/8" CDA inserts

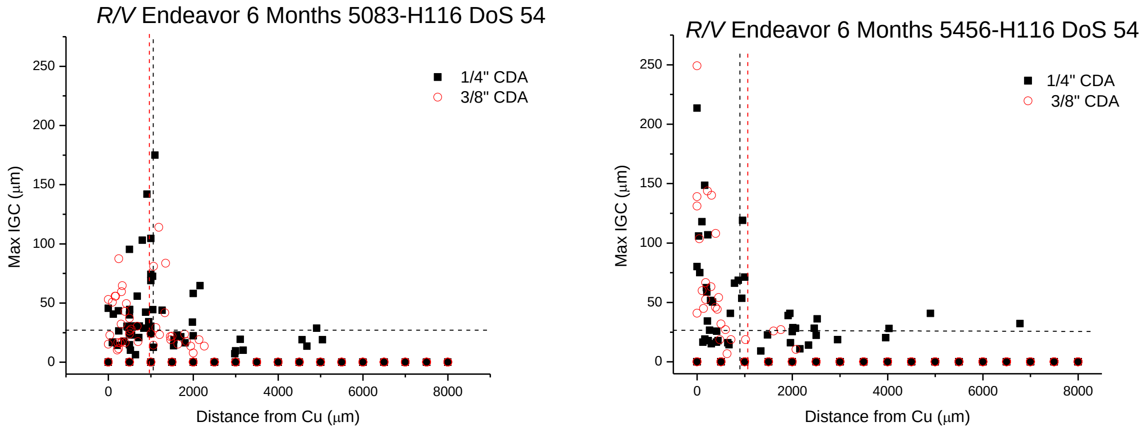

Figure 3.64: a. AA5083-H116 DoS 54 mg/cm^2 *for the R/V Endeavor 6-month exposure showing maximum IGC vs throwing distance from the coupling interface for ¼" and 3/8" CDA inserts b. AA5456-H116 DoS 54 mg/cm*^{2} *for the R/V Endeavor 6-month exposure showing maximum IGC vs throwing distance from the coupling interface for ¼" and 3/8" CDA inserts*

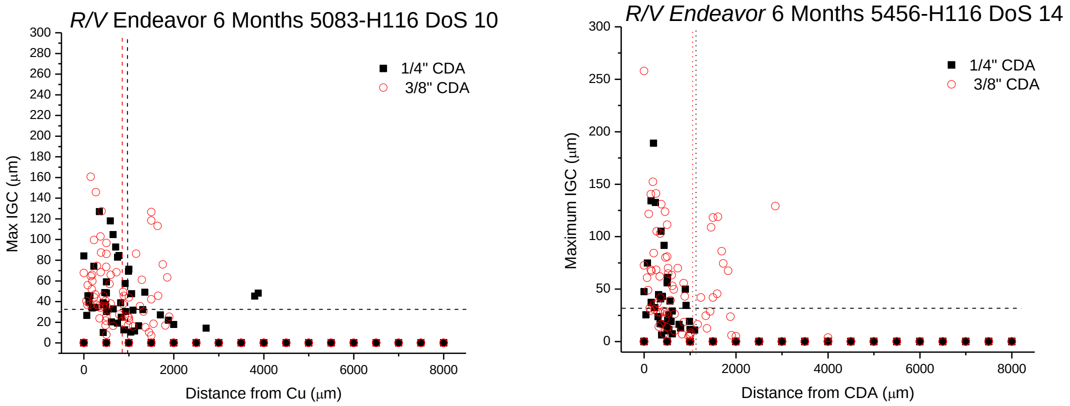

Figure 3.65: a. AA5083-H116 DoS 10 mg/cm^2 *for the R/V Endeavor 6-month exposure showing maximum IGC vs throwing distance from the coupling interface for ¼" and 3/8" CDA inserts b. AA5456-H116 DoS 14 mg/cm*^{2} *for the R/V Endeavor 6-month exposure showing maximum IGC vs throwing distance from the coupling interface for ¼" and 3/8" CDA inserts*

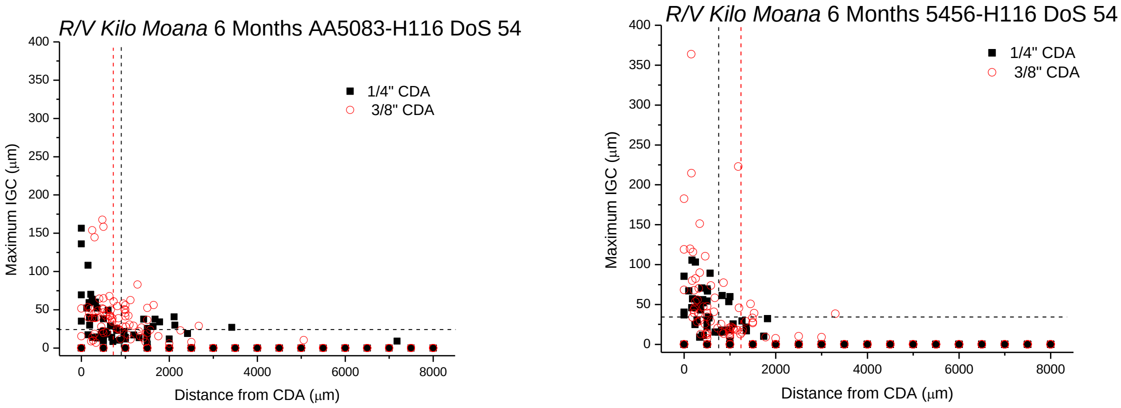

Figure 3.66: a. AA5083-H116 DoS 54 mg/cm^2 for the R/V Kilo Moana 6-month exposure showing maximum IGC vs throwing distance from the coupling interface for ¼" and 3/8" CDA inserts b. AA5456-H116 DoS 54 mg/cm^2 for the R/V Kilo Moana 6-month exposure showing maximum IGC vs throwing distance from the coupling interface for ¼" and 3/8" CDA inserts

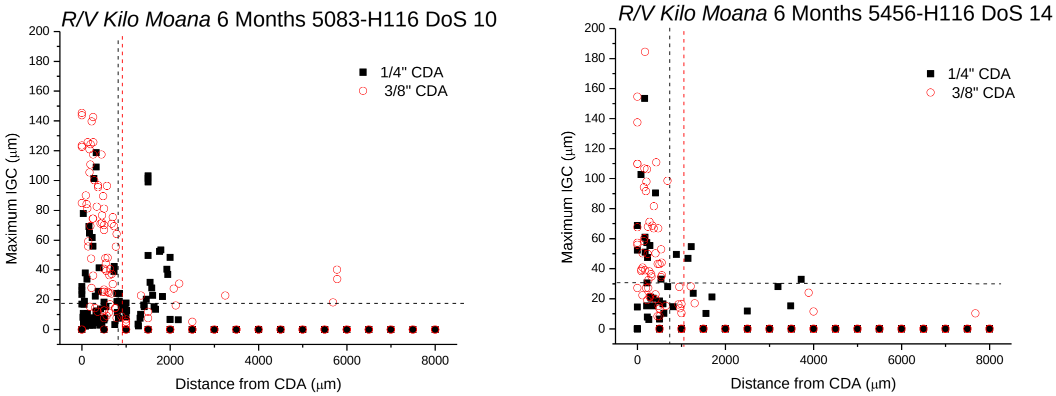

Figure 3.67: a. AA5083-H116 DoS 10 mg/cm^2 for the R/V Kilo Moana 6-month exposure showing maximum IGC vs throwing distance from the coupling interface for ¼" and 3/8" CDA inserts b. AA5456-H116 DoS 14 mg/cm^2 for the R/V Kilo Moana 6-month exposure showing maximum IGC vs throwing distance from the coupling interface for ¼" and 3/8" CDA inserts

3.11.5.5 Alloy Comparison

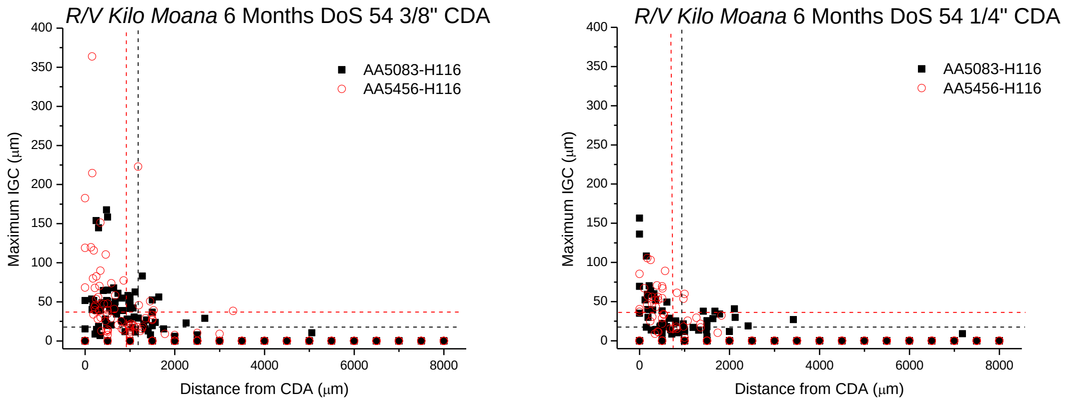

Figure 3.68: a. R/V Kilo Moana 6-month exposure for DoS 54 mg/cm^2 with a 3/8" CDA insert showing maximum IGC vs throwing distance from the coupling interface for AA5083 and AA5456 b. R/V Kilo Moana 6-month exposure for DoS 54 mg/cm^2 with a 1/4" CDA insert showing maximum IGC vs throwing distance from the coupling interface for AA5083 and AA5456

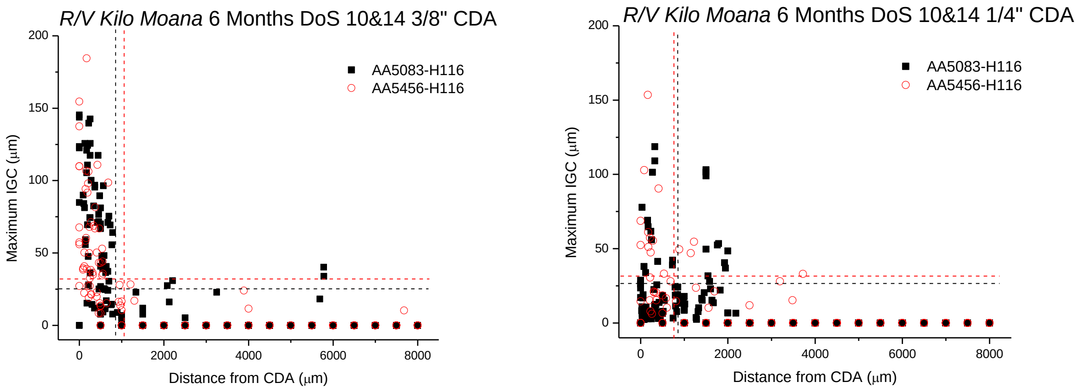

Figure 3.69: a. R/V Kilo Moana 6-month exposure for DoS 10 & 14 mg/cm^2 with a 3/8" CDA insert showing maximum IGC vs throwing distance from the coupling interface for AA5083 and AA5456 b. R/V Kilo Moana 6-month exposure for DoS 10 & 14 mg/cm^2 with a 1/4" CDA insert showing maximum IGC vs throwing distance from the coupling interface for AA5083 and AA5456

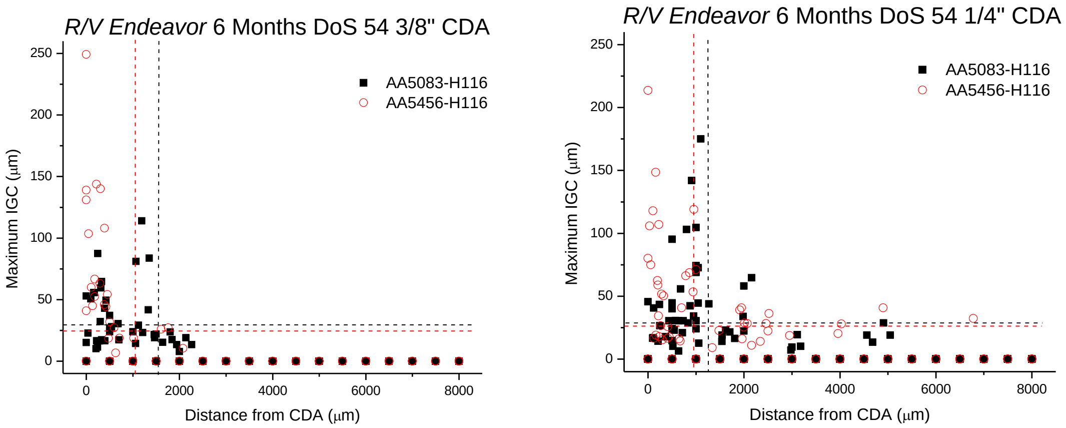

Figure 3.70: a. R/V Endeavor 6-month exposure for DoS 54 mg/cm^2 with a 3/8" CDA insert showing maximum IGC vs throwing distance from the coupling interface for AA5083 and AA5456 b. R/V Endeavor 6-month exposure for DoS 54 mg/cm^2 with a 1/4" CDA insert showing maximum IGC vs throwing distance from the coupling interface for AA5083 and AA5456

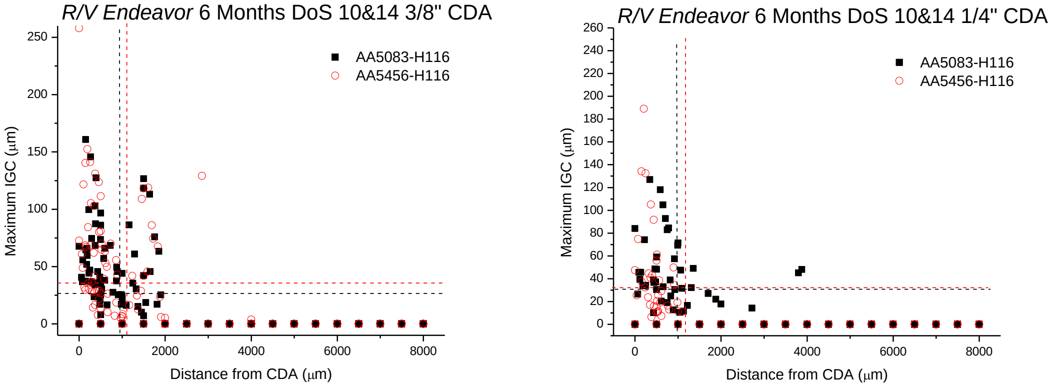

Figure 3.71: a. R/V Endeavor 6-month exposure for DoS 10 & 14 mg/cm^2 with a 3/8" CDA insert showing maximum IGC vs throwing distance from the coupling interface for AA5083 and AA5456 b. R/V Endeavor 6-month exposure for DoS 10 & 144 mg/cm^2 with a 1/4" CDA insert showing maximum IGC vs throwing distance from the coupling interface for AA5083 and AA5456

4 A Combined Experiment and Modeling Analysis of ASTM G85 WB Accelerated Corrosion Testing of Galvanically Coupled Sensitized AA5456-H116 and CDA 706 Cupronickel

Please note that OLI calculations and COMSOL modeling were performed by:
Chao (Gilbert) Liu

4.1 Abstract

Galvanically coupled samples of AA5456-H116, an aluminum-magnesium alloy, and a cupronickel CDA 706, otherwise denoted C70600, undergo accelerated corrosion using ASTM G85 wet bottom (G85 WB) and ASTM G85 WB Modified (G85 WB Mod) testing. Surface and subsurface damage of AA5456-H116 was investigated and quantified. The G85 WB test is less harsh than the Modified G85 WB, and IGC damage was found to correlate with the severity of the test. These results were compared to Finite Element Modeling results investigating relative humidity (RH) and water layer (WL) thickness. The best fit between experimental results and the modeling results was found when modeling assumed that a 3000 μm water layer was formed during the spray portion of the G85 cycle followed by the measured decrease in RH, which led to a less intense IGC attack that was more focused in the proximity of the CDA/AA5456-H116 interface.

4.2 Overview

The following chapter explores accelerated corrosion testing of galvanically coupled samples, as well as a modelling investigation to correlate with experimental results. AA5456-H116 samples with CDA 706 inserts were identical to those used in outdoor exposures in Chapter 3. Finite Element Modeling using COMSOL^{TM} with experimentally derived polarization curves serving as boundary conditions was utilized to mimic the IGC trends with known surface chemistry and humidity values as a function of time. Outdoor exposure samples surface chemistry is difficult to model, therefore, G85 WB tests were used to accelerate corrosion resulting in results that can be tied to modeling behavior, as well as outdoor exposure results.

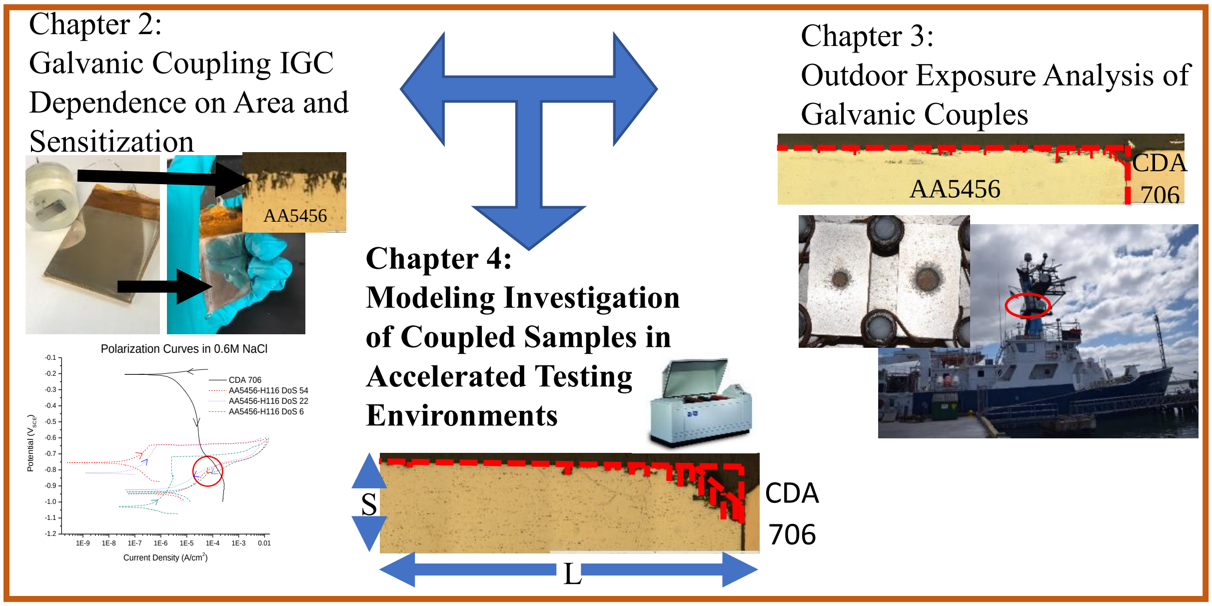

Schematic for Thesis Organization

4.3 Introduction

AA5XXX aluminum magnesium alloys are used widely in naval superstructures. In these conditions, AA5XXX alloys are exposed to atmospheric corrosion for long service lives. This corrosion is accelerated with increasing degree of sensitization (DoS). With increased time and temperature, AA5XXX alloys containing greater than 3wt% Mg sensitize at field temperatures as low as 50°C[1] which are easily achievable on sun-exposed surfaces. With increased sensitization, the active β phase (Al_3Mg_2) precipitates at the grain boundaries creating a direct pathway for intergranular corrosion (IGC) propagation[2]. With stress added to the system, intergranular stress corrosion cracking (IGSCC) is probable. Lim et al. showed that with AA5083-H116, IGC accelerates in artificial seawater with increased DoS and applied potential, and is most rapid through rapid in the rolling direction of the alloy[3]. AA5XXX series alloy microstructures have elongated grains on the longitudinal by long transvere (LS) and short transverse (ST) planes, and wide grains on the long transverse (LT) plane.

CDA 706, a cupronickel alloy, is widely utilized in marine structures for its corrosion resistance, bacteriostatic, and anti-microfouling properties[4,5]. When the materials are coupled in naval applications, CDA 706 acts as the cathode in a galvanic couple with AA5XXX. This coupling accelerates IGC of the AA5XXX alloys. Mizuno et al. showed that for galvanic coupling in both full immersion and atmospheric conditions, increased cathode size accelerates IGC in AA5083-H131[6,7]. Mizuno et al. used AA5083-H131 and AISI 4340 to investigate the throwing power for coupled samples[6]. It was found that IGC propagates further from the galvanic interface with increased cathode:anode ratio and IGC depth increases[6].

Past work focuses mainly on experimental full immersion and thin film studies. However, when samples are exposed to atmosphere, they become exposed to thin electrolyte films that fluctuate diurnally with RH. Accelerated corrosion testing with atmospheric corrosion chambers are heavily utilized to evaluate material corrosion performance. ASTM G85[8] is an aggressive laboratory atmospheric test using an acidic solution pH and fluctuating atmosphere conditions throughout the test. Testing with wet bottom (WB) conditions maintain more stable RH over dwells than dry bottom (DB)[9]. Under WB conditions, approximately an inch of water is maintained at the bottom of the corrosion chamber. This ensures that the chamber does not dry which would, in turn, decrease the corrosion rate[8].

4.4 Materials

Galvanically coupled samples were prepared using 5456-H116 ¼” plate was provided by the Naval Surface Warfare Center-Carderock Division (NSWCCD). 5456-H116 samples, cut to 1” x 1.5” on the LT face, were heat treated at 100°C for 14 days to reach a DoS of 54 mg/cm^2, which was validated using ASTM G67[10] nitric acid mass loss test (NAMLT). CDA 706 rods, ¼” and 3/8” in diameter, were provided by Metal Samples. Silver (Ag) samples, specifically UNS P07010 99.99% were provided by Metal Samples. Ag samples were polished to 1200 grit with silicon carbide papers prior to testing. The compositions of AA5456-H116 and CDA 706 are shown respectively in Table 4.1 and 4.2. The main alloying element of AA5456-H116 is magnesium with a temper of H116 which designates that the alloy is special strain hardened, and corrosion resistant[11]. Two AA5456-H116 samples, after polishing to 1200 grit with silicon carbide paper, 3/8” CDA 706 inserts press fitted into the center. One of the AA5456-H116 samples had a 1/4” CDA 706 insert press fitted into the center. Assembled samples, prior to testing, can be seen in Figure 4.1.

Table 4.1: Alloy composition of 5456-H116 ¼” provided by NSWCCD (by materials certification)

5456-H116								
Element	Al	Mg	Fe	Si	Cr	Zn	Ti	Cu
Wt %	Rem.	5.2640	0.1830	0.1570	0.0930	0.0560	0.0263	0.0240

Table 4.2: Alloy composition of CDA 706 provided by Metal Samples (by materials certification)

CDA 706					
Element	Cu	Ni	Fe	Mn	Impurities
Wt %	87.778	9.948	1.453	0.793	Rem.

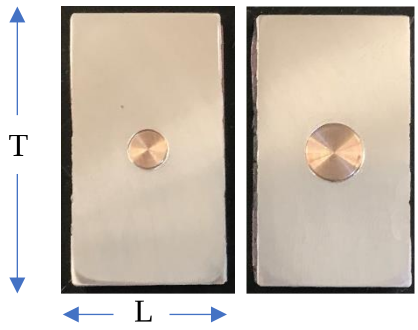

Figure 4.1: AA5456-H116 with ¼"and 3/8" CDA 706 inserts, respectively, prior to testing

4.5 Experimental Procedures

4.5.1 Standard G85 WB

One coupled sample with a 3/8" CDA 706 insert was placed in a Q-FOG Cycle Corrosion Tester (Model CCT) for G85-WB[8] testing along with 3 Ag samples. G85 WB calls for an electrolyte of 0.9M NaCl, pH adjusted to 2.9 with acetic acid. The test runs on a 6-hour cycle, in which samples were sprayed for 45 minutes, had a dry air purge for 120 minutes, followed by a dwell for 195 minutes. The relative humidity (RH), although it is not controlled, fluctuates over the testing cycle, as shown in Figure 4.2[12]. The time of wetness (TOW), provided by Parker[12], also varies, as shown in Figure 4.3 plotting impedance over time, where impedance was measured at a frequency of 26kHz. The sample is dry at low impedance, and wet at high impedance. The AA5456-H116 and CDA 706 coupled sample was removed after 31 days. Silver samples were removed after 50, 100, and 600 hours.

4.5.2 Modified G85 WB

One coupled sample with a 3/8" CDA 706 insert, and one with a ¼" CDA 706 insert were placed in a Q-FOG Cycle Corrosion Tester (Model CCT) along with five Ag samples for a modified G85 WB test. Samples were sprayed for 45 minutes, had a dry air purge for 1 minute, followed by a dwell for 314 minutes totaling the full 360-minute (6 hour) cycle. The electrolyte, as in G85 WB is 0.9M NaCl, pH adjusted to 2.9 with acetic acid with RH fluctuations as shown in Figure 4.2 for four cycles. The TOW fluctuates, as shown in Figure 4.3, where the samples are dry for less time than the standard G85 WB test. Also, over time, the sample stays wet longer and dries more slowly. Coupled samples were removed from the accelerated test after 2 weeks (14 days). Silver samples were removed sequentially after exposure for 50, 100, 200, 250, and 404 hours.

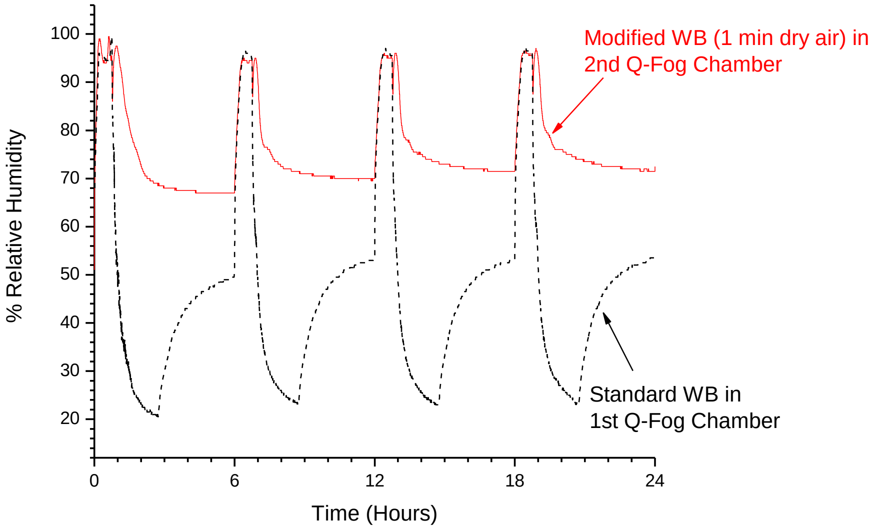

Figure 4.2[12]*: RH fluctuations over one day (4 cycles) for the Modified G85 WB and Standard G85 WB*

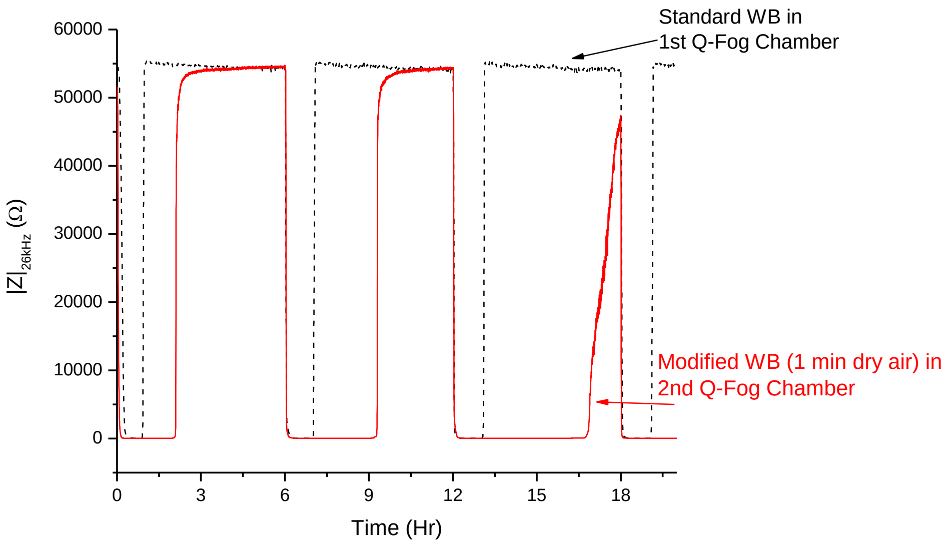

Figure 4.3[12]*: Impedance measured over 20 hours for Modified G85 WB and Standard G85 WB*

4.5.3 G85 Exposure Analysis

Samples, following exposure, were rinsed with deionized H_2O and dried with lab air. Before and after images are shown in Figure 4.4 a-c. From these macroscopic images, the surface damage on the AA5656-H116 and CDA 706 was quantified. Image J[13], after setting the scale to a known distance, was used for this quantification. On each image, eight equidistant measurements were taken around the AA5456-H116 and within the CDA 706 to measure the throwing power out on the AA5456, seen in Figure 4.5a, and cathodic protection by measuring uncorroded CDA 706 shown in Figure 4.5b. These distance measurements were averaged for comparison. Figure 4.5c shows the cross sections that were made for analysis. Samples were cut in quarters along the L direction with the edge pieces, furthest from the CDA 706 insert, were cut in halves along the T direction.

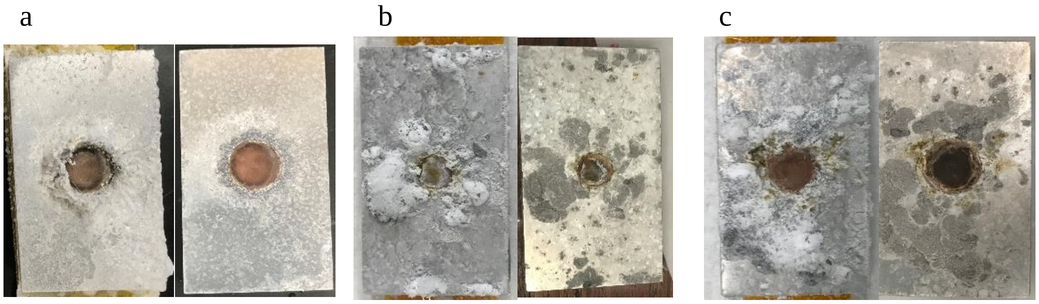

Figure 4.4: a. AA5456-H116 throwing power on surface of removals b. Cathodic protection on CDA 706 samples c. diagram of cross sectioning

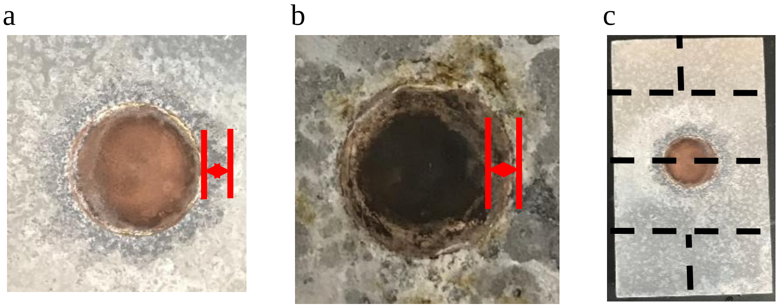

Figure 4.5: a. G85 WB before and after cleaning b. G85 Modified ¼" insert before and after cleaning c. G85 Modified 3/8" insert before and after cleaning

Following cross-sectioning, the two middle pieces were mounted to expose the CDA 706:AA5456-H116 SL face. The four edge pieces were mounted to expose the ST faces. These samples were polished to 1200 grit using silicon carbide paper, followed by 3 and 1 μm diamond suspension, and 0.05 μm colloidal silica. The CDA 706 and AA5456-H116 samples were imaged stitched using an optical microscope.

On one side of each coupled sample exposed to G85 Modified, there were large salt deposits. This resulted in great surface wastage. As this phenomena is not seen in outdoor exposures, half of the G85 WB samples were disregarded. To obtain the same total fields of view, the used half of each sample in the modified test was polished and imaged at a second depth to aquire more data to correlate to the G85 WB test. This salt cluster deposition is shown with G85 WB Modified ¼" CDA 706 insert in Figure 4.6.

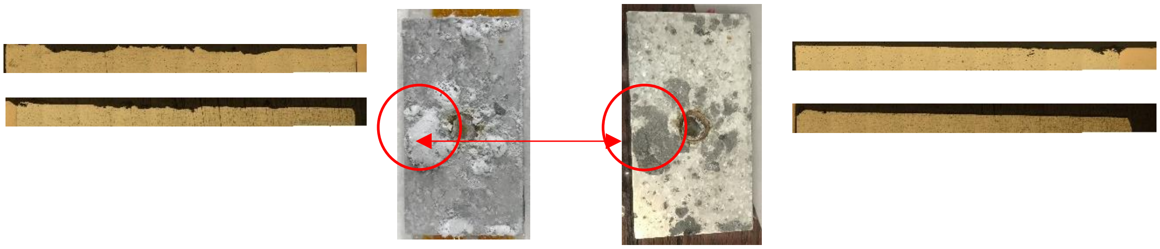

Figure 4.6: Cross sections of left and right side of AA5456-H116 with a CDA 706 ¼" insert. Salt deposition of uncleaned sample, results in large wastage that is seen on the cleaned sample surface. The left images were disregarded in IGC analysis.

Area summations of IGC damage were calculated using Image J. Each image, before analysis was opened in Image J, seen in Figure 4.7a, where under the analyze tab, the scale was set by changing the known distance using a measurement of the scale bar and set to global to save the scale. The area of interest was cropped, shown in Figure 4.7b, and the polygon tool was used to select areas of constituent particles and edited out using the fill tool under edit as shown in Figure 4.6c. The image was then converted to black and white by changing the image type to 8bit. The image was then adjusted using the threshold tool to 80% as shown in Figure 4.7d. Using the analyze particles tool, and selecting : display results, clear results, summarize, and inlude holes selected, the summarize tool was then utilized to show the total area that was shown to be red. The area of sample that was removed from machining, shown in Figure 4.7e, was measured and subtracted from this total area. This missing area was an artifact of machining, and was consistent across all samples.

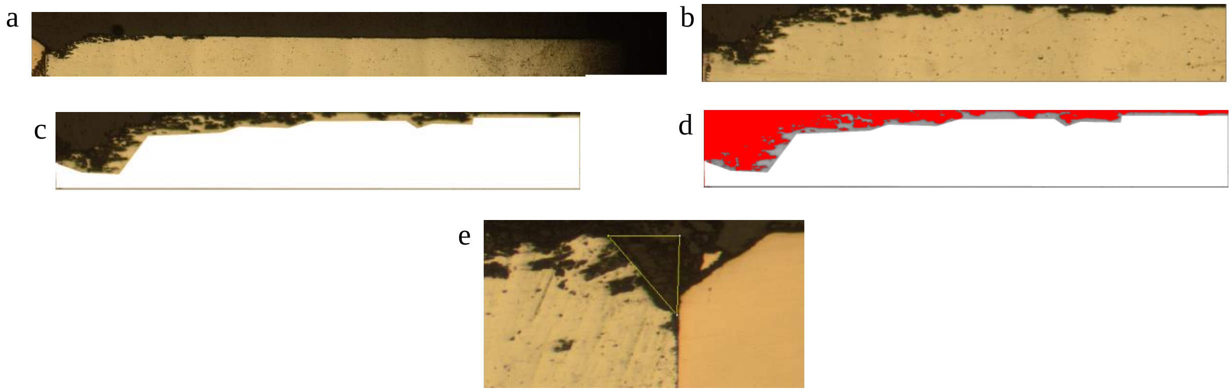

Figure 4.7: Image J Area Analysis a. Original image for analysis b. Image cropped c. Image after filling in all areas of non-interest d. Image after threshold is adjusted e. Area selected to be subtracted from total area as it was not corroded, but an effect of machining

The throwing power of each sample was measured using Image J. The scale was adjusted, and the depth of IGC as well as the distance from the edge of the AA5456-H116: CDA 706 interface were measured. The IGC at set distances of 0 to 8000 µm from the interface in increments of 500 µm was also measured. Figure 4.8 shows a visualization of the throwing power across a sample. Distance of throwing power was measured from the CDA 706 and AA5456-H116 interface, as depicted by the farthest right vertical red line, to the farthest point at which any point IGC isdetected. IGC depth was measured from the top of the sample down in the S direction, with an exception being taken at the interface. Due to assembly requirements creating a defect in the interface surface, IGC was only characterized based on original AA5456-H116 surface exposed. Depths in these corners were taken from the original datum, based on the triangular shape. Distances were taken from these IGC fissures to the interface as performed previously.

Edge pieces, from Figure 4.5c, after imaging had the maximum IGC measurement recorded to be used as a baseline measurement of IGC across the whole sample. The maximum IGC observed down the S direction was utilized as a baseline for IGC unaffected by CDA. These values were utilized to quantify IGC depth on AA5456-H116 DoS 54 mg/cm^2 samples that are unaffected by CDA 706 inserts. This allows for better understanding of the effects of CDA 706 without bias of general corrosion patterns of AA5456-H116.

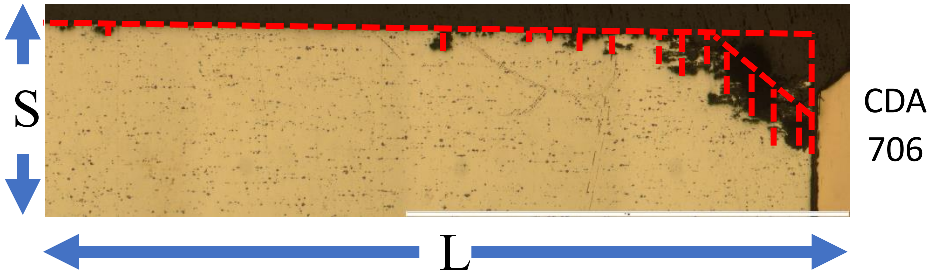

Figure 4.8: One of four fields of view, showing throwing power across AA5456-H116.

4.5.4 Ag Reduction

Each of the Ag samples had two trials using a Princeton Applied Research 263A potentiostat. An electrolyte of 0.1M Na_2SO_2, at pH=10, was de-aerated with N_2 for one hour. This solution was transferred to a flat cell while remaining under de-aeration, where it was de-aerated for an additional 10 minutes prior to reduction. Samples were galvanostatically reduced with a constant current of -0.1 mA. Following reduction, the 1st derivative of each scan was plotted against the original data, shown in Figure 4.9 for a 50 hr G85 WB sample. The 1st derivative shows the steepest point in reduction, which correlates to time of reduction, as described in detail by Neiser[14]. The charge of reduction was calculated using equation 1, where Q is the charge, I is the current (Amps), and t is time (s).

$$Q = It \qquad \text{Equation 1}$$

Charge was converted to thickness using equation 2 and 3 from ASTM B825[15].

$$T = \frac{itK}{a} \qquad \text{Equation 2}$$

$$K = \frac{10^5 M}{NFd} \qquad \text{Equation 3}$$

Where T=thickness (Å)

i=current (mA)

t=time (s)

a=area (cm^2)

K=conversion factor

M=gram-molecular weight of substance

N=number of faradays to reduce 1-gram substance (1 for AgCl, 2 for Ag_2S)

F=Faraday's constant (9.65x10^4 C)

d=density substance reduced (g/cm^3)

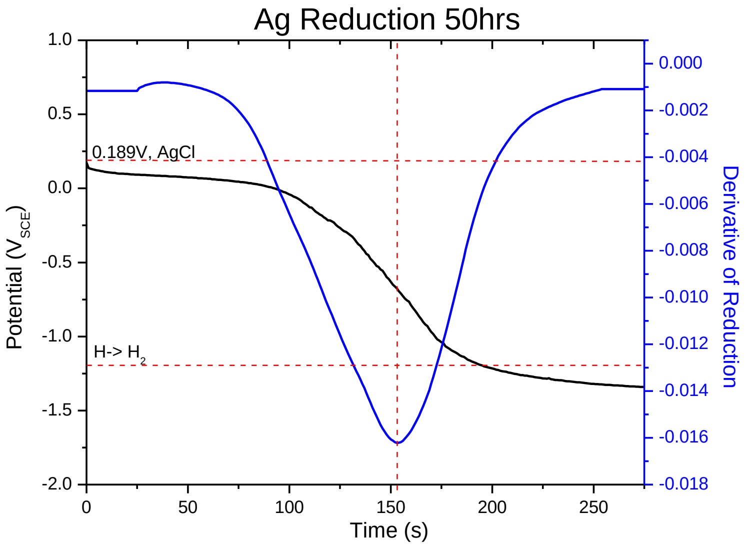

Figure 4.9: Ag Reduction curve for G85 WB 50hr sample, plotting Potential vs time, and the derivative of the potential vs time to show reduction time

4.5.5 Electrochemical Polarization Curve Measurements

A three-electrode flat cell setup was utilized to perform potentiodynamic polarization curve measurements for CDA 706 and AA5456-H116, respectively. CDA 706/AA5456-H116 test coupon with a surface finish of 1200 grit acted as working electrode (WE), and saturated calomel electrode (SCE) as well as Platinum-Niobium (Pt-Nb) mesh wire were used as reference and counter electrodes respectively. The solution compositions simulating different relative humidity environment during the G85 testing electrolytes were calculated by OLI Analyzer Software Ver. 9.5.3 (OLI Systems, Cedar Knolls, NJ) humidity's samples are exposed to while in the accelerated G85 tests. The composition of simulated electrolytes, along with their corresponding RH are listed in Table 4.3.

Table 4.3: Electrolyte composition for corresponding RH

RH (%)	95	90	80	70	60	50
NaCl (M)	0.9	2.7	5	5.4	2.9	1.1
pH	2.9	2.58	2.2	1.21	1.12	1.29
Solution conductivity κ (S/m)	11	23	35.7	17	3.6	1.5

All the measurements were conducted in quiescent solutions after 2-hour open circuit potential (OCP) by Bio-Logic VMP3 Potentiostat (Bio-Logic SAS, Claix, France), Cathodic scans for CDA 706 started at 0.05 V above OCP, and ended at -1.2 V_{SCE}, with a scan rate of 0.5 mV/s. Cyclic potentiodynamic measurement with scan rate=0.5 mV/s were used for AA5456-H116 and scanned from -0.05 V below OCP in the positive direction until reaching the current density limit equal to 0.1 A/cm^2, and then scanned in the negative direction until reaching a final potential of -1.2 $V_{SCE.}$ IR correction and curve extrapolation polarization curves of AA5456 at higher current density region were achieved by EC-Lab software Ver 11.01 (Bio-Logic SAS, Claix, France). These fitted polarization curves were used as boundary conditions in the modeling which will be discussed in the following.

4.5.6 Modeling Development

A two-dimensional finite element-based model with Laplace's Equation as the governing equation was developed to calculate potential and current distribution along the CDA 706/AA5456 galvanic couple, as a function of thickness of thin layer electrolyte on the galvanic couple surface in different environments corresponding to different RHs during the G85 tests. The modeling domain is the electrolyte only, which can be treated as the cross-section of thin film electrolyte above the center line of the galvanic couple along the length direction. Only half of the galvanic couple geometry was modeled so as to save computation time. A schematic plot of the modeling geometry is shown in Figure 4.10. R_{CDA} is the radius of CDA rod inserted in the AA5456 plate, L_{AA} is the length of AA5456 plate. The details of mathematical development have been described elsewhere[16,17]. For boundary conditions, the anodic kinetics of AA5456 worked as anodic boundary condition, whilst the cathodic kinetics of CDA 706 were used as the cathodic boundary conditions. In each simulated RH environment, potential and current density distributions were a function of electrolyte layer thickness (WL).

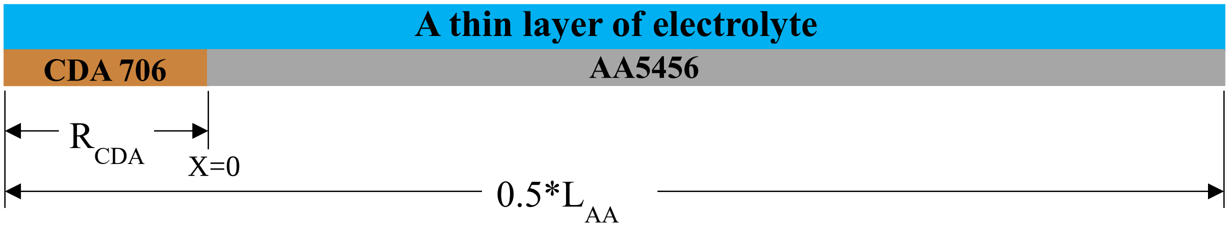

Figure 4.10: Schematic Plot of Modeling Geometry.

4.6 Results

4.6.1 Surface Analysis

As discussed earlier, surface damage on AA5456-H116 and cathodic protection of CDA 706 inserts were recorded following accelerated testing. G85 WB and G85 WB Modified samples with 3/8" CDA 706 inserts had nearly identical damage on AA5456-H116 as seen in Figure 4.11. The smaller 1/4" CDA 706 insert, although with much greater standard deviation, had less surface damage. The variance in surface damage implies that the larger cathode results in more AA5456-H116 surface damage. It can be noted that surface damage of the ¼" and 3/8" inserts are not proportional to the radius of damage on the AA5456-H116 interface suggesting that there is a defining area that limits cathode kinetics.

Figure 4.11 also points out the cathodic protection on CDA 706 inserts. The CDA 706 inserts are cathodically protected by coupling to AA5456-H116. There is more cathodic protection on G85 WB modified samples than the standard test. The ¼" CDA 706 insert also has less protection than the larger 3/8" CDA 706 insert.

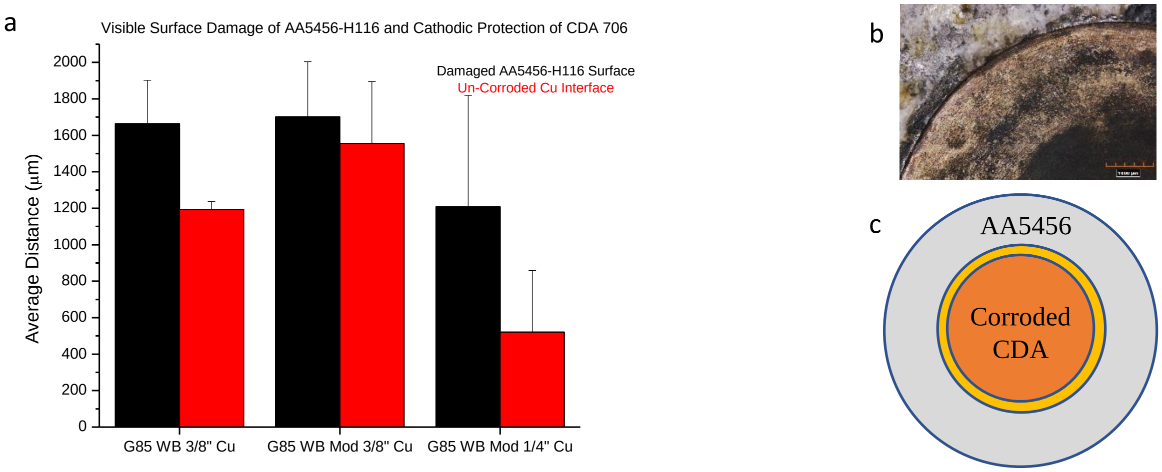

Figure 4.11: a. Surface damage on AA5456-H116 surface and cathodically protected CDA 706 b. AA5456-H116 3/8" CDA insert from G85 WB Modified test c. Diagram showing corroded CDA on uncorroded CDA when coupled to AA5456-H116

4.6.2 IGC Damage

Area of sub-surface corrosion damage, as shown in Figure 4.12, result in nearly identical damage to G85 WB and G85 WB modified samples in 31 and 14 days exposure respectively. The area corroded of the 3/8" CDA 706 inserts are nearly 3x larger than the ¼" CDA 706 insert. The surface area of CDA 706 exposed is 1.5x larger for the 3/8" insert than the ¼" CDA 706 insert. The surface damage almost doubled for an increase in CDA 706 diameter.

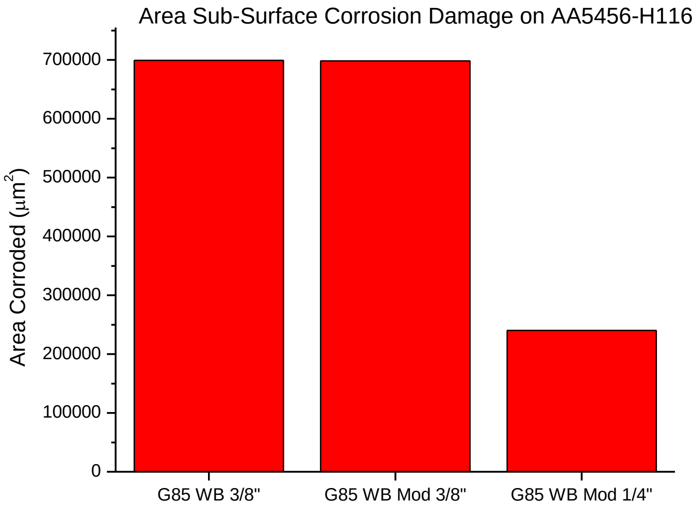

Figure 4.12: Area of corrosion subsurface damage on G85 WB 3/8" and G85 WB Modified 3/8" and 1/4"

Throwing power measurements for the G85 WB test, using a coupled AA5456-H116 DoS 54 mg/cm^2 sample with a 3/8" CDA 706 insert is shown in Figure 4.13. The majority of IGC falls above the baseline measurement as depicted by the red dashed line, and within the surface damage average and standard deviation measurements, from Figure 4.11, as depicted by the blue dashed lines. IGC depth decreases away from the CDA 706 interface, with the maximum IGC depth being 404 µm. There are a few IGC depth measurements above the baseline, measured from edge pieces, far from the CDA 706 between 6000-7000 µm from the coupling interface.

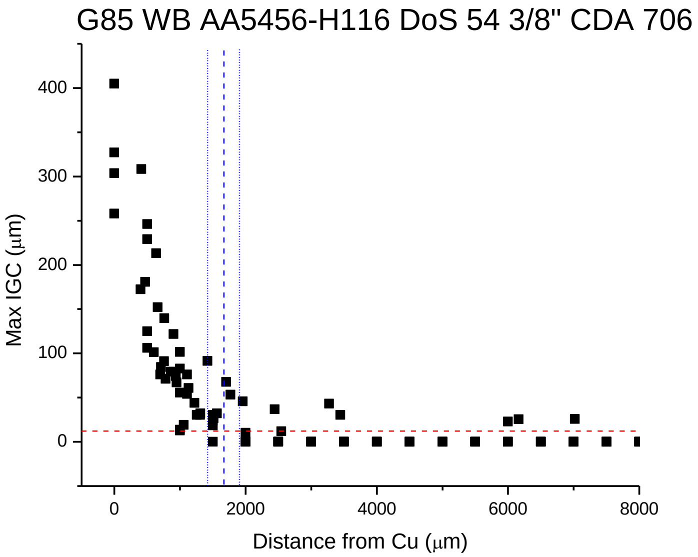

Figure 4.13: G85 WB 5456 throwing power plot of coupled DoS 54 mg/cm^2 with a 3/8" CDA 706 insert

G85 WB Modified test throwing power trends on AA5456-H116 DoS 54 mg/cm^2 with CDA 706 3/8" and ¼" inserts, shown in Figure 4.14 a&b respectively, have different trends than the standard G85 WB test. The red dashed baseline IGC depth is about the same for both samples, as it is the area investigated is unaffected by cathodic kinetics of CDA 706. Maximum IGC for both the 3/8" and ¼" CDA 706 insert are comparable around 250 µm. This depth of IGC is seen across about 2225 µm away from the coupling interface for the 3/8" CDA 706 insert shown in Figure 14a, within one standard deviation of the surface damage. From Figure 4.14b, the ¼" CDA 706 insert sample has the IGC depth fall off with distance from the coupling interface. There is, however, a cluster of visible IGC just beyond the visible surface damage average and one standard deviation measurements. IGC goes well past the visible surface damage, however are at small depths, and diminishing with distance from the coupling interface. At these distanced from the CDA 706 interface, IGC propagates further horizontally in the T direction than down in the S face.

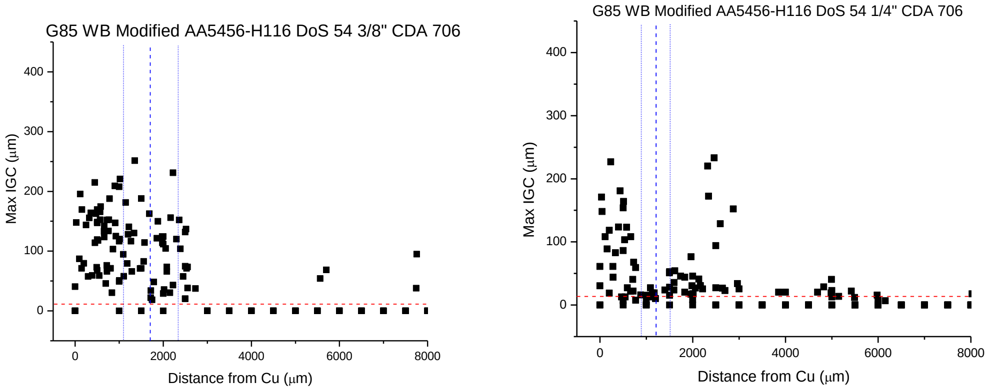

Figure 4.14: G85 WB Modified throwing power plot of DoS 54 mg/cm^2 with a a. 3/8" CDA 706 insert b. 1/4" insert

4.6.3 Ag Reduction

Ag reduction results standard G85 WB, are shown in Figure 4.15 a&b. Figure 4.15a shows the charge, Q (mC/cm^2) vs time (hrs) exposed. Figure 4.14b shows the thickness of Ag corrosion product (µm) vs time (hrs) exposed in G85 WB. As time increases, more AgCl deposits, but the variance increases over exposure time. Ag$_2$S is not seen at low exposure times but seen at 600hr G85 WB exposures. Sulfides are not explicitly included in the G85 WB test, but compressed lab air is used in G85 testing. Sulfides in the compressed air slowly make their way into the system, regardless of filters, and readily deposit on the Ag surfaces.

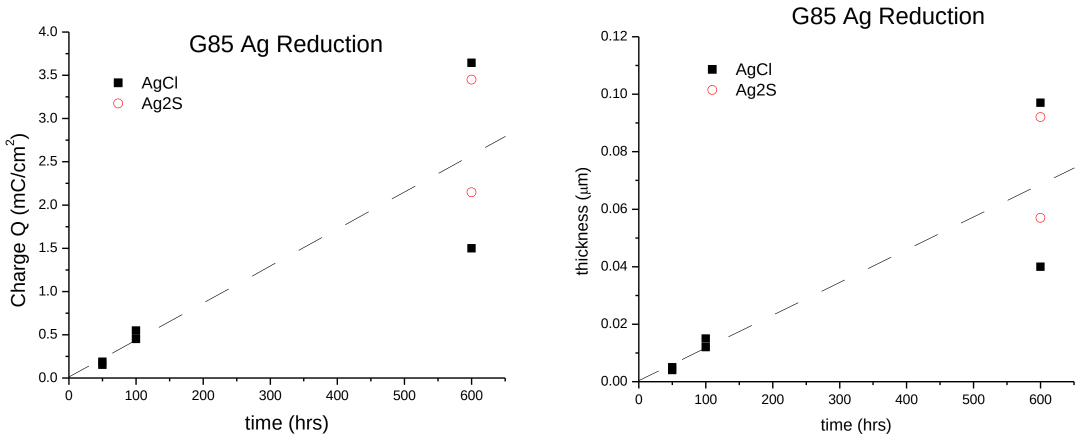

Figure 4.15: a. Ag reduction charge for varying lengths of exposure in G85 WB b. Ag corrosion film thickness for varying lengths of exposure in G85 WB

G85 WB Modified Ag samples had much greater variation in their results as shown in Figure 4.16 displaying the charge vs time. As time increases from 50 to 200 hrs, AgCl and Ag_2S both increase in Q (mC/cm^2). However, with extended time up to 404 hrs exposure, corrosion products decrease in thickness on the surface. Images of exposed samples are shown in Figure 4.17. Here it can be seen that at 100 and 404 hrs, there is uniform deposition across the Ag sample. However, on the 150 and 200 hr samples, there is not uniform deposition of corrosion products. From these images, and the pattern of the water marks, it seems that the G85 solution beads up and had deposited thicker AgCl and Ag_2S on select areas of the sample.

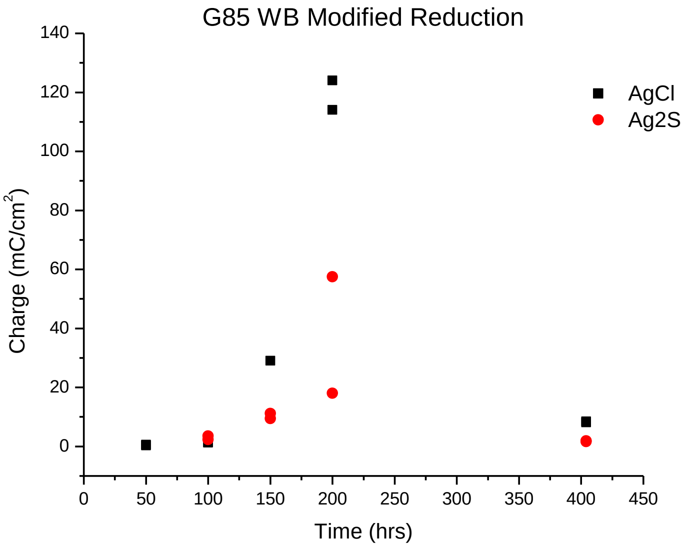

Figure 4.16: Ag reduction charge for varying lengths of exposure in G85 WB Modified

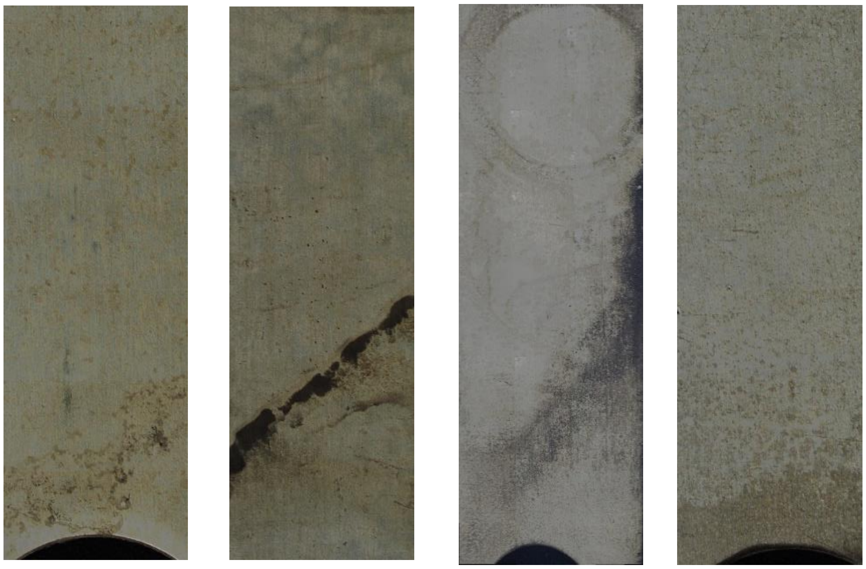

Figure 4.17: Ag samples following removal from G85 WB Modified

4.6.4 Electrochemical Tests

Polarization scans, for solutions representative of varying RH conditions are plotted in Figure 4.18. The potential versus the current density is plotted for both AA5456-H116 DoS 54 mg/cm^2 and CDA 706. AA5456-H116 sits at a higher potential than CDA 706. It is also evident that as the potential becomes more positive, not as a function of RH, but of molarity and pH from Table 4.3. At lower RH values, particularly evident in AA5456-H116 scans, the cathodic reduction shifts to higher current density values.

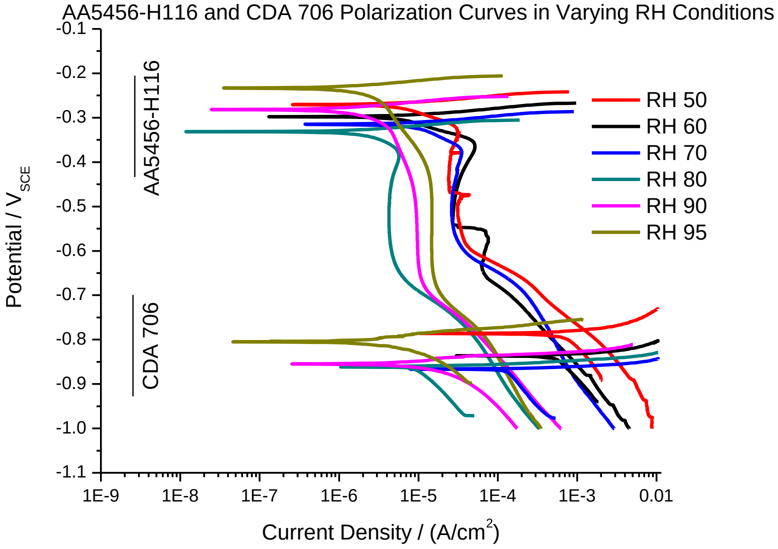

Figure 4.18: Polarization curves of AA5456-H116 DoS 54 mg/cm^2 and CDA 706 in solutions representative of various RH conditions

Copper ion activity, over varying RHs, seen below in Figure 4.19 shows potentials ranging from -0.0843 V to -0.29956 V. These calculated reversible potentials sit at or above the OCPs of CDA 706 from Figure 4.18. Because there is corrosion of the CDA 706, there must be enough ohmic drop or solution beading to bring the CDA 706 potential very near its OCP to get above this reversible potential and allow CDA 706 to corrode.

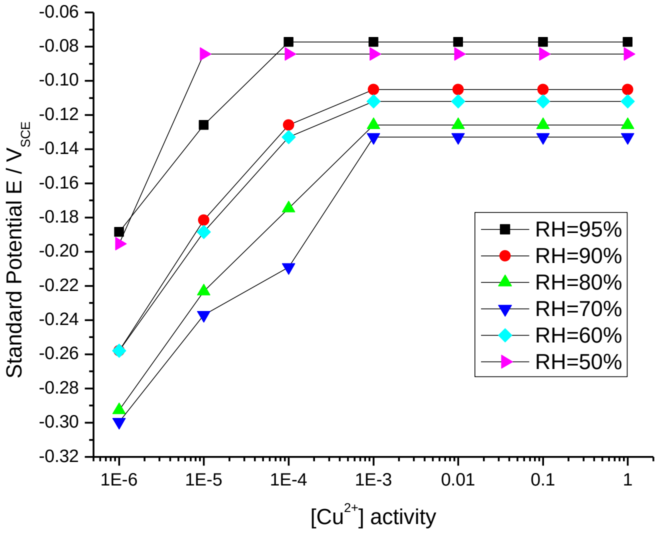

Figure 4.19: Standard potentials for varying Cu^{2+} *activity over a range of RH*

4.6.5 Modeling Results

This modeling work focused on the comparison of simulated results between G85 standard and modified tests the CDA insert = 3/8” only. Two aspects of the modeling work are the focus of this section: comparisons of simulated current distributions along the AA5456 plate as a function of RHs to demonstrate the effect of RH on the expected corrosion damage distributions; determination of the most relevant initial electrolyte layer thickness (WL) which results in the corrosion damage distribution furthest close to the maximum IGC distribution best rationalizing the observed maximum IGC distribution along the AA5456 plate shown in Section 4.6.2.

Direct measurement of electrolyte layer thickness during G85 tests has never been achieved due to the technical difficulty involved. However, a modeling approach provides an alternative to simulate the change in the WL and the pertinent current distribution under each WL, based on the estimation of initial WL at the very start of each G85 test (during the 45-minute spray period) and the subsequent RH time-course. To explicitly illustrate the relation between the initial WL and consequential change in WL, one should start with the equation:

$$WL = \frac{LD}{M \cdot C} \qquad \text{Equation 4}$$

where *LD* is salt loading density, *C* is equilibrium concentration of the thin film electrolyte (which is a function of humidity for a given salt at a given temperature), and M is the molar mass of sodium chloride (NaCl). For a preliminary estimation of change in WL during the G85 test in the modeling framework, it is assumed that *LD* was a constant during the entire test, and the equilibrium concentration of the electrolyte was fixed by RH. Because the G85 test started with RH=95%, it means that initial WL was associated with this RH value. By this definition, one can obtain relationship between WL and RH for different initial WL values taking into account the concentration values from Table 4.3, which is tabulated in Table 4.4.

Table 4.4: Water Layer thicknesses at various relative humidity values

RH (%)	WL (µm)						
95 (initial)	5000	4000	3000	2000	1000	500	100
90	1666.5	1332	1000	666	333.3	166.7	33.33
80	900	720	540	360	180	90	18
70	833.5	666.7	500	333.3	166.7	83.33	16.67
60	833.5	666.7	500	333.3	166.7	83.33	16.67
50	833.5	666.7	500	333.3	166.7	83.33	16.67

It should be noted that WL thickness is assumed to be constant when RH$\leq$ 70% for each scenario. The rationale is that the composition of the real solution was actually a mixture of water, acetic acid and NaCl. The test solution became saturated and began to precipitate NaCl solid salt when RH reached 70%, and NaCl has much smaller solubility in acetic acid than in water, resulting in far less concentrations of NaCl in the solution (RH=50, 60%) than saturated

NaCl concentration (RH=70%) based on OLI software calculation shown in Table 4.3. If the lowering of the deliquescence RH (DRH) by the acetic acid was not taken into account, the WL would have gone to zero at 75% RH as that is the DRH of pure NaCl. The surface stays wet at lower RH than 75% as shown in the RH data in Figure 4.2 and the TOW data in Figures 4.3 collected during the G85 cycles.

An example of comparisons of current density distributions along the distance away from CDA/AA5456 interface as a function of RHs for an initial WL=5,000 µm is shown in Figure 4.20. The current density distribution for RH≥80% are fairly uniform as compared to those at lower RH due to the lower galvanic coupling current and ohmic resistance brought by higher solution conductivity. For RH≤70%, the current density is at a maximum at the CDA/AA5456 interface before decreasing rapidly within a short distance away (< 2 mm) from the interface, before reaching a plateau near zero. The lower RH, the more dramatically is the decrease in current density, and the low-current density plateau was closer to the CDA/AA interface. For example, RH=50% reached the plateau at the distance~1,500 µm whilst RH=70% was about 3,000 µm.

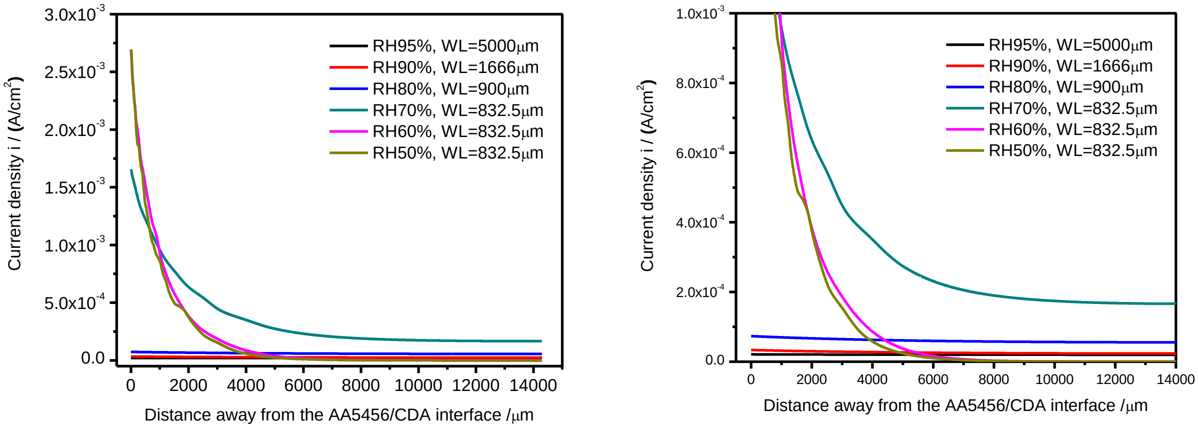

Figure 4.20: a) comparisons of current density distributions along the distance away from CDA/AA5456 interface as a function of RHs for an initial WL=5,000 μm; b) Zoom-in view of distributions for RH≥80%

The next modeling aspect is to determine the most relevant initial WL from which the resultant simulated charge distribution along the AA5456 plate was most close to the maximum IGC depth distribution observed. The following method was utilized to take into account the variation in RH during each G85 standard/modified test cycle: the percentage of time period for each RH (50, 60, 70, 80, 90, and 95%) during every 24hr-cycle based on Figure 4.2 was defined in Table 4.5. The WL for each RH was calculated for range of initial WL and FEM modeling was used to calculate the current distribution for each case. The total charge density during the entire test was calculated for the cases with different WLs for each position along the first 8000 μm away from the CDA/ AA5456 interface (Figure 4.13 and 4.14 a)), based on the equation:

Total current density (initial WL) = $\sum_{RH} i_{RH} \cdot (percentage\ during\ 24hr\ cycle) * 24 * 3600 * days$

where subscript *RH* is 50, 60, 70, 80, 90 and 95% respectively, i_{RH} is the value from the first modeling study, and the number of days is 31 for the standard test, and 14 for the modified test.

Using this approach, the cumulative charge density distributions as a function of distance from the CDA/AA5456 interface as a function of initial WLs and can be compared with the maximum IGC depth observed as shown in Figure 4.21. It can be seen that the curves of initial WL=3,000 μm scenario best fit in the maximum IGC distribution patterns for both standard and modified tests, which implied that the initial WL for a G85 test was about 3,000 μm.

Table 4.5: Percentage of time period for each re-defined RH during every 24hr-cycle of G85 test

RH range	Simplified RH	Percentage (%) during 24hr-cycle (standard)	Percentage (%)during 24hr-cycle (modified)
RH≥95%	95	10.1	16
95%>RH≥85%	90	0.9	4.4
85%>RH≥75%	80	2.4	9.6
75%>RH≥65%	70	0.1	69.9
65%>RH≥55%	60	1.6	0.1
55%>RH	50	84.9	0

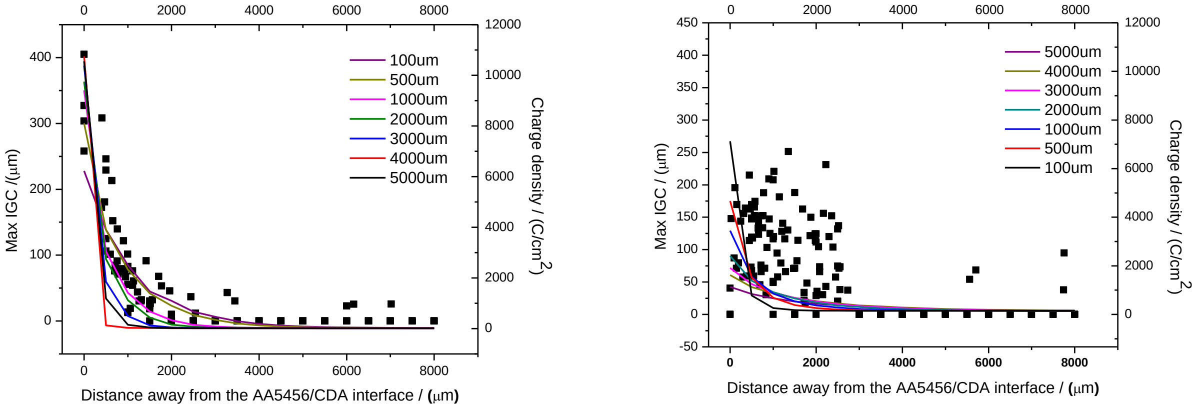

Figure 4.21: Comparison between modeling and experiment results. a) standard test; b) modified test.

4.7 Discussion

4.7.1 Damage Related to G85 Test Environment

AA5456-H116 damage, both surface and subsurface are related to the G85 testing protocols. In half the exposure time, modified G85 WB has very comparable area damage as standard G85 WB shown in Figure 4.12. Damage is more rapid in modified G85 WB due to the aggressive nature of the test. The modified test vs standard, shown in Figure 4.2 has only one minute of dry air. This maintains the humidity at about 70% RH or above, resulting in the samples staying wet for much longer than the standard test in which the humidity rapidly falls to very low values and never exceeds 50% after the end of the spray in each cycle. The modified test also remains wet for a longer duration of testing than the standard test, as shown in Figure 4.3. With the high humidity, salt clusters deposited on the AA5456-H116 surface shown in Figure 4.6.

The standard G85 has greater maximum IGC, but a stronger decay trend than the modified test, shown in Figures 4.13 & 4.14 respectively. The modified test has more fissures, and smaller attack depth. The modified test samples stay wet longer, resulting in more of the sample being under a thin layer of solution. There is more initiation of IGC due to decreased ohmic drop with increased wetness. This results in more anodic β-phase fissures being able to access the cathode, increasing the fissure count.

Surface damage of AA5456-H116 from the CDA 706 interface is comparable for both G85 standard and modified are comparable as seen in Figure 4.12. The throwing power of CDA 706 increases in the modified G85 relative to that of the standard G85 due to the increased wetness. The ¼” CDA 706 insert, compared to the 3/8” CDA 706 insert in the modified G85 test has less throwing power due to less cathode being available.

4.7.2 CDA Corrosion

CDA 706, although the cathode in this galvanic couple, corrodes as shown in Figure 3b due to the environmental characteristics of this study. With wetting and drying, G85 solution beads up on both the AA5456-H116 and CDA 706 surfaces as depicted in Figure 4.22. The modified G85 samples stay wet and in the drying/wetting stage for the majority of the test, while the G85 standard test is dry five out of the six hours each cycle, based on TOW data in Figure 4.3. Shown in Figure 4.11, when comparing the 3/8" insert, more CDA 706 corrodes on the G85 WB modified sample than the G85 WB standard test. However, from copper ion activity calculations in Figure 4.19, it is shown that CDA 706 should not corrode, meaning the cycle has an effect on CDA 706 corrosion. As the sample dries, the CDA 706 and AA5456-H116 decouple, and droplets corrode the CDA 706 as well as the AA5456-H116 as the sample decouples due to electrolyte diminishing.

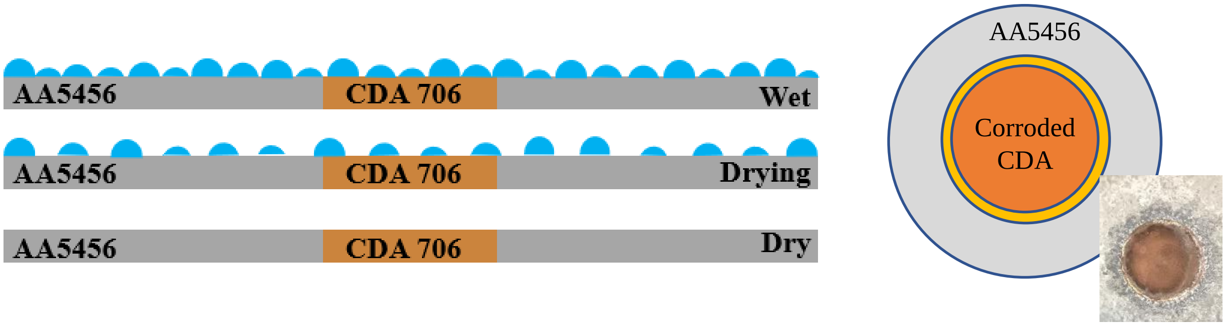

Figure 4.22: Wetting and de-wetting over CDA 706 interface in G85 WB and CDA 706 insert showing little uncorroded CDA 706

The CDA 706 inserts having undergone modified G85 WB exposures, have corroded CDA 706 area, shown in Figure 4.11. Under the modified conditions, the RH stays between 100 and 67%. At increased humidity's, the electrolyte layer thickens[18]. From TOW data in Figure 4.3, it can be seen that the modified G85 WB samples do dry, but not as rapidly as the standard test. In order for the CDA 706 to corrode, the water layer has to thin enough to allow for decoupling of CDA 706 and AA5456-H116. It can be seen from Figure 4.23 that corrosion products build up vertically on the G85 standard test, while salt deposits on the edge of the CDA 706 insert. This deposition protects a larger area of CDA 706 from corrosion by maintaining coupling with AA5456-H116. Although throwing power is comparable in both tests, shown in Figure 4.11, there is much deeper damage closer to this throwing power distance away from CDA 706, seen in Figure 4.14 for the modified test correlating to the increased cathodic kinetics.

Figure 4.23: Untouched and cleaned AA5456-H116 samples with a 3/8" CDA insert tested in a. G85 WB and b. G85 WB Modified

4.7.3 Ag Reductions Related to Accelerated Testing Environment

Ag reduction results show more corrosion product on the modified G85 WB removals than the G85 WB standard. The modified test is much more aggressive, with little dry time. With the high humidity's, seen in Figure 4.2, the solution will remain more corrosive as evident in Table 4.3 resulting in increased corrosivity of coupled samples, and Ag removals. For the modified G85 WB Ag samples, there is great fluctuation in deposition over time and no linear relationship as would be expected. Figure 4.17 shows inconsistent deposition for 150 and 200 hr exposure times. Because of very high NaCl deposition and little wetting and drying, there are inconsistencies in Ag reduction. This phenomenon has been seen by Frankel et al in the past[19].

Even though there are difficulties with Ag being used as a corrosion standard in modified G85 WB tests, it is a valuable tool for monitoring corrosivity of accelerated tests. G85 WB reduction results show that there is a linear trend seen in Figure 4.15. Accelerated tests in ASTM B117, including the addition of ozone, have validated the use of Ag for monitoring corrosivity in accelerated corrosion chambers[14]. For outdoor exposure Ag retrievals, studied in detail by Abbott[20], Ag corrosivity is shown to increase over time and is location dependent.

4.7.4 Experimental and Modeling Comparisons

From Figure 4.21a, it can be seen that for Standard G85 WB tests, a water layer 3000 µm best rationalizes the observed corrosion damage. This water layer thickness is found at 95% RH, which is representative of the solution chemistry of standard G85 solution, as evident in Table 4.4. From Table 4.5, it is evident that the testing cycle remains at this high humidity for 10.1% of the test. This is significantly less than the time spent at 55% RH. However, the time spent at this high 95% RH is long enough to increase the WL thickness, and accelerate IGC propagation. The model was able to predict maximum IGC depth and throwing power of approximately 2000 µm as found from surface and subsurface damage plotted in Figures 4.11 & 4.13 respectively. Damage from the Modified G85 test, plotted with charge densities from the model shown in Figure 4.20b, does not readily fit the model. The 3000 µm water layer reflects a representative throwing power to that seen, however IGC depth distribution is not reflected by charge density distribution. As the modified G85 exposed sample remained wet, IGC depth was maximized due to CDA 706 coupling with damage out to about 2000 µm.

4.8 Conclusions

AA5456-H116 at DoS 54 mg/cm^2 and CDA706 galvanic coupling corrosion behavior was investigated under accelerated corrosion testing and Finite Element Modeling. The influence of RH fluctuation and water layer thickness was investigated to model IGC and throwing power laboratory results.

(1) IGC throwing power is comparable for both Standard and Modified G85 WB tests when comparing AA5456-H116 DoS 54 mg/cm^2 with a 3/8" CDA insert. The RH and TOW fluctuations, however, effect the depth of IGC away from the CDA 706 interface.

(2) As the size of the cathode increases in diameter, from ¼" to 3/8" CDA, tested in modified G85 WB, maximum IGC remains the same however throwing power decreases due to a decrease in cathodic influence.

(3) Ag Reductions show a linear trend in corrosion over time in the standard G85 WB test, while the modified G85 test had varied reduction results. The short dry time showed that the modified test cycle deposits more corrosion products, however they do not dry and deposit evenly.

(4) CDA 706 inserts, although coupled to AA5456-H116, develop corrosion products. As solution dries, and droplets form on the CDA 706 insert, CDA 706 and AA5456-H116 decouples resulting in CDA 706 corrosion.

(5) A water layer thickness of 3000 µm results in the most comparable model for IGC propagation from standard G85 WB accelerated testing.

4.9 Limitations

With modeling, there were some assumptions and limitations in this work. The RH and WL thicknesses were adjusted to find the most representative model. In reality, the RH and WL fluctuate throughout the cycle. The surface chemistry, was therefore assumed based on G85 electrolyte variations with RH.

4.10 Acknowledgments

Financial support from the Office of the Undersecretary of Defense Technical Corrosion Collaboration via the USAFA Contract FA7000-14-2-0010 is gratefully acknowledged. Thanks to Mary Parker for assistance in G85 testing, and Victor Yang for aid in polarization testing.

4.11 References

1. Oguocha, I. N. A., Adigun, O. J. & Yannacopoulos, S. Effect of sensitization heat treatment on properties of Al-Mg alloy AA5083-H116. *J. Mater. Sci.* **43,** 4208–4214 (2008).
2. Lim, M. L. C. *et al.* Model to predict intergranular corrosion propagation in three dimensions in AA5083-H131. *Mater. Des.* **96,** 131–142 (2016).
3. Lim, M. L., Scully, J. R. & Kelly, R. G. Intergranular Corrosion Penetration in AA5083 as a Function of Electrochemical and Metallurgical Conditions service. **69,** 35–47 (2013).
4. Aylor, D. M., Hays, R. A. & Marshall, L. S. *Galvanic Corrosion Evaluation of High Performance Naval Seawater Valve Materials in Quiescent, Natural Seawater*. (2000).
5. Schleich, W. *Typical failures of CuNi 90/10 seawater tubing systems and how to avoid them*.
6. Mizuno, D. & Kelly, R. G. Galvanically Induced Intergranular Corrosion of AA5083-H131 Under Atmospheric Exposure Conditions - Part I –Experimental Characterization. 1–6 (2013).
7. Mizuno, D. & Kelly, R. G. Galvanically Induced Intergranular Corrosion of AA5083-H131 Under Atmospheric Conditions Part 2 Modelling the damage. *Corrosion* **69,** 681–692 (2013).
8. ASTM G85-02: Standard Practice for Modified Salt Spray (Fog). *Annu. B. ASTM Stand.* **82,** 8–9 (2006).
9. Parker, M. & Kelly, R. G. Developing a Framework for Improved Accelerated Testing of Aluminum-Lithium Alloys. (2017).
10. ASTM G67-04, ‘Standard Test Method for Determining the Susceptibility to Intergranular Corrosion of 5XXX Series Aluminum Alloys by Mass Loss After Exposure to Nitric Acid (NAMLT Test)’. (2004).
11. M. Tiryakioglu, J. T. S. Physical Metallurgy and the Effect of Alloying Additions in Aluminum Alloys. in *Handbook of Aluminum* (ed. G.E. Totten, D. S. M.) (Marcel Dekker, Inc, 2003).
12. Mary Parker (personal communication). (2018).
13. NIH. Image J.
14. Neiser, E. B. Atmospheric Corrosion of Silver and its Relation to Accelerated Corrosion Testing. (University of Virginia, 2010).

15. ASTM B825-13: Standard Test Method for Coulometric Reduction of Surface Films on Metallic Test. *Annu. B. ASTM Stand.* (2002). doi:10.1520/B0825-13.2
16. Liu, C., Rafla, V., Scully, J. R. & Kelly, R. G. *Mathematical Modeling of Potential and Current Distributions for Atmospheric Corrosion of Galvanic Coupling in Airframe Components*. *NACE Corrosion Conference* (2015).
17. Liu, C. & Kelly, R. G. The Use of Finite Element Methods (FEM) in the Modeling of Localized Corrosion. *Electrochem. Soc. Interface* **23,** 47–51 (2014).
18. Schindelholz, E. & Kelly, R. G. Wetting phenomena and time of wetness in atmospheric corrosion: A review. *Corros. Rev.* **30,** 135–170 (2012).
19. Lin, H., Frankel, G. S. & Abbott, W. H. Analysis of Ag Corrosion Products. *J. Electrochem. Soc.* **160,** C345–C355 (2013).
20. Abbott, W. H. A Decade of Corrosion Monitoring in the World ' s Military Operating Environments -A Summary of Results. *Columbus, OH DoD CorrDefense* (2008).

5 Summary, Technological Impact, & Recommendations for Future Work

5.1 Summary

5.1.1 Chapter 2: Galvanic Coupling Study of Sensitized AA5456-H116 with CDA 706 and the Effects of Cathode to Anode Coupling Area Ratios

The rate of intergranular corrosion (IGC) has been known to vary for DoS and cathode:anode ratio. This work shows that IGC off AA5456-H116 propagates minimally at low sensitizations (≤DoS 14mg/cm^2) and increases with DoS. With increasing anode size, from 1 cm^2 to 3 cm^2, IGC also increases. Cathodic current increases with cathode size, accelerating IGC. The steady state coupling potential tends to increase within increasing DoS, although at high sensitizations the coupling potential falls. Coupling current density is not affected by DoS or anode size, however increases with cathode area. IGC is observed to accelerate due to an assortment of variables.

5.1.2 Chapter 3: Outdoor Exposure of Galvanically Coupled Sensitized AA5456-H116 and CDA 706

Exposure retrievals show that there are a multitude of variables that effect IGC propagation. Geolocation and RH of these exposures have a major effect on IGC propagation. Increased TOW and salt spray due to ship service at sea accelerates IGC propagation. These observations were with IGC measurements as well as Ag reductions to monitor corrosivity of each environment. With longer exposures as well as increased DoS, IGC also accelerates. Increasing cathode insert diameter increased the throwing power and maximum IGC increases due to increasing cathodic current. Alloy variation, AA5083-H116 and AA5456-H116 showed no consistent trend in IGC propagation regardless of variation in Mg content.

5.1.3 Chapter 4: A Combined Experiment and Modeling Approach to Study ASTM G85 WB Accelerated Corrosion Testing of Galvanically Coupled Sensitized AA5456-H116 and CDA 706 Cupronickel

Standard and Modified G85 accelerated corrosion tests have comparable throwing power for the AA5456-H116 and CDA 706 3/8" insert. The modified test, however, had a consistent IGC depth over the entire throwing power distance of approximately 2000 µm, whereas the standard test showed the expected decrease in IGC severity with increasing distance from the cathode. Under modified G85 conditions, the ¼" CDA insert has approximately the same maximum IGC, but less throwing power than the 3/8" CDA insert. From Finite Element Modeling, using COMSOL, a water layer thickness of 3000 µm resulted is the most comparable IGC propagation trends from the CDA 706 interface for both standard and modified G85 exposed samples.

5.1.4 Comparisons of Data (Exposure and G85)

IGC depths compared to distances from the coupling interface, from both field exposures and accelerated corrosion testing, are comparable. It should however be noted; the solution chemistries of G85 WB and exposed samples are different. These comparisons are investigated to see the benefit of using accelerated testing in correlation to outdoor exposure damage. AA5456-H116 DoS 54 mg/cm^2 coupled to a 3/8" CDA insert from Chapter 3 and Chapter 4 are compiled below in Figure 5.1. It is evident that 12-month outdoor tests have less throwing power than a 31-day G85 WB accelerated testing. Visual surface throwing power damage is relatively comparable; however, it could be said that the exponential decay trend for outdoor tests is about 500 µm compared to 2000 µm for accelerated testing. Maximum IGC for the R/V Kilo Moana sample is higher than that of the R/V Endeavor and G85 tested sample. The exponential decay trends are similar. The IGC trend from G85, along with modeled results can be utilized to compare to exposure retrievals and accelerate testing in the future.

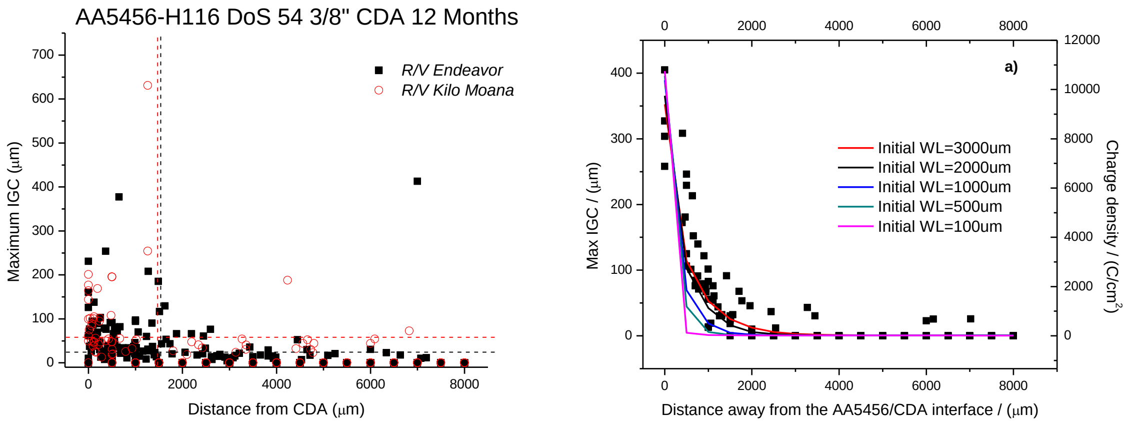

Figure 5.1: AA5456-H116 DoS 54 mg/cm^2 with a 3/8" CDA insert showing maximum IGC vs throwing distance from the coupling interface for a. outdoor exposures R/V Endeavor and R/V Kilo Moana 12-month exposure b. Standard G85 WB showing maximum IGC vs throwing distance super imposed with modeling results

5.2 Technological Impact

- *Cathode:Anode IGC Acceleration*

  Corrosion is a function of anode and cathode, however with increased cathode size and resultant cathodic kinetics, IGC propagates further on the anode. By investigating cathode size of CDA 706 when coupled to AA5XXX, with varying techniques, IGC can be better predicted for coupled samples. For applications where galvanic couples are unavoidable, it is of interest to know what cathode:anode ratios will have the most dramatic influence on IGC. Ship structures can be looked at in detail to see galvanic coupling ratios, and IGC formation rate can be predicted.

- *Effects of Variables of Exposed Samples on IGC*

  It has been found in this work, as well as by Khullar et al[1,2]. that the area of the anode has an effect on IGC rate. Accelerated testing protocols do not specify a requirement in sample size. Outdoor exposure testing does not have a standard protocol but is performed to show damage acceleration at different locations. This knowledge aids in developing matrices of future testing of AA5XXX alloys. It is important to utilize samples of an area large enough to propagate IGC, otherwise samples exposed will provide be non-representative of damage. A practical application of this is that accelerated testing protocols do not specify sample area for exposure. ASTM D1654[3] requires a scribe to represent coating defects. With no clear requirement for scribe area, as this work and Khullar[2] showed, if the area is too small, false negatives of IGC propagation may be reported.

- *Correlation between Outdoor Exposures and Accelerated Testing*

  To truly understand how IGC will propagate in the field, outdoor exposures are necessary. It, however, is not ideal to wait long durations to know when samples will corrode. By comparing exposure analysis to samples tested in accelerated corrosion chambers, correlations can be made to aid in prediction of corrosion rate with shorter testing times. Through modeling of G85 WB test samples, performed in collaboration with Chao (Gilbert) Liu, damage in accelerated testing environments can be predicted and correlated to outdoor exposure retrievals.

5.3 Recommendations for Future Work

The current research explores the role of galvanic coupling of AA5XXX and CDA 706 in full immersion, outdoor exposure, and accelerated corrosion testing environments. This work can be used as a framework of understanding to move advance research in the following areas:

- *What is the relation of anode size to IGC propagation?*

Recent work by Khullar et al[1,2]. found that area of anode of 5XXX alloys in accelerated testing conditions affects IGC propagation. This work validates that in full immersion testing, there is an increase in IGC when changing the anode size from 1 cm^2 to $3cm^2$. It would be expected that damage for a 1:1 and 3:3 cm^2 cathode:anode ratio would remain the same, however, with increasing cathodic current, damage increases with area size. It is of interest to see what area of anode in varying conditions is large enough to accept this cathodic current and propagate IGC. This could affect and influence future accelerated testing experimental methods.

- *How do additional exposure retrievals vary in IGC damage?*

  In this work, both 6 & 12-month exposure retrievals were analyzed and quantified for damage. With additional 18 and 24-month retrievals, it is of interest to see how IGC propagation accelerates based on geolocation, RH, AA5XXX alloy, and cathode:anode ratio. Silver returns from these vessels, used to quantify corrosivity of the environment, can be compared to past work on Ag reductions by Abbott[4] and related to damage. This will aid in predicting damage of AA5XXX and CDA 706 couples exposed in naval applications.

- *How does stress added to these systems affect IGC propagation?*

  Current work is beginning here at the University of Virgina by Dr. Kelly and Dr. Burns in collaboration with LUNA and the Office of Naval Research (ONR) to investigate stressed samples on a United States Navy ship, as well as accelerated testing. By investigating stress effects on AA5XXX alloys, there will be increasing understanding of the corrosion rates of these alloys in addition to the studied cathode:anode effects studied in this work.

- *Damage Quantification Improvements*

  All samples had IGC quantified by multiple cross-sectional images. This was performed to get multiple representations of the data and attempt to get a true representation. For exposure retrievals and accelerated testing samples, Image J was used to find area of damage on surface images and subsurface cross-sections. However, 3D characterization, using X-ray computed tomography (XCT) may better represent damage.

- *Data retrievals*

  Following data returns, it would be of interest to have consistent data over exposure. The research vessels utilized had variability in data collection. To mitigate this data loss and have consistent RH data throughout the exposures, data-loggers would provide more consistent and easier manipulated data. It would also be beneficial to log all incoming meteorological weather data and investigate additional weather effects including salinity and precipitation.

- *Data Science Application*

  For future work, it would be beneficial to create a data supply for future researchers of exposure results. This database would include meteorological data, IGC depth measurements, as well as surface damage. A database would be a useful resource for those investigating exposures, as well as working on correlating laboratory work to real-world results.

5.4 References

1. Khullar, P., Badilla, J. V & Kelly, R. G. Intergranular Corroson in Al-Mg 5XXX Alloys Under Atmospheric Exposures. in *NACE* 1–10
2. Khullar, P. Cathodic Control of Intergranular Corrosion in Sensitized AA5083 H-131. (University of Virginia, 2018).
3. ASTM D1654-08: Standard Test Method for Evaluation of Painted or Coated Specimens Subjected to Corrosive Environments. **8,** 8–11 (2017).

4. Abbott, W. H. A Decade of Corrosion Monitoring in the World ' s Military Operating Environments -A Summary of Results. *Columbus, OH DoD CorrDefense* (2008).